THESIS FOR THE DEGREE OF DOCTOR OF PHILOSOPHY

Probing Unconventional Superconductivity in Hybrid Josephson Junctions

NERMIN TRNJANIN

Department of Microtechnology and Nanoscience (MC2)

Quantum Device Physics Laboratory

CHALMERS UNIVERSITY OF TECHNOLOGY

Göteborg, Sweden 2026

Probing Unconventional Superconductivity in Hybrid Josephson Junctions
NERMIN TRNJANIN

ISBN 978-91-8103-442-4
Doktorsavhandlingar vid Chalmers tekniska högskola
Ny serie Nr 5899
ISSN 0346-718X

Quantum Device Physics Laboratory
Department of Microtechnology and Nanoscience (MC2)
Chalmers University of Technology
SE-412 96 Göteborg, Sweden
Telephone: +46 (0)31-772 1000
www.chalmers.se

Cover
False-colored SEM images of three nanodevices covered by an Ensō circle.

Printed by Chalmers Digital tryck
Göteborg, Sweden 2026

Probing Unconventional Superconductivity in Hybrid Josephson Junctions
NERMIN TRNJANIN
Quantum Device Physics Laboratory
Department of Microtechnology and Nanoscience (MC2)
Chalmers University of Technology

Abstract

Topological superconductivity represents a promising direction for fault-tolerant quantum computing through the braiding of Majorana bound states. Realising robust experimental platforms, however, remains challenging due to disorder, competing transport channels, and the need for precise symmetry engineering. Superconducting hybrid systems provide a versatile platform for combining superconductivity, spin-orbit coupling, magnetism, and mesoscopic phenomena in tuneable low-dimensional devices.

This thesis investigates superconductivity and transport in Josephson junctions based on ultra-thin Al-AlO_x-Al tunnel junctions, hybrid EuS-Al-InAs nanowires, and Bi_2Se_3 topological-insulator nanoribbons. The objective is to understand how superconducting correlations, symmetry breaking, and mesoscopic transport can be engineered and characterised in regimes relevant for topological superconductivity.

The first part of the thesis focuses on superconducting transport and spectroscopy in ultra-thin Al-AlO_x-Al Josephson junctions. By analysing the supercurrent peak within the framework of the Ivanchenko-Zil'berman and resistively and capacitively shunted junction models, intrinsic device parameters governing Josephson transport are extracted. Magnetotransport measurements reveal Fraunhofer-like interference patterns, enabling characterisation of the effective transport cross-sectional area. The results further demonstrate that ultra-thin aluminium junctions can operate as superconducting spectrometers at magnetic fields exceeding 1 T.

The second part investigates non-reciprocal superconducting transport in hybrid EuS-Al-InAs nanowire Josephson junctions. By varying the magnitude and orientation of external magnetic fields, a pronounced superconducting diode effect is observed. Importantly, a finite diode efficiency persists even in the absence of an externally applied magnetic field, demonstrating that engineered exchange fields alone can break the symmetries required for non-reciprocal superconductivity.

The final part explores quantum transport in Josephson junctions based on Bi_2Se_3 nanoribbons. By systematically varying junction geometry, distinct transport regimes are identified across different length scales. Short junctions are dominated by diffusive bulk transport, while intermediate junction lengths exhibit signatures consistent with superconducting transport with significant surface-state contributions. For longer junctions, the Josephson transport again becomes predominantly diffusive.

Collectively, these studies advance the understanding of superconducting transport and engineered hybrid superconducting systems relevant for topological superconductivity.

Keywords: Superconductivity; Josephson junctions; Hybrid superconducting systems; Topological superconductivity; Proximity effect; Mesoscopic transport; Josephson diode effect; Topological insulators ...

I dedicate this thesis to my beloved grandparents

You were the bravest and kindest people I have known

Acknowledgements

It seems like an eternity ago that I joined the Quantum Device Physics group at Chalmers as a PhD student in October 2019. During my time as a PhD student, I have had the privilege of being surrounded by wonderful individuals and being part of a great group.

I want to thank so many people for the support you have given me, starting with my family.

Draga mama, eto završio sam, i tako mi je drago što te mogu učiniti ponosnom. Kad pomislim da si stajala pored mene i tjerala me da radim domaću zadaću dok sam bio mali, a danas sam dogurao sve do doktorata. Hvala ti za sve što si učinila za mene.

Također želim zahvaliti ostatku svoje porodice ovdje u Švedskoj, svojim rođacima, dajdžama i ujnama. Kada neko kao ja jednostavno ne napušta univerzitet, drago mi je da niste mislili da sam lud i što ste imali pouzdanje u mene.

Mojoj dragoj sestri i dragom bratu u Švicarskoj, jako mi je drago što smo se našli čak i nakon toliko godina razdvojenosti.

Till alla som kände mig innan jag började min doktorandtjänst men också de som jag lärt känna efter, vare sig vi studerade tillsammans, tränat ihop eller om ni har blivit en ny del av min familj, vill jag tacka er för att ni finns i mitt liv. Tack till min kära Katerina som stöttade mig trots alla timmar jag lade ner på jobbet.

To all of you who came into my life during my time as a PhD student, you have become a core part of my life. My brothers in arms who spent so much time with me: Ivo, Vittorio, Ankit, Bekmurat, and Oleg, who were part of our special D1 group, not forgetting Theresa and Rodrigo, who joined us for their Master's theses. We shared a lot of fun as well as hardship together on the first floor of MC2.

Ivo, who I could always count on to have an answer to almost any question. Vittorio, who kept us all grounded. Last but not least, a great teammate in Ankit. I would not have wanted to go through these years with any other group of people. Thank you for everything, from the laughter to the science, to the running and the nights out.

Beyond our little group on D1, I want to thank the rest of QDP, in particular the former and current members of the Quantum Materials and Nano Devices group, who took me in as an orphan scientist. First and foremost, I owe immense gratitude to my supervisor Thilo Bauch, without whom I would not have come this far. Núria, who has been the work sister I did not know I needed. Kiryl, who swooped in and became my TI-guru. But also the other former and current

members of the group, Alessia, Edoardo, Ananthu, Floriana, Alexei, Karn, Klinti, Xavier and Riccardo and for all the scientific discussions and for welcoming me into the group. Outside QmanD, Dag W., Federico C., Sumedh M., and Samuel L.-A., I want to thank you for being guiding voices. Lars Jönsson, without whom the lab would probably have broken down entirely.

To a certain group of people outside QDP at MC2 who have been part of this journey: Ragnar D., Amr O., Chris W., Marina K., Paul N., Ariadna S., Therese K. and Alejandro V.-V. We shared countless coffees, beers, dinners, lunches, meetings, you name it! Thank you for making MC2 a place filled with people who broadened my horizons both professionally and personally.

I also want to thank Niclas Lindvall, Henrik Fredriksen, and Marcus Rommel at the nanofabrication lab, without whom none of the work presented in this thesis would have been possible.

I would also like to thank my collaborators from Copenhagen, Jesper Nygård. and Yu Liu, I want to express my gratitude for your dedication and for providing us with the materials we needed to conduct our research.

I am sure that I have forgotten some people, and for that I am sorry, but please know that I am grateful regardless of the size of your contribution to my life.

List of publications

This thesis presents an introduction, summary and extension to the following appended papers:

[I] N Trnjanin, I. Cools, V Buccheri, O Shvetsov, and T Bauch, "Magneto-transport properties of thin Josephson junctions for spectroscopic applications in the presence of large magnetic fields", Applied Physics Letters **127** (2025) 10.1063/5.0278518.

[II] N Trnjanin, I. Cools, V Buccheri, Y Liu, J Nygård, and T Bauch, "Magnetic-Field Anisotropy of the Josephson Diode Effect in Ferromagnetic Hybrid Nanowires", (2026).

[III] K. Niherysh, N. Trnjanin, A. P. Surendran, G. Kunakova, X. Palermo, D. Montemurro, J. Andzane, D. Erts, D. S. Golubev, S. Lara-Avila, et al., "Ballistic transport in Al-Bi_2Se_3-Al nanoribbon Josephson junctions: indication from Fabry–Pérot interference and length dependent I_cR_n product", (2026).

We always refer to these publications as paper I, II and III according to the labeling in the list above.

Specification of my contributions to the appended papers

I. I was the main contributor to this work. I designed and fabricated the devices used in the study and carried out all transport measurements. I developed the software used for both the measurements and the data analysis, performed the formal analysis and validation of the results, and produced all figures presented in the manuscript. I also wrote the original draft of the paper and participated in the review and editing process together with the co-authors.

II. I was the main contributor to this work. I designed and fabricated the devices, performed the measurements, and developed the software used for data acquisition and analysis. I carried out the data analysis and validation of the results and prepared the figures included in the manuscript. I also wrote the original draft of the paper and contributed to the review and editing process together with the co-authors.

III. I contributed to the experimental investigation and carried out the transport measurements together with the other main co-author. I contributed to the analysis and interpretation of the transport data and prepared the figures related to this part of the work. I also contributed to the writing, review, and editing of the manuscript.

Glossary

List of Abbreviations and Symbols

Abbreviations

AAS	Altshuler-Aronov-Spivak
AB	Aharonov-Bohm
ABS	Andreev Bound State
AC	Alternating Current
AFM	Atomic Force Microscopy
Al	Aluminium
AlN	Aluminium Nitride
BCS	Bardeen-Cooper-Schrieffer
BdG	Bogoliubov-de Gennes
BIA	Bulk Inversion Asymmetry
Bi_2Se_3	Bismuth Selenide
BTK	Blonder-Tinkham-Klapwijk
CPS	Coplanar Stripline
CPR	Current-Phase Relation
cQED	Circuit QED
DC	Direct Current
DOS	Density of States
DUT	Device Under Test
EBL	E-Beam Lithography
EDA	Extrinsic Device Asymmetry
EuS	Europium Sulphide
FFT	Fast Fourier Transform
FP	Fabry-Pérot
HfO_2	Hafnium Oxide
ICP	Inductively Coupled Plasma
ICPT	Inelastic CP tunnelling
InAs	Indium Arsenide
IVC	Current-Voltage Characteristics
IVVI	IVVI Interface
I-Z	Ivanchenko-Zilberman
JJ	Josephson Junction
JDE	Josephson Diode Effect
LC	Inductor-Capacitor
MAR	Multiple Andreev Reflection
MBS	Majorana Bound State
MXC	Mixing Chamber
NbTi	Niobium-Titanium
NbTiN	Niobium Titanium Nitride
NR	Nanoribbon
NW	Nanowire
PCB	Printed Circuit Board
QP	Quasiparticle
RCSJ	Resistively and Capacitively Shunted Junction
RF	Radio Frequency
SEM	Scanning Electron Microscopy
SGS	Subharmonic Gap Structure
SIA	Structural Inversion Asymmetry
SIS	Superconductor--Insulator-Superconductor
SiO_2	Silicon Dioxide
SN	Superconductor-Normal
SNS	Superconductor-Normal-Superconductor
SOC	Spin-Orbit Coupling
TI	Topological Insulator
TRS	Time-Reversal Symmetry
TSS	Topological Surface States
UCF	Universal Conductance Fluctuations
UHV	Ultra-High Vacuum
ZBP	Zero-Bias Peak

Symbols

A_{eff}	Effective junction area
B	Magnetic field
B_{ext}	Externally applied Magnetic field
B_{exc}	Exchange field
E_J	Josephson energy
E_{Th}	Thouless energy
E_Z	Zeeman energy
f_c	Cut-off frequency
I	Current
I_c	Critical current
I_{ret}	Retrapping current
I_{sw}	Switching current
k_F	Fermi wavevector
L_N	Junction length
L_J	Josephson inductance
L_k	Kinetic inductance
ℓ_e	Elastic mean free path
ℓ_ϕ	Phase coherence length
ℓ_{SO}	Spin-orbit length
Q	Quality factor
R_N	Normal-state resistance
T	Temperature (or Transmission coefficient)
V	Voltage
V_b	Bias voltage
V_g	Gate voltage
Y	Admittance
β_c	McCumber parameter
Δ	Superconducting energy gap
ϵ_D	Dirac point energy
λ_L	London penetration depth
Λ	Pearl length
μ	Chemical potential
ξ	Superconducting coherence length
τ	Transmission probability
φ	Superconducting phase difference
Φ	Magnetic flux
Φ_0	Magnetic flux quantum ($h/2e$)

Contents

1 Introduction

Since the discovery of superconductivity in mercury by Kamerlingh Onnes in 1911, superconductivity has remained a cornerstone of condensed matter physics [1]. The development of the Bardeen-Cooper-Schrieffer (BCS) theory in 1957 provided a microscopic understanding of this phenomenon in terms of Cooper pairing and established a framework for conventional, phonon-mediated superconductors [2]. Within this paradigm, superconductivity is characterised by a superconducting energy gap, macroscopic phase coherence, dissipationless charge transport, and perfect diamagnetic behaviour through the Meissner effect [3]. These properties enable a wide range of technologies across science and industry, including high-field superconducting magnets for Magnetic Resonance Imaging, Nuclear Magnetic Resonance spectroscopy, and particle accelerators such as the Large Hadron Collider, where fields up to 8.33 T are used to steer high-energy beams [4, 5]. Beyond high-field applications, superconductivity enables energy-efficient power transmission via high-temperature superconducting (HTS) cables [6], high-sensitivity detection using Superconducting Nanowire Single-Photon Detectors and Transition Edge Sensors [7], and devices exploiting macroscopic phase coherence such as superconducting quantum interference devices (SQUIDs) for biomagnetism [8] and superconducting qubits, a leading platform for scalable quantum computation [9, 10].

While BCS theory successfully describes conventional superconductors as spin-degenerate, time-reversal symmetric systems with s-wave spin-singlet pairing, characterised by phonon-mediated Cooper pairing, a fully gapped quasiparticle spectrum, and long-range phase coherence [3], it also delineates the boundaries of this paradigm. In particular, the mean-field treatment underlying BCS theory does not capture strong collective fluctuations of the superconducting order parameter.

These limitations become especially important in reduced dimensions, where thermal and quantum fluctuations are enhanced. More generally, the Hohenberg-Mermin-Wagner theorem demonstrates that continuous symmetries cannot sustain true long-range order in sufficiently low-dimensional systems at finite temperature [11]. In low-dimensional superconductors, fluctuations of the superconducting phase can therefore suppress global phase coherence even when local Cooper pairing remains intact [12–17].

Nevertheless, superconductivity can persist beyond the conventional BCS framework. When combined with strong spin-orbit coupling, magnetism, or nontrivial band topology, superconducting states can emerge with qualitatively different properties [18–22]. These developments have motivated the exploration of unconventional superconductivity.

A particularly important conceptual advance was the recognition that superconductors can be classified not only by their pairing symmetry, but also by topological invariants that depend on the presence or absence of fundamental symmetries such as time-reversal and particle-hole symmetry [23]. Topological superconductors can host topologically pro-

tected boundary states in the form of Majorana zero modes, quasiparticles that are their own antiparticles and obey non-Abelian exchange statistics [24]. The possibility of braiding Majorana modes to implement fault-tolerant quantum gates has positioned topological superconductivity as a candidate for scalable quantum computing architectures [24]. However, while several materials have been proposed as candidates for intrinsic topological superconductivity, unambiguous experimental verification remains challenging [25]. Consequently, much contemporary research has focused on engineered topological superconductivity in hybrid systems combining superconductivity, spin-orbit coupling, and magnetism [19].

Hybrid superconductor-semiconductor and superconductor-topological insulator structures provide a possible route towards realising topological superconducting phases [20]. In these systems, conventional BCS superconductivity is induced via the proximity effect from an adjacent superconductor, typically aluminium [26].

In contrast to conventional BCS superconductivity, the realisation of topological superconducting phases requires breaking time-reversal symmetry and lifting spin degeneracy to engineer effectively spinless superconducting channels with p-wave character [18, 27]. In low-dimensional systems, strong spin-orbit coupling combined with Zeeman splitting provides a practical route to this regime, as demonstrated in III-V semiconductor nanowires [27, 28]. Reduced dimensionality further simplifies the subband structure and mitigates orbital depairing, allowing phase-coherent superconductivity to persist even at the elevated magnetic fields (on the order of 1 T) required to open a topological gap.

The specific mechanism depends on the material platform. In semiconductor nanowires such as InAs, the interplay of Rashba spin-orbit coupling and Zeeman splitting can drive the system into an effectively spinless regime. In contrast, topological insulator nanoribbons based on materials such as Bi_2Se_3 host spin-momentum locked surface states that can acquire superconducting correlations via the proximity effect. In these systems, the application of approximately half a magnetic flux quantum through the nanoribbon can compensate the topological Berry phase and produce an odd number of one-dimensional modes, providing an alternative route to topological superconductivity.

A central challenge in hybrid Majorana platforms is the requirement of large Zeeman splitting to achieve a topological phase transition[20]. This splitting can be realised using external magnetic fields (B_{ext}) or proximity-induced exchange fields (B_{exc}) [20]. While B_{ext} introduces orbital effects that are intrinsically detrimental to superconductivity [19], h_{exc} provides a local spin-splitting mechanism that minimises orbital depairing [29]. Understanding how superconductivity can remain robust, coherent, and spectroscopically accessible under such conditions is therefore essential for progress towards topological quantum devices.

To address these challenges, this work employs two complementary material platforms: InAs nanowires with epitaxial Al and ferromagnetic EuS to enable strong spin-orbit coupling and intrinsic time-reversal symmetry breaking, and Bi_2Se_3 nanoribbons with evaporated Al contacts to induce superconductivity in the topological surface states.

Across these platforms, Josephson junctions play a central role by enabling phase-

coherent transport and providing spectroscopic access to low-energy excitations through their phase-dependent transport response. This allows the investigation of Andreev bound states, the details of which will be discussed later in this thesis, as well as potential Majorana modes [20, 30–32].

At the same time, hybrid systems introduce a variety of transport regimes, ranging from ballistic to diffusive [33], and symmetry-breaking phenomena such as non-reciprocal superconductivity, which are directly relevant to the systems studied in this work and have no analogue in conventional BCS systems [34, 35]. In particular, the preservation of phase-coherent ballistic transport is crucial for maintaining well-defined Andreev spectra and avoiding disorder-induced trivial states that can mimic topological signatures, as disorder can produce soft gaps and spurious zero-energy states [20, 36–42].

This thesis investigates key elements required for realising and probing topological superconductivity through experimental studies of superconducting transport and spectroscopy in hybrid Josephson junctions. It focuses on three central aspects: the development of ultra-thin Al junctions as robust spectroscopic probes at magnetic fields exceeding 1 T, symmetry breaking via intrinsic exchange in EuS-Al-InAs nanowires, and ballistic transport in Bi_2Se_3 nanostructures. Accordingly, this thesis is structured around three complementary studies.

- First, we demonstrate that ultra-thin aluminium Josephson junctions remain robust and fully functional for spectroscopic measurements in strong in-plane magnetic fields exceeding 1 T. Despite operating far beyond the typical field scales associated with conventional Al superconductivity, the junctions preserve phase coherence and exhibit pronounced Fraunhofer interference. Moreover, inelastic Cooper-pair tunnelling measurements reveal well-defined on-chip electromagnetic modes, confirming that these devices retain their spectroscopic sensitivity at high fields. Because topological phase transitions generally require Zeeman energies that exceed the induced superconducting gap, the survival of these integrated spectrometers at fields > 1 T is precisely what makes probing such transitions experimentally viable. (Paper I)
- Second, we explore non-reciprocal superconducting transport in hybrid EuS-Al-InAs nanowire Josephson junctions. These devices combine proximity-induced superconductivity with strong spin-orbit coupling and an exchange field generated by a ferromagnetic insulator. By systematically varying both the magnitude and orientation of an external magnetic field, we demonstrate a pronounced superconducting diode effect and investigate its anisotropic dependence on magnetic field orientation. Importantly, a finite diode efficiency persists even in the absence of an external magnetic field, demonstrating that engineered exchange fields can contribute significantly to the symmetry breaking required for non-reciprocal superconductivity. Crucially, because the Josephson diode effect requires the simultaneous breaking of time-reversal and inversion symmetries, these non-reciprocal signatures provide evidence for the symmetry-breaking conditions relevant to topological superconductivity. (Paper II)
- Finally, we investigate quantum transport in Josephson junctions based on Bi_2Se_3 nanoribbons, a material platform of central importance to topological superconductivity. Because bulk and surface transport coexist in Bi_2Se_3, disentangling their

respective contributions in both the normal and superconducting states remains a central challenge. By systematically varying the junction geometry, we identify distinct transport regimes across different length scales. In short junctions, transport is dominated by diffusive bulk contributions, while intermediate junction lengths up to approximately 500 nm exhibit signatures consistent with ballistic transport, including Fabry-Pérot-like interference. For longer junctions, the Josephson transport again becomes predominantly diffusive. These results establish the geometric regime in which coherent surface transport contributes significantly to the Josephson effect and highlight the role of superconducting probes in resolving phase-coherent transport channels in topological materials. (Paper III)

Taken together, the results presented in this thesis illustrate how conventional BCS superconductivity can be transformed, through material selection and device engineering, into a versatile platform for exploring unconventional and topological superconducting phenomena. By establishing robustness in high magnetic fields, revealing ballistic transport properties, and demonstrating controllable non-reciprocal effects, this work contributes to the experimental foundations required for realising topological superconductivity and, ultimately, topological quantum computing.

1.1 Thesis Outline

In this thesis, we investigate unconventional superconductivity in Josephson junctions. The remainder of the thesis is organised as follows:

- **Chapter 2** provides the theoretical background and is divided into two parts. The first part introduces the theoretical framework used to describe superconductivity in Josephson junctions, including superconducting interfaces, Andreev bound states, transport regimes, and interface transparency. It further discusses symmetry breaking, spin-orbit coupling, Zeeman effects, and the emergence of topological superconductivity, including asymmetric Andreev bound states and a brief introduction to Majorana bound states. The second part focuses on the theoretical description of experimental probes of Josephson junctions, including transport-based characterisation, critical current, environmental impedance, kinetic inductance, magnetic interference, Fabry-Pérot interferometry, the Josephson diode effect, and symmetry breaking in hybrid systems.
- **Chapter 3** describes the experimental methods, including an overview of device fabrication, measurement setups and filtering, instrumentation, measurement schemes, and cryogenic techniques.
- **Chapter 4** presents the experimental results. This includes the development of ultra-thin Al Josephson junctions as spectroscopic probes operating at high magnetic fields, the observation of the Josephson diode effect in InAs-Al-EuS nanowires, and the investigation of quasi-ballistic transport in Bi_2Se_3 nanoribbons.
- **Chapter 5** builds on the main findings and provides an outlook on future directions. This includes proposals for implementing a superconducting spectrometer based on ultra-thin junctions in a symmetric $\Phi_0/2$-biased DC SQUID configuration, dispersive readout of Andreev bound states in EuS-Al-InAs nanowires via coupling to a coplanar waveguide resonator, and further studies of Bi_2Se_3 nanoribbons aimed at accessing additional transport modes and improving electrostatic control through optimised gating architectures.
- **Appendices:** contain detailed fabrication recipes and supplementary derivations.
- **Appended papers:** The publications forming the basis of this thesis are included at the end of the document, following the references.

2 Background

This chapter introduces the physical framework underlying hybrid superconducting systems and their use as platforms for engineered topological superconductivity. The discussion is structured to connect material properties, microscopic transport mechanisms, and experimentally accessible observables.

We begin by outlining hybrid superconductor-semiconductor and superconductor-topological insulator platforms, emphasising the key ingredients required to realise topological phases, including proximity-induced pairing, spin-orbit coupling (SOC) which breaks inversion symmetry (IS), and broken time-reversal symmetry (TRS). This is followed by a microscopic description of transport in Josephson junctions (JJs), focusing on Andreev reflection, bound state formation, and the role of interface transparency and transport regimes.

Building on this foundation, we introduce the effects of symmetry breaking on the sub-gap excitation spectrum, including SOC, Zeeman splitting, and the emergence of asymmetric Andreev bound states (ABS) and ϕ_0-junction behaviour. The conditions for realising Majorana bound states (MBS) in low-dimensional systems are then discussed within this framework.

The final part of the chapter focuses on experimental probes of these phenomena, including transport spectroscopy, electromagnetic environment effects, magnetic interference, and phase-coherent transport signatures such as Fabry-Pérot (FP) interference and the Josephson diode effect (JDE). Together, these tools provide the basis for interpreting the experimental results presented in the subsequent chapters.

2.1 Hybrid Material Platforms for Topological Quantum Computing

Superconductivity is a macroscopic quantum state characterised by zero electrical resistance and the expulsion of magnetic fields through the Meissner effect. These properties arise from the formation of Cooper pairs, in which electrons bind into correlated pairs through an effective attractive interaction mediated by lattice vibrations [3]. A defining feature of the superconducting state is the emergence of a macroscopic quantum phase associated with the superconducting condensate.

When superconductors are incorporated into mesoscopic hybrid structures, coherent transport can also occur through adjacent normal regions via the superconducting proximity effect [43, 44]. In such systems, quantum interference phenomena depend on the ability of quasiparticles in the normal region to preserve phase coherence over finite distances. This coherence is ultimately limited by inelastic scattering processes that randomise the electronic phase. The associated phase coherence length therefore plays a

central role in determining the transport properties of mesoscopic superconducting devices and will be discussed in detail in Sec. 2.1.3.

The existence of a well-defined macroscopic phase makes superconductors a natural platform for quantum technologies. One example is the superconducting transmon qubit, where the nonlinear inductance of a Josephson junction is used to form an anharmonic LC oscillator with discrete quantum energy levels [9]. These systems have seen rapid experimental progress and currently represent one of the leading platforms for quantum computation [10]. However, their performance remains limited by decoherence arising from coupling to uncontrolled environmental degrees of freedom and materials-related imperfections, including charge noise, flux noise, dielectric loss, and parasitic two-level systems. Mitigating these effects requires substantial quantum error correction, posing a significant challenge for scalability.

These limitations have motivated the search for alternative approaches to quantum computation that are intrinsically more robust against local sources of noise. Topological quantum computing offers such a route by encoding quantum information nonlocally in the joint fermion parity of spatially separated Majorana bound states, making the encoded information inherently less sensitive to local perturbations [18, 24, 45].

In practice, however, this protection is not absolute. Several non-ideal mechanisms can degrade the topological protection. Finite spatial overlap between Majorana modes leads to an exponentially small energy splitting, lifting the ground-state degeneracy and introducing dephasing [46, 47]. In addition, non-adiabatic manipulation of system parameters can induce transitions out of the protected subspace, for example through Landau-Zener processes that populate excited states and mimic topological signatures [48, 49]. Furthermore, quasiparticle poisoning, arising from non-equilibrium excitations entering the system, can change the fermion parity and directly corrupt the encoded quantum information [50, 51].

Together, these mechanisms place important constraints on the realisation of robust topological qubits and highlight the need for careful control of device geometry, manipulation protocols, and the electromagnetic environment.

However, intrinsic topological superconductors are both rare and difficult to control experimentally. Candidate materials are limited and often exhibit unconventional pairing mechanisms whose symmetry remains under active debate [52, 53]. Moreover, their topological properties rely on specific band structures and material parameters that are not easily tuneable, making systematic experimental control challenging [25, 54]. In such systems, MBS are typically localised at defects or vortex cores, which makes their controlled manipulation and braiding experimentally challenging compared to engineered hybrid devices, where boundary modes can be more readily accessed and tuned.

As a result, much of the current effort has focused on engineering topological superconductivity in hybrid systems [20, 55]. In these platforms, superconductivity is induced in a non-superconducting material via the proximity effect [3, 56], while key ingredients such as SOC and broken TRS can be introduced and tuned in a controlled manner to create the conditions for a topological phase [27, 28]. A key advantage of these systems is the ability to independently control parameters such as carrier density (chemical potential μ), spin-orbit interaction strength, and magnetic interactions using electrostatic gates and material design, enabling systematic access to the relevant physical regimes [57, 58].

This level of control makes hybrid platforms a central focus in the search for engineered

topological superconductivity. The emulation of Majorana physics in these systems relies on the creation of a helical liquid [27] in which spin and momentum are locked due to strong SOC [59]. The application of a Zeeman or exchange field breaks TRS, lifting the remaining spin degeneracy and ensuring that only a single spin-polarised band crosses the Fermi level [29]. When this effectively spinless system is proximitised by an s-wave superconductor, the underlying helical structure forces the induced pairing to acquire an effective p-wave character [18]. In this regime, zero-energy MBS emerge at the system boundaries as self-conjugate quasiparticles, reflecting the intrinsic particle-hole symmetry of the superconducting state [60]. Their non-local encoding of fermion parity and the resulting ground-state degeneracy give rise to non-Abelian exchange statistics, offering a route toward fault-tolerant quantum operations [18, 24, 45]. Further details on MBS are discussed in Sec. 2.2.2.

The key ingredients required to engineer such phases include:

- **Superconducting pairing:** Induced via the proximity effect from a conventional superconductor, providing the necessary pairing potential [3, 56].
- **Spin-dependent interactions:** Arising from mechanisms such as Rashba SOC, which couple spin and momentum and modify the electronic band structure [59].
- **Broken time-reversal symmetry:** Introduced through external magnetic fields or magnetic proximity effects from ferromagnetic insulators like Europium Sulphide (EuS), enabling the formation of non-trivial topological phases [29, 61].
- **Phase coherence:** Maintained over mesoscopic length scales, allowing for coherent transport and the formation of bound states [30].

2.1.1 Engineering Topological Superconductivity in Hybrid Systems

The interplay of the above mentioned ingredients leads to the emergence of topological superconductivity under suitable conditions. In practice, different material systems provide distinct routes to achieving these requirements while also setting requirements on surrounding structures which might be used as spectroscopic tools to probe bound states in topological JJs.

Ultrathin Aluminium Josephson Junctions as Probing Tools for Low Energy Excitations

Aluminium (Al) based JJs form a well-established platform for superconducting quantum devices due to their reproducibility and compatibility with nanofabrication techniques [62]. In particular, ultrathin Al films exhibit enhanced critical magnetic fields compared to bulk superconductors, allowing superconductivity to persist in regimes relevant for hybrid devices [63, 64]. A representative device geometry and junction structure are shown in Fig. 2.1.

This is particularly important in the context of topological superconductivity, where magnetic fields of $\sim$ 0.5-2 T are often required to break TRS and access the topological regime [65, 66], depending on parameters such as the effective g-factor, chemical potential, and induced superconducting gap.

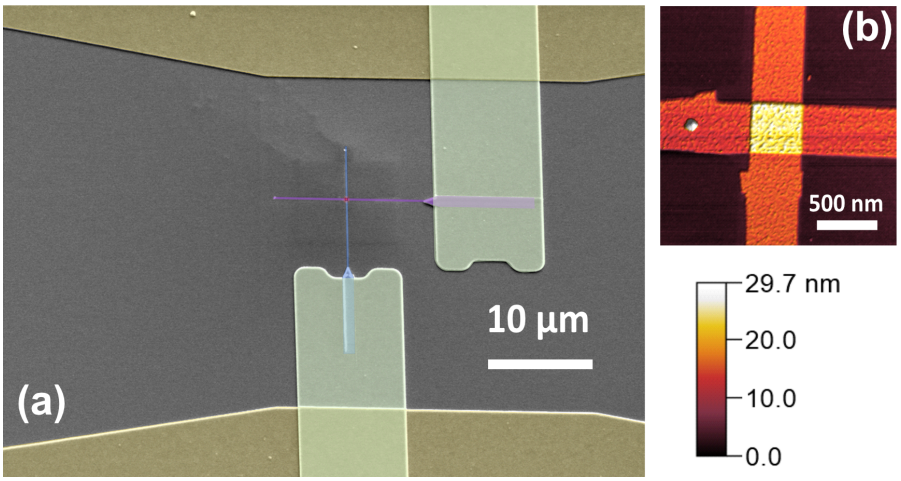

Figure 2.1: (a) False-colour scanning electron microscopy (SEM) micrograph of a representative ultrathin Al-based JJ device, highlighting the different material constituents and the junction region. (b) Atomic force microscopy (AFM) image of the junction area ($2\,\mu\text{m} \times 2\,\mu\text{m}$), showing the surface topography of the Al-AlO_x-Al junction and the overlap region forming the tunnel barrier.

Bulk conventional superconductors such as aluminium, lead, and tin exhibit relatively low critical fields on the order of $B_c \sim$ 10-100 mT, and therefore lose their superconducting properties well below the required field scales [63, 67].

In contrast, alternative superconducting materials such as niobium-based compounds can sustain fields on the order of tesla, but are often less compatible with standard nanofabrication techniques and the formation of high-quality hybrid interfaces [68].

This trade-off motivates the use of ultrathin superconducting films, in which the critical in-plane field can be significantly enhanced due to the suppression of orbital depairing in confined geometries [26]. In Al films, the critical field can increase from $\sim$ 100 mT for thicknesses of order 100 nm to values exceeding 1 T for films as thin as $\sim$ 10 nm [63].

In the tunnelling regime, an Al-AlO_x-Al junction can exchange energy with its electromagnetic environment during charge transport, enabling both absorption and emission of microwave excitations that are reflected in its current-voltage characteristics (IVCs). Details of this process are discussed in Sec. 2.3.1. As a result, ultrathin Al-AlO_x-Al junctions are particularly suitable for spectroscopic applications in the presence of such magnetic fields, where they can be used as sensitive probes of the electromagnetic environment and microwave excitations in nanoscale devices. In this work, such junctions are employed as on-chip spectrometers to investigate superconducting transport and LC modes under strong magnetic fields.

III-V Ferromagnetic Hybrid Nanowires

Semiconductor nanowires (NWs) based on III-V materials, such as Indium Arsenide (InAs), provide a highly tuneable platform for hybrid superconducting devices [69]. The low effective mass of quasiparticles in these materials leads to a reduced electronic density of states (DOS), making the chemical potential highly sensitive to electrostatic gating.

As a result, comparatively small gate-induced changes in carrier density can produce substantial shifts of the Fermi level [70, 71]. The reduced dimensionality and geometric confinement furthermore allow efficient electrostatic control of the carrier density. In addition, their strong intrinsic Rashba SOC, arising from the large atomic spin-orbit interaction of the constituent elements [72] and enhanced by structural inversion asymmetry (SIA) in narrow-gap III-V materials-and large effective g-factor give rise to pronounced spin-dependent effects [73]. When coupled to a superconductor, these NWs acquire superconducting correlations via the proximity effect, forming gate-tuneable JJs [74]. A representative NW and device geometry are shown in Fig. 2.2.

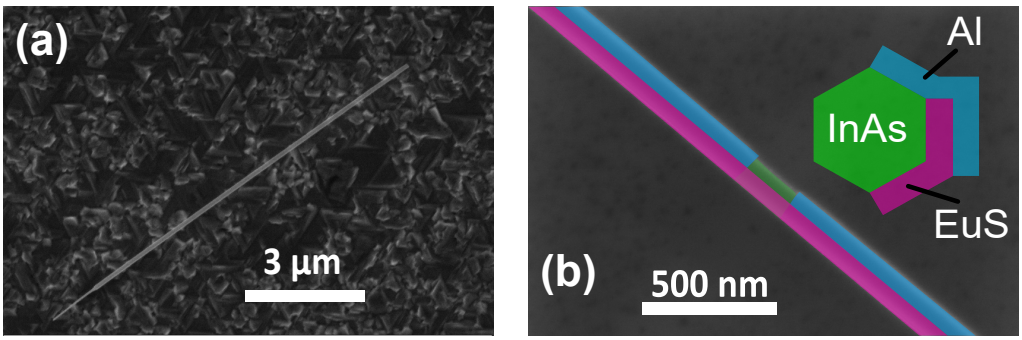

Figure 2.2: (a) SEM micrograph of an InAs NW on the growth substrate, consisting of an InAs core with epitaxial Al and EuS layers covering three of the six facets. (b) Device after transfer to a sample chip and selective etching of the Al shell to define a JJ. The remaining Al segments form superconducting leads, while the exposed NW segment acts as the weak link. False colouring highlights the different material regions, with Al shown in blue, EuS in pink, and the exposed InAs core in green. The Al and EuS layers overlap on a single facet of the NW.

Incorporating a ferromagnetic insulator, such as EuS, introduces an exchange field that breaks TRS without the need for large external magnetic fields [58]. This combination of superconductivity, tunability, and magnetic interactions makes hybrid NWs a versatile platform for exploring symmetry-breaking effects and engineered superconducting states [29, 75, 76].

Topological Insulator Nanoribbons

Topological insulators (TIs), such as Bismuth Selenide (Bi_2Se_3), provide an alternative route to realising topological superconductivity and associated exotic quasiparticles, including MBS [77]. These materials are characterised by an insulating bulk and conducting surface states that arise from strong SOC and band inversion [23, 78]. The surface states exhibit spin-momentum locking, forming a helical electron system that is robust against non-magnetic disorder [79, 80].

When brought into contact with a conventional superconductor, these surface states acquire superconducting correlations via the proximity effect [81], providing a distinct route to topological superconductivity compared to semiconductor NWs.

In this work, Bi_2Se_3 nanoribbons (NRs) are investigated, as shown in Fig. 2.3. The reduced thickness of these ribbons enhances the relative contribution of the topological

surface states (TSS) to transport by reducing the relative influence of bulk conduction.

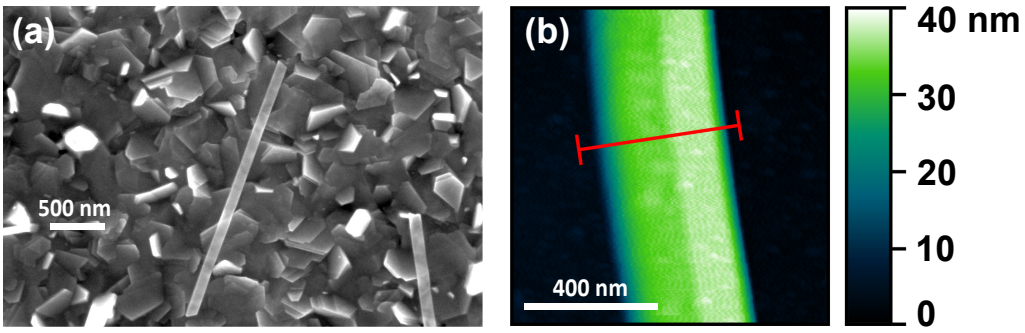

Figure 2.3: (a) SEM micrograph of a Bi_2Se_3 NR grown by physical vapour deposition (PVD) on the growth substrate. (b) AFM image of a transferred Bi_2Se_3 NR on a sample substrate. The ribbon thickness is extracted from a line profile taken along the red line.

NR geometries further provide lateral confinement, leading to transverse subband quantisation and enabling phase-coherent transport and interference effects across well-defined dimensions [82–84]. As a result, Bi_2Se_3 NRs offer a versatile platform for probing proximity-induced superconductivity and mesoscopic transport phenomena in low-dimensional topological systems [85, 86].

Moreover, in TI nanoribbons, an additional route towards topological superconductivity involves tuning the one-dimensional surface-state subbands using an axial magnetic flux. Because the spin momentum locked surface states acquire a geometric π Berry phase upon encircling the ribbon circumference, the transverse momentum quantisation develops a finite-size gap at zero magnetic flux [87, 88]. An axial magnetic flux introduces an additional Aharonov-Bohm phase that modifies the quantisation condition. At half a flux quantum ($\Phi = \Phi_0/2$), the Aharonov-Bohm phase compensates the Berry phase, causing one surface-state subband to become gapless. In this regime, the system effectively supports a single helical transport channel, providing a promising platform for topological superconductivity when proximitised by an s-wave superconductor [89, 90].

The π Berry phase originates from the spin-momentum locking of the topological surface states. As an electron encircles the nanoribbon circumference, its spin adiabatically rotates together with its momentum, causing the wavefunction to acquire an additional geometric phase of π. This phase modifies the transverse momentum quantisation condition and plays a central role in the magnetic-flux dependence of the surface-state subbands. A more detailed discussion of Berry phases and topological surface states can be found in Refs. [23, 78].

2.1.2 Andreev Reflection and Bound State Formation in Superconducting Hybrid Structures

While the properties of Cooper pairs in bulk superconductors are of fundamental interest, many key phenomena in mesoscopic devices arise at interfaces with other materials. At these interfaces, the interplay between superconducting correlations and adjacent normal,

semiconducting, or insulating regions gives rise to transport mechanisms absent in bulk systems.

We focus here on two prototypical cases: superconducting tunnel junctions (SIS) and hybrid structures involving normal or semiconducting regions (superconductor-normal (SN) and superconductor-normal-superconductor (SNS)), illustrated in Fig. 2.5, where panels (a-d) show the SIS, SN, and SNS cases discussed below.

To describe transport across such interfaces, it is useful to recall that the superconducting state requires both the formation of Cooper pairs and the establishment of global phase coherence. While the transition is phenomenologically bounded by a critical temperature T_c and a critical field B_c, these are essentially mean-field conditions for the existence of the pairing amplitude. In reduced dimensions or highly disordered systems, the actual transition to a zero-resistance state is further constrained by the superfluid stiffness (or phase stiffness [91]), ρ_s. This quantity measures the energy cost associated with spatial variations of the superconducting phase, ϕ. If the superfluid stiffness is low, thermal or quantum fluctuations can randomise the phase and destroy long-range order even while the pairing amplitude remains finite. Consequently, the resilience of the condensate is defined by the interplay between the pairing energy and the phase rigidity of the system.

Within this superconducting regime ($T < T_c$ and $B < B_c$), superconductivity can be described by a macroscopic complex order parameter

$$\Psi(\mathbf{r}) = \sqrt{n_s(\mathbf{r})}e^{i\phi(\mathbf{r})}, \tag{2.1}$$

where n_s is the Cooper-pair density and ϕ is the superconducting phase. Spatial variations of this phase give rise to supercurrents, establishing a direct connection between quantum coherence and charge transport.

A characteristic length scale associated with the superconducting condensate is the coherence length ξ_0, which describes the spatial extent of pairing correlations within the superconductor. In the clean limit, this is given by

$$\xi_0 = \frac{\hbar v_F^S}{\pi \Delta}, \tag{2.2}$$

where v_F^S is the Fermi velocity in the superconducting material and Δ is the superconducting gap. Physically, ξ_0 provides an estimate of the spatial extent of Cooper-pair correlations and defines the characteristic length scale over which the superconducting order parameter can vary spatially.

The presence of a well-defined superconducting phase becomes particularly important when two superconducting regions are coupled through an interface. In this case, the nature of charge transport depends sensitively on both the properties of the interface material and the length scale over which coupling occurs.

In the limit of a thin insulating barrier separating two superconductors (SIS junction, Fig. 2.5(a)), charge transport occurs via coherent tunnelling of Cooper pairs, giving rise to the Josephson effect [3],

$$I_s = I_c \sin\phi, \tag{2.3}$$

where $\phi = \phi_2 - \phi_1$ is the phase difference between the superconductors. The phase evolves in time according to the second Josephson relation,

$$\frac{d\phi}{dt} = \frac{2e}{\hbar}V, \tag{2.4}$$

establishing a direct link between quantum phase and electrical voltage.

An equivalent description is obtained in terms of a phase-dependent free energy of the junction. The supercurrent can be expressed as $I_s = \frac{2e}{\hbar}\frac{\partial F}{\partial \phi}$, which follows from considering the electrical work performed in changing the phase difference. Integrating Eq. (2.3), the free energy takes the form

$$F(\phi) = \text{const} - E_J \cos\phi, \tag{2.5}$$

where $E_J = \frac{\hbar I_c}{2e}$ is the Josephson energy, setting the characteristic energy scale of Josephson tunnelling across the junction.

While this macroscopic description successfully captures tunnelling between superconductors, hybrid structures involving normal metals or semiconductors require a microscopic description of quasiparticle transport across superconducting interfaces.

Superconducting Interfaces At superconducting interfaces, electron and hole excitations become coupled through the superconducting pairing potential, giving rise to proximity induced superconducting correlations in adjacent materials. The resulting correlations can persist within the normal region over a characteristic coherence length ξ_N [43]. Their magnitude and spatial extent depend sensitively on the transport properties of the weak link and the transparency of the superconducting interfaces.

More details concerning ξ_N for different transport regimes are discussed in Sec. 2.1.3.

When the interface connects a superconductor to a normal metal, the proximity effect enables superconducting correlations to penetrate into the normal region. Microscopically, this process is mediated by Andreev reflection, illustrated schematically in Fig. 2.5(b-c), in which electron and hole excitations are coupled through the transfer of Cooper pairs into or out of the superconducting condensate. For subgap energies, an incident electron is retro-reflected as a hole with opposite momentum and spin, causing the reflected trajectory to approximately retrace the original electron path. Conversely, Cooper pairs in the superconducting condensate can inject correlated electron-hole excitations into the normal region, establishing proximity-induced superconducting correlations. Charge transport is therefore governed by coupled electron-hole quasiparticle processes rather than direct Cooper-pair tunnelling.

The microscopic transport properties of such hybrid interfaces depend strongly on their transparency. In realistic devices, scattering at the interface can partially reflect incident quasiparticles, modifying both the superconducting proximity effect and the resulting transport processes. A convenient description of this behaviour is provided by the Blonder-Tinkham-Klapwijk (BTK) framework [92, 93], in which the interface is modelled by a delta-function barrier characterised by a dimensionless scattering strength Z.

Within this model, the transparency of an individual conduction channel is described by a transmission coefficient

$$\tau = \frac{1}{1+Z^2}, \tag{2.6}$$

where $\tau \to 1$ corresponds to a perfectly transparent interface and $\tau \ll 1$ describes the tunnelling regime dominated by normal reflection.

The interface transparency directly determines the normal-state conductance through the Landauer relation,

$$G_N = \frac{2e^2}{h}\sum_n \tau_n, \tag{2.7}$$

which in turn sets the normal resistance R_N. In the limit of high transparency ($Z \to 0$), Andreev reflection is enhanced and subgap transport is dominated by electron-hole conversion processes. In contrast, large barrier strengths ($Z \gg 1$) suppress transmission and drive the junction toward the tunnelling (SIS) regime.

A key experimental signature of interface transparency is the excess current (I_{exc}), extracted from the high-bias current-voltage characteristic ($eV > 2\Delta$) through

$$I(V) = \frac{V}{R_N} + I_{\text{exc}}. \tag{2.8}$$

Microscopically, I_{exc} arises from Andreev reflections at the interfaces. In the ballistic limit of a highly transparent interface, $I_{\text{exc}}R_N = \frac{4}{3}\Delta/e$ [94]. The evolution of this product as a function of the barrier strength Z is shown in Fig. 2.4(a).

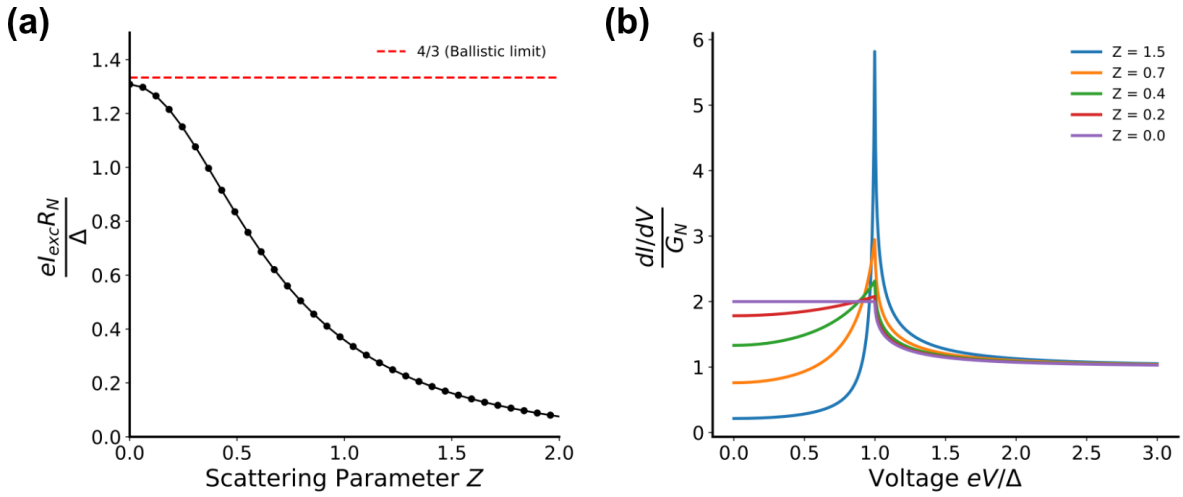

Figure 2.4: Transport signatures of interface transparency within the BTK framework for superconducting hybrid structures. **(a)** Normalised excess current $eI_{\text{exc}}R_N/\Delta$ for a SNS junction as a function of the dimensionless interface scattering parameter Z. The red dashed line indicates the theoretical maximum value of 4/3 for a perfectly transparent interface ($Z = 0$), adapted from [94]. The monotonic decrease in I_{exc} reflects the suppression of Multiple Andreev Reflection (MAR) processes as the interface transparency decreases. **(b)** Normalised differential conductance $(dI/dV)/G_N$ of a SN interface as a function of normalised bias voltage eV/Δ for representative values of Z. For a perfectly transparent interface ($Z = 0$), the conductance is doubled within the superconducting gap ($eV < \Delta$) due to ideal Andreev reflection. As Z increases, the subgap enhancement evolves into a tunnelling-like spectrum with suppressed zero-bias conductance and pronounced coherence peaks at the gap edges. The excess current shown in panel (a) corresponds to the integrated conductance above the normal-state baseline ($G/G_N = 1$) in panel (b).

At finite bias voltages below the superconducting gap ($eV < 2\Delta$), quasiparticles can undergo repeated Andreev reflections between superconducting interfaces. During each traversal across the junction, quasiparticles gain an energy eV, enabling transport through

a sequence of repeated electron-hole conversion events until sufficient energy is accumulated to access the quasiparticle continuum above the superconducting gap. This process, known as Multiple Andreev Reflection (MAR), produces characteristic subharmonic gap structures in the differential conductance at voltages

$$eV = \frac{2\Delta}{n}, \tag{2.9}$$

where n is an integer corresponding to the number of Andreev reflections involved in the transport cycle. Representative MAR spectra measured in Bi_2Se_3 and EuS-Al-InAs Josephson junctions are shown in Fig. 2.15(b-c).

Figure 2.4(b) additionally illustrates how the spectroscopic response evolves from the Andreev-enhanced regime ($Z = 0$) toward the tunnelling limit as the interface transparency decreases. The detailed morphology and periodicity of the resulting subharmonic gap structure (SGS) are highly sensitive to the microscopic nature of the weak link [95]. Material-specific properties, such as the Dirac or helical nature of the charge carriers, can modify the shape of subgap features, transforming them from resonant peaks to sawtooth-like shoulders depending on the channel transparency [96]. In systems where IS is broken due to SOC or spin-splitting is present, spin-polarised MAR processes can emerge, leading to split or asymmetric conductance features that reflect the interplay between magnetism and superconductivity [97, 98].

While MAR reflects non-equilibrium quasiparticle transport at finite bias, repeated Andreev processes can also give rise to discrete equilibrium bound states in superconducting weak links. In SNS junctions, coherent electron-hole conversion at the two superconducting interfaces leads to the formation of phase-dependent Andreev bound states, which provide the microscopic origin of Josephson transport.

Andreev Bound States in SNS Junctions In SNS junctions, repeated Andreev reflections at the two superconducting interfaces establish electron-hole correlations throughout the weak link, as illustrated in Fig. 2.5(d). Provided the junction length L_N remains shorter than the relevant coherence length in the normal region, these correlated quasiparticle trajectories maintain phase coherence across the junction [26, 44]. The interplay between the relevant coherence length and the junction length is discussed further in Sec. 2.1.3

The penetration of superconducting correlations can establish an induced superconducting gap Δ' within the normal region, defining the characteristic energy scale of proximity-induced quasiparticle excitations. It is important to distinguish this from the parent superconducting gap Δ of the superconducting electrodes; while Δ is an intrinsic property of the bulk superconducting material (e.g., Al), Δ' reflects the effective pairing strength experienced by charge carriers in the proximitised region. In realistic hybrid devices, the induced gap is typically reduced ($\Delta' < \Delta$) due to finite interface transparency, Fermi-level and density-of-states mismatch between the materials and disorder [93].

In this regime, repeated Andreev reflections at the two interfaces give rise to discrete ABS, which originate from phase-coherent interference of electron and hole trajectories

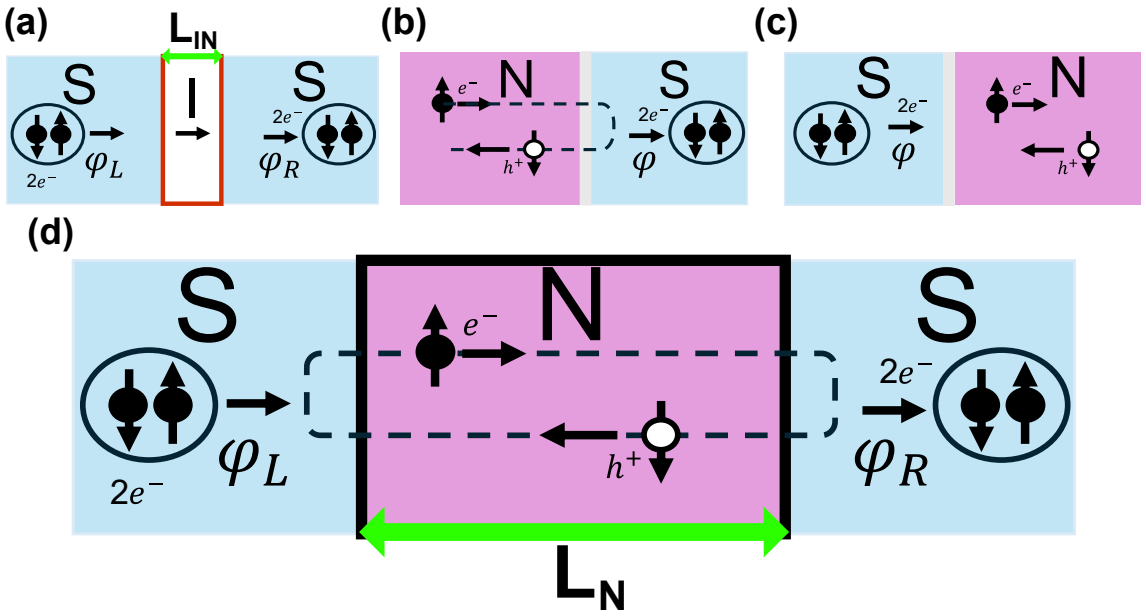

Figure 2.5: Fundamental transport mechanisms at superconducting interfaces and junctions. **(a)** Josephson tunnelling in a SIS junction, where the supercurrent is mediated by the coherent tunnelling of Cooper pairs across a thin insulating barrier. **(b)** Microscopic process of Andreev reflection at an NS interface: an incident electron from the normal region is retro-reflected as a hole of opposite spin and momentum, resulting in the transfer of a Cooper pair ($2e$) into the superconducting condensate. **(c)** Injection of Cooper pairs at a SN, illustrating the penetration of pairing correlations into the normal region via the proximity effect. **(d)** Formation of ABS in a SNS weak link. Phase-coherent, repeated Andreev reflections between the two superconducting leads establish a discrete sub-gap energy spectrum governed by the macroscopic phase difference $\phi = \phi_L - \phi_R$.

forming closed paths within the normal region. This allows the transport problem to be reformulated in terms of a discrete subgap excitation spectrum, whose energy levels depend on the superconducting phase difference. The resulting ABS provide a microscopic description of superconducting transport, with the supercurrent determined by the phase dispersion of these states.

The detailed structure of the ABS spectrum depends on the transmission properties of the junction, characterised by the transmission coefficient τ introduced in the BTK framework. In the short-junction limit, where the junction length L_N is smaller than the coherence length in the normal region ($L_N < \xi_N$), electron-hole correlations remain phase coherent across the weak link. For a ballistic junction, the corresponding coherence length is given approximately by

$$\xi_N = \frac{\hbar v_F^N}{\Delta'}, \tag{2.10}$$

where v_F^N is the Fermi velocity in the normal region and Δ' is the induced superconducting gap.

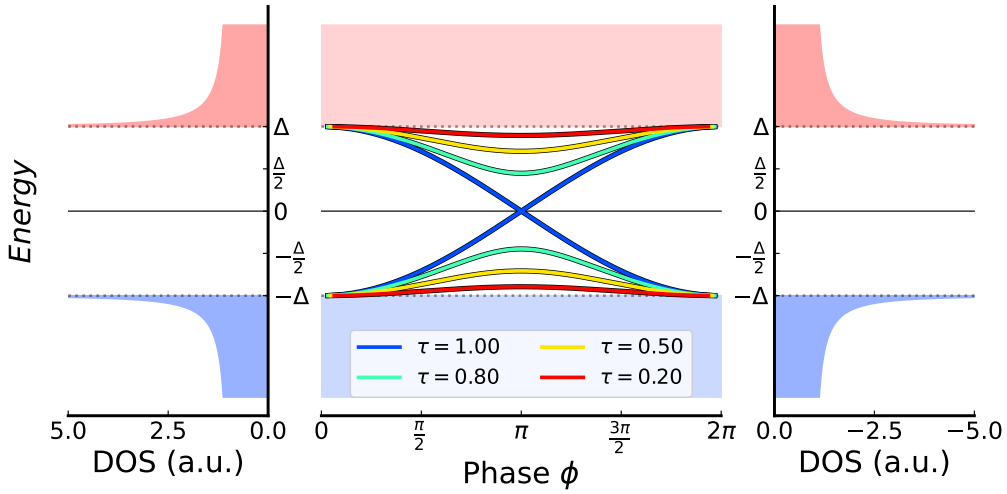

Figure 2.6: Andreev bound states and superconducting DOS in a short ballistic SNS junction. The central panel shows the phase-dependent ABS spectrum for a single conduction channel with transmission τ, as described by Eq. (2.11). Here, the induced gap in the weak link is assumed to equal the parent superconducting gap ($\Delta' = \Delta$). With increasing transparency, the ABS evolve from weakly dispersive states to strongly phase-dependent modes that approach zero energy at $\phi = \pi$ in the fully transparent limit ($\tau \to 1$). The left and right panels display the quasiparticle DOS in the superconducting leads, exhibiting a hard gap for $|E| < \Delta$ and coherence peaks at $\pm\Delta$. The color shading distinguishes occupied ($E < 0$) and unoccupied ($E > 0$) states.

In this regime, the subgap spectrum for a single transport channel is given by

$$E_{\pm}(\phi) = \pm\Delta'\sqrt{1 - \tau\sin^2(\phi/2)}, \tag{2.11}$$

where ϕ is the superconducting phase difference across the junction. This phase-dependent spectrum is illustrated in Fig. 2.6.

The supercurrent carried by these bound states follows directly from the phase dependence of the energy spectrum,

$$I_s(\phi) = \frac{2e}{\hbar}\frac{\partial E}{\partial \phi}. \tag{2.12}$$

Equation (2.11) describes a single transport channel with transmission τ. In realistic junctions, multiple conduction channels contribute to the total supercurrent, such that superconducting transport is determined by the collective phase dispersion of the occupied subgap states.

The properties of the resulting ABS spectrum depend sensitively not only on interface transparency, but also on the transport regime of the weak link itself, including the effects of junction length, disorder, and quasiparticle scattering. These considerations define distinct ballistic and diffusive transport regimes, which are discussed in the following section.

2.1.3 Transport Regimes

In mesoscopic Josephson junctions, superconducting transport is governed by several characteristic length and energy scales associated with quasiparticle scattering, phase coherence, and proximity-induced superconducting correlations within the weak link [56].

A central quantity is the elastic mean free path ℓ_e, which characterises the average distance a quasiparticle travels before its momentum is randomised by elastic scattering from impurities or disorder. The relation between the junction length L_N and ℓ_e distinguishes ballistic transport ($\ell_e \gg L_N$), in which quasiparticles propagate with minimal scattering, from diffusive transport ($\ell_e \ll L_N$), where transport occurs through multiple scattering events.

Even in the presence of elastic scattering, phase coherence can persist over a separate characteristic scale known as the phase coherence length l_ϕ. This length scale describes the distance over which the electronic phase remains well defined before being randomised by inelastic processes such as electron-electron or electron-phonon scattering. Phase-coherent transport phenomena, including Josephson transport and mesoscopic interference effects, require junction dimensions comparable to or smaller than l_ϕ.

At finite temperatures, thermal fluctuations can further suppress superconducting correlations over a characteristic thermal coherence length

$$\xi_T = \sqrt{\frac{\hbar D}{2\pi k_B T}}, \tag{2.13}$$

which describes the decay of phase-coherent superconducting transport at elevated temperatures, where $D = v_F \ell_e/3$ is the diffusion constant in the normal region. In practice, thermal effects become important when ξ_T becomes comparable to or shorter than either the junction length L_N or the intrinsic coherence length ξ_N.

Mesoscopic SNS junctions are commonly classified according to two independent criteria: the degree of quasiparticle scattering, distinguishing ballistic and diffusive transport, and the relation between the junction length and the superconducting coherence length in the weak link, distinguishing short and long junctions.

In hybrid SNS junctions, the relevant superconducting coherence length is the coherence length ξ_N within the proximitised normal region, which characterises the spatial extent over which electron-hole correlations remain phase coherent inside the weak link. The form of ξ_N depends on the transport regime.

In diffusive systems, superconducting correlations decay over a coherence length

$$\xi_N = \sqrt{\frac{\hbar D}{\Delta}}, \tag{2.14}$$

where D is the diffusion constant in the normal region. In ballistic systems, the corresponding coherence length is instead determined by the quasiparticle propagation velocity,

$$\xi_N = \frac{\hbar v_F^N}{\Delta}, \tag{2.15}$$

where v_F^N is the Fermi velocity in the weak link.

An equivalent energy scale for describing superconducting transport in mesoscopic weak links is the Thouless energy E_{Th}, which characterises the inverse dwell time of quasiparticles traversing the junction,

$$E_{\mathrm{Th}} \sim \frac{\hbar}{\tau_D}. \tag{2.16}$$

Physically, E_{Th} measures the characteristic energy associated with phase-coherent propagation through the weak link. In diffusive systems, quasiparticle motion is governed by multiple scattering events, giving a dwell time $\tau_D = \frac{L_N^2}{D}$ which yields

$$E_{\mathrm{Th}} = \frac{\hbar D}{L_N^2}. \tag{2.17}$$

In ballistic systems, the traversal time is instead determined by direct propagation across the junction $\tau_D \sim \frac{L_N}{v_F^N}$ leading to

$$E_{\mathrm{Th}} \sim \frac{\hbar v_F^N}{L_N}. \tag{2.18}$$

JJs are further classified as short or long depending on whether quasiparticles traverse the weak link on a timescale shorter or longer than the superconducting timescale $\hbar/\Delta$.

In ballistic systems, this criterion reduces to a comparison between the junction length and the coherence length ξ_N. Short ballistic junctions satisfy

$$L_N \ll \xi_N, \tag{2.19}$$

while long ballistic junctions satisfy

$$\xi_N \ll L_N \ll \ell_e. \tag{2.20}$$

In diffusive systems, the classification is more naturally expressed in terms of the Thouless energy. Short diffusive junctions satisfy

$$E_{\mathrm{Th}} \gg \Delta, \tag{2.21}$$

while long diffusive junctions correspond to

$$E_{\mathrm{Th}} \ll \Delta. \tag{2.22}$$

The corresponding characteristic scales and their influence on the $I_c R_N$ product are summarised in Table 2.1 and Table 2.2.

While the transport regimes discussed above determine how superconducting correlations propagate through a junction, the qualitative nature of the superconducting state is ultimately constrained by the symmetries of the system. In hybrid structures, time-reversal and inversion symmetries can be deliberately broken through SOC, magnetic fields, or magnetic proximity effects. These mechanisms modify the Andreev spectrum and enable phenomena beyond conventional superconductivity, including non-reciprocal transport and topological superconducting phases.

We therefore now turn to the role of symmetry breaking and its implications for topological superconductivity.

Table 2.1: Characteristic length and energy scales for mesoscopic SNS JJs [44, 99, 100]. Here, ξ_T represents the thermal coherence length, which governs the decay of the supercurrent at elevated temperatures [43].

Transport	Junction	Length	Characteristic scales		
			ξ_N	ξ_T	E_{Th}
Ballistic	Short	$L \ll \xi_N$	$\hbar v_F^N/\Delta$	$\hbar v_F^N/k_B T$	$\hbar v_F^N/L$
	Long	$\xi_N \ll L \ll \ell_e$			
Diffusive	Short	$\ell_e \ll L \ll \xi_{\mathrm{N}}$	$\sqrt{\hbar D/\Delta}$	$\sqrt{\hbar D/2\pi k_B T}$	$\hbar D/L^2$
	Long	$L \gg \xi_{\mathrm{N}}$			

Table 2.2: Theoretical limits for the $I_c R_N$ product at $T = 0$ [101]. The diffusive (dirty) short-junction limit follows the Kulik-Omelyanchuk (KO-1) theory [102], while the ballistic (clean) short-junction limit is given by the KO-2 result [103]. The long-junction limits depend on E_{Th}, with the diffusive constant derived by Dubos et al. [99].

Transport regime	Short junction ($E_{\mathrm{Th}} \gg \Delta$)	Long junction ($E_{\mathrm{Th}} \ll \Delta$)
Ballistic	$I_c R_N = \pi\Delta/e$	$I_c R_N \sim E_{\mathrm{Th}}/e$
Diffusive	$I_c R_N \approx 2.07\,\Delta/e$	$I_c R_N \approx 10.82\,E_{\mathrm{Th}}/e$

2.2 Symmetry Breaking and Topological Emergence

The preceding sections have established how superconducting transport in hybrid JJs is governed by interface transparency, coherence lengths, and the resulting Andreev bound state spectrum. These considerations determine how superconducting correlations propagate through a device and how phase-coherent transport is established.

However, the qualitative nature of the superconducting state is not determined by these factors alone. In particular, the structure of the Andreev spectrum-and the possibility of realising unconventional or topological phases-is fundamentally constrained by the symmetries of the system.

In conventional superconductors, the simultaneous presence of TRS, IS, and spin degeneracy enforces a symmetric quasiparticle dispersion spectrum and conventional s-wave pairing. Breaking these symmetries lifts degeneracies, modifies the dispersion of quasiparticles, and can qualitatively alter the superconducting ground state.

In hybrid systems, such symmetry breaking can be engineered in a controlled manner through SOC, magnetic fields, or magnetic proximity effects. These ingredients are not only responsible for phenomena such as non-reciprocal transport and anomalous Josephson effects, but also form the essential building blocks required to realise topological superconductivity which will be discussed in Sec. 2.2.2.

In the following, we first introduce the microscopic mechanisms of SOC and Zeeman interactions, and then show how their interplay reshapes the Andreev spectrum, ultimately

Figure 2.7: Schematic of the hybrid nanowire platform. The orientation of the nanowire ($\hat{x}$) and the resulting Rashba field ($\hat{y}$) establish the basis for the asymmetric dispersion relations ($B \parallel B_{SO}$) and topological gap opening ($B \perp B_{SO}$) discussed in Sec. 2.2.1. Note that the effective Rashba field is assumed to be oriented along $\hat{y}$ (perpendicular to the NW) for simplicity's sake; as discussed in Paper III, this orientation is not necessarily reflected in realistic devices.

enabling the emergence of MBS.

2.2.1 Spin-Orbit Coupling and Zeeman Effects

Throughout this section, we adopt a dimensionless representation by normalising energy to the Rashba energy E_{SO} and momentum to k_{SO}. Details concerning these parameters follow below. These parameters define the characteristic energy and momentum scales associated with Rashba spin splitting, illustrated in Fig. 2.8(b), providing a consistent scale for comparing Zeeman and superconducting energy contributions.

To understand how symmetry breaking modifies superconducting transport, it is useful to begin from a minimal one-dimensional electron system and introduce the relevant physical ingredients step by step.

We first consider a spin-degenerate free-electron dispersion,

$$E(k) = \frac{\hbar^2 k^2}{2m}, \tag{2.23}$$

shown in Fig. 2.8(a), where k is the electron wave vector and m is the effective electron mass. In the absence of spin-dependent interactions, each momentum state remains doubly degenerate in spin [70].

Rashba spin-orbit coupling. In systems lacking inversion symmetry, electronic states with opposite momentum are no longer required to remain spin degenerate. This asymmetry allows SOC to generate momentum-dependent spin splitting of the electronic bands. Microscopically, SOC originates from relativistic corrections to electron motion and can be derived from the Dirac equation in the non-relativistic limit [104, 105]. In semiconductor nanowires, the dominant contribution is typically Rashba SOC, which arises from structural inversion asymmetry at interfaces or from external electric fields.

In general, IS breaking in semiconductors can originate either from the crystal lattice itself, leading to bulk inversion asymmetry (BIA) and the Dresselhaus effect [106], or

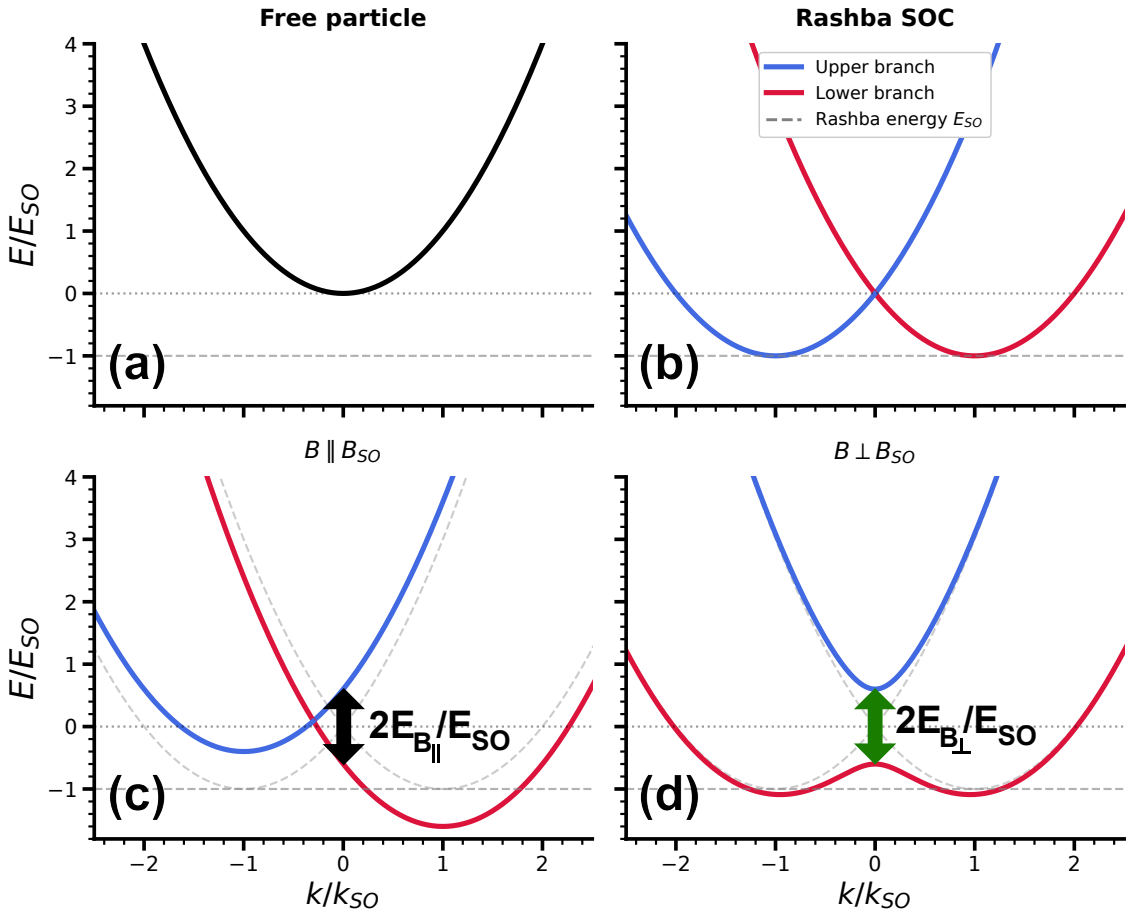

Figure 2.8: Evolution of the 1D band structure under SOC and Zeeman fields. **(a)** Spin-degenerate free-electron dispersion. **(b)** Rashba SOC ($E_{\mathrm{SO}} = m\alpha^2/2\hbar^2$) lifts spin degeneracy into helical branches. **(c)** A field parallel to the SOC field ($B_y = 0.6E_{\mathrm{SO}}$) shifts the Rashba-split branches in momentum space, shifting the crossing point to $k = -0.3k_{\mathrm{SO}}$ and resulting in an asymmetric dispersion where $v_{F1} \neq v_{F2}$. **(d)** A perpendicular field ($B_x = 0.6E_{\mathrm{SO}}$) opens a Zeeman gap of $1.2E_{\mathrm{SO}}$ at $k = 0$. All energies and momenta are normalised to E_{SO} and $k_{\mathrm{SO}} = m\alpha/\hbar^2$, respectively.

from asymmetry in the confining potential, giving rise to structure inversion asymmetry (SIA) and the Rashba effect [107]. In InAs NW systems, the Dresselhaus contribution is typically weak and often neglected [72], such that the spin-orbit interaction is well described by the Rashba term alone. Importantly, the Rashba coupling strength α can be tuned via external electrostatic gates [108, 109], providing experimental control over spin-dependent transport properties [59].

For a quasi-one-dimensional NW oriented along the x-direction, as illustrated schematically in Fig. 2.7, the Rashba interaction can be projected onto an effective one-dimensional form,

$$H_{\mathrm{SOC}} = -\alpha k_x \sigma_y, \tag{2.24}$$

where α is the Rashba spin-orbit coupling strength, k_x is the electron momentum along the nanowire axis, and σ_y is the Pauli matrix describing spin along the transverse $\hat{y}$

direction. This corresponds to an effective momentum-dependent spin-orbit field

$$\mathbf{B}_{\mathrm{SO}}(k) \propto k_x \hat{\mathbf{y}}. \tag{2.25}$$

Here, the nanowire axis defines the propagation direction $\hat{x}$, while the effective Rashba field is assumed to point along $\hat{y}$ due to structural confinement and inversion asymmetry transverse to the wire. More generally, the spin-orbit field follows $\mathbf{B}_{\mathrm{SO}} \propto \mathbf{k} \times \mathbf{E}$ and therefore depends on the local electric field environment. In realistic hybrid NW devices, gate-induced electric fields, interface asymmetries, and device geometry can significantly modify the direction and magnitude of the effective Rashba field, such that it is not necessarily strictly perpendicular to the wire axis, as discussed further in Paper III.

In quasi-one-dimensional systems, however, strong transverse confinement restricts the electronic motion to a single propagation direction. The spin-orbit interaction can therefore be projected onto a single dominant component, yielding an effective one-dimensional description that captures the relevant low-energy physics.

Diagonalising the Hamiltonian yields the dispersion

$$E_{\pm}(k_x) = \frac{\hbar^2 k_x^2}{2m} \pm \alpha k_x, \tag{2.26}$$

as shown in Fig. 2.8(b). In this regime, the spin expectation value aligns with the effective spin-orbit field, resulting in spin-momentum locked branches in which the spin orientation depends on the direction of motion [107, 110]. The characteristic momentum and energy scales associated with the Rashba interaction are defined as:

$$k_{\mathrm{SO}} = \frac{m\alpha}{\hbar^2}, \quad E_{\mathrm{SO}} = \frac{m\alpha^2}{2\hbar^2}. \tag{2.27}$$

Physically, k_{SO} represents the momentum offset of the band minima, while E_{SO} corresponds to the energy depth of the resulting helical wells relative to the crossing point at $k = 0$.

Zeeman interaction. The spin structure generated by Rashba SOC can be modified through the application of an external magnetic field, which couples to the electron spin through the Zeeman interaction,

$$H_Z = \frac{1}{2} g \mu_B \mathbf{B} \cdot \boldsymbol{\sigma}, \tag{2.28}$$

where g is the effective Landé g-factor, μ_B is the Bohr magneton, $\mathbf{B}$ is the applied magnetic field, and $\boldsymbol{\sigma} = (\sigma_x, \sigma_y, \sigma_z)$ denotes the Pauli spin matrices [20, 111–113]. The corresponding Zeeman energy is

$$E_Z = \frac{1}{2} g \mu_B B. \tag{2.29}$$

The effect of the magnetic field depends sensitively on its orientation relative to the effective Rashba field shown schematically in Fig. 2.7. For a quasi-one-dimensional NW oriented along $\hat{x}$ with an effective Rashba field $\mathbf{B}_{\mathrm{SO}} \parallel \hat{y}$, a magnetic field applied parallel to the spin-orbit field (B_y) shifts the spin-split bands in momentum space, breaking IS and producing an asymmetric dispersion relation, as illustrated in Fig. 2.8(c). This asymmetry

leads to different Fermi velocities for left- and right-moving quasiparticles ($v_{F1} \neq v_{F2}$), which forms the basis for non-reciprocal transport phenomena such as the Josephson diode effect [113].

In contrast, a magnetic field applied perpendicular to the spin-orbit field but parallel to the NW axis (B_x) hybridises the spin-split branches and opens a gap at $k = 0$, as shown in Fig. 2.8(d). This field configuration lifts the degeneracy at $k = 0$ and forms a key ingredient for realising topological superconductivity in proximitised nanowires.

Combining the kinetic, Rashba SOC, and Zeeman contributions yields the effective single-particle Hamiltonian

$$H = \frac{\hbar^2 k^2}{2m} - \alpha k \sigma_y + B_x \sigma_x + B_y \sigma_y, \tag{2.30}$$

which forms the basis for describing spin-orbit-coupled semiconductor NW systems.

Proximity-induced superconductivity. To describe superconducting correlations in these systems, it is convenient to use the Bogoliubov-de Gennes (BdG) formalism, in which electron and hole excitations are treated within a unified framework [3, 114]. This approach captures the hybridisation of electron and hole states induced by superconducting pairing, resulting in a particle-hole symmetric excitation spectrum.

When the NW is proximity-coupled to an s-wave superconductor, the system can be described by an effective BdG Hamiltonian of the form

$$\mathcal{H}_{\mathrm{BdG}} = \left(\frac{\hbar^2 k^2}{2m} - \mu - \alpha k \sigma_y \right) \tau_z + B_x \sigma_x + B_y \sigma_y + \Delta \tau_x, \tag{2.31}$$

where μ is the chemical potential, Δ is the induced superconducting gap, and σ and τ are Pauli matrices acting in spin and particle-hole space [115].

This model constitutes the minimal microscopic description of a proximitised spin-orbit-coupled NW and forms the basis for both symmetry-broken Josephson effects and topological superconductivity. In particular, it underlies theoretical proposals for realising MBS in semiconductor-superconductor hybrid systems [27, 28]. Discussed more in detail in Sec. 2.2.2.

2.2.2 Consequences of Symmetry Breaking in Hybrid Junctions

The combination of SOC, Zeeman splitting, and superconducting pairing not only enables a transition to a topological phase, but also qualitatively modifies the Andreev bound state spectrum already in the topologically trivial regime.

Depending on the strength and interplay of these ingredients, two distinct physical regimes can be identified. For moderate Zeeman fields, symmetry breaking leads to asymmetric ABS and anomalous Josephson effects, including phase shifts and non-reciprocal transport. At larger Zeeman energies, the system may enter a topological superconducting regime associated with the emergence of MBS localised near its boundaries.

These regimes are discussed separately in the following sections.

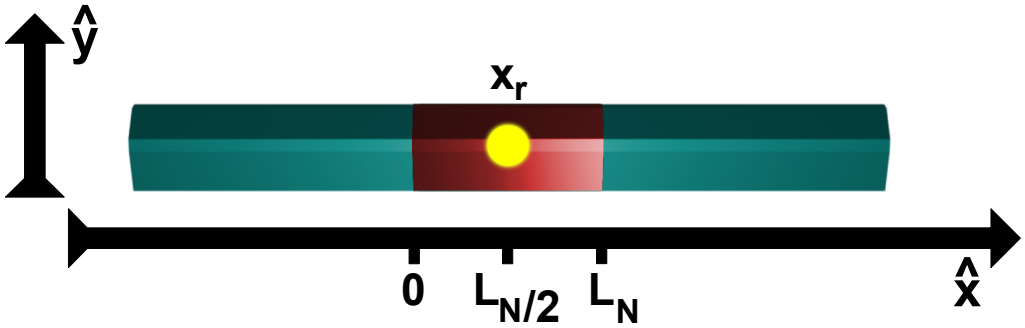

Figure 2.9: Schematic of a hybrid nanowire Josephson junction used to illustrate finite-length and symmetry-breaking effects in the Andreev bound state spectrum. A superconducting nanowire (blue) contains a weak link of length L_N (red) extending from $x = 0$ to $x = L_N$. A scattering centre located at position $x = x_r$ (yellow dot) breaks spatial symmetry within the junction and contributes to asymmetric quasiparticle phase accumulation in the presence of spin-orbit coupling and magnetic fields.

Asymmetric Andreev Bound States and Anomalous Josephson Effects

For a finite-length junction containing a scattering centre at position x_r, illustrated schematically in Fig. 2.9, the ABS spectrum can be described within a scattering matrix formalism [116, 117]. In finite-length Josephson junctions, the ABS spectrum depends not only on the superconducting phase difference, but also on the dynamical phase accumulated by quasiparticles traversing the weak link. When the junction length L_N becomes comparable to the coherence length ξ_N or the spin-orbit length

$$\ell_{\mathrm{SO}} = \frac{\hbar^2}{m\alpha}, \tag{2.32}$$

finite propagation effects qualitatively modify the ABS dispersion.

Within this framework, the ABS energies E are determined by a resonance condition that incorporates both the superconducting phase difference ϕ and the finite propagation time across the weak link. For a single-channel junction with a scattering barrier located at a relative position $x = x_r L_N$, $x_r \in [0, 1]$ (where $x_r = 0.5$ corresponds to a scatterer located at the centre of the junction, which is the configuration considered in the following discussion), the ABS spectrum is given by

$$\begin{aligned} &\tau \cos\left[(\lambda_1 - \lambda_2)\varepsilon + \phi\right] \\ &+ (1-\tau)\cos\left[(\lambda_1 + \lambda_2)\varepsilon x_r\right] \\ &= \cos\left[2\arccos(\varepsilon) - (\lambda_1 + \lambda_2)\varepsilon\right], \end{aligned} \tag{2.33}$$

where $\varepsilon = E/\Delta$ is the normalised ABS energy and τ is the transmission probability of the junction. The quantities

$$\lambda_{1,2} = \frac{L_N \Delta}{\hbar v_{F1,2}} \tag{2.34}$$

describe the dimensionless dynamical phase accumulated by right- and left-moving quasiparticles with Fermi velocities $v_{F1,2}$, respectively.

The evolution of the ABS spectrum is illustrated in Fig. 2.10. In the short-junction limit shown in Fig. 2.10(a), the ABS dispersion is symmetric and closely resembles the conventional short-junction result (see Appendix B). Introducing a finite junction length, Fig. 2.10(b), enhances the role of dynamical phase accumulation and leads to a flattening of the ABS branches near the superconducting gap edges.

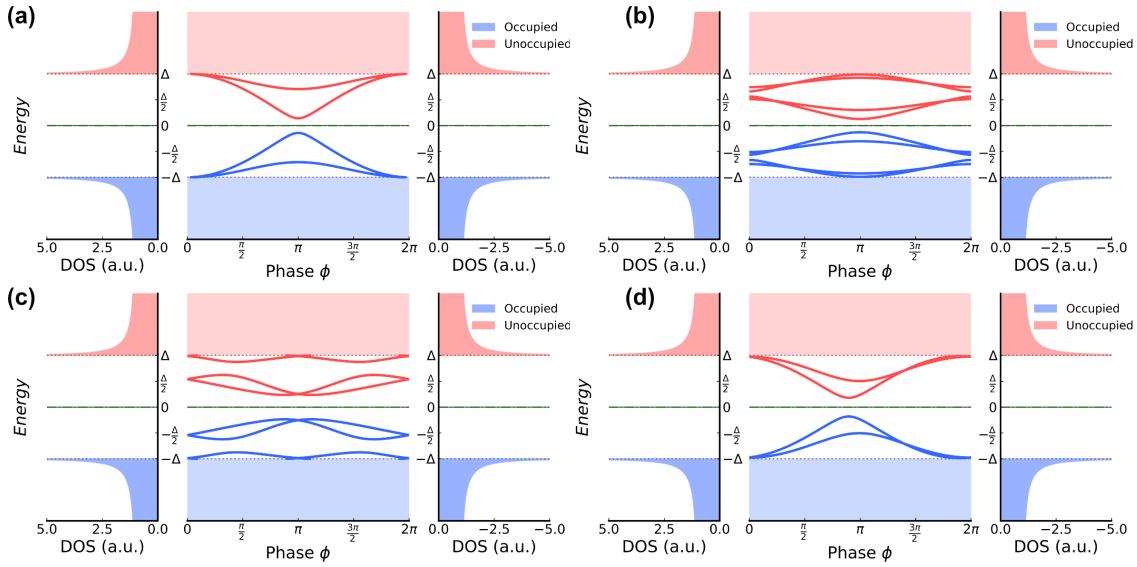

Figure 2.10: Evolution of the ABS spectrum under finite-length effects, asymmetric phase accumulation, and broken symmetries. Calculated using the transcendental ABS relation in Eq. (2.33) and the Yokoyama model [111, 112]. **(a) Short-junction limit:** Symmetric ABS spectra for $\lambda_1 = \lambda_2 = 0$, corresponding to negligible dynamical phase accumulation across the junction. Two transmission probabilities are shown, $\tau = 0.98$ and $\tau = 0.5$, illustrating the evolution from strongly dispersive to weakly dispersive ABS branches with decreasing transparency. **(b) Finite-length regime:** Finite propagation phases $\lambda_1 = \lambda_2 = 1.5$ with scattering position $x_r = 0.5$ lead to flattened ABS branches near the superconducting gap edges. The avoided crossings near $\phi = 0$ and $\phi = 2\pi$ arise from finite backscattering ($\tau \neq 1$) [117]. **(c) Asymmetric phase accumulation:** Unequal dynamical phases for opposite propagation directions ($\lambda_1 = 1.8$, $\lambda_2 = 0.2$ and vice versa) with $\tau = 0.78$ generate a tilted "W"-shaped ABS spectrum. This phenomenologically captures the effect of inversion-symmetry breaking and asymmetric quasiparticle propagation while preserving phase-reversal symmetry $E(\phi) = E(-\phi)$. **(d) Broken IS and TRS (Yokoyama model):** The combined presence of SOC and Zeeman coupling produces a phase-shifted ABS spectrum described by Eqs. (2.35) and (2.36). The calculations use transmission probabilities $T = 0.95$ and 0.7, SOC parameters $\epsilon_{SO} = 0.8$ and 0.5, Zeeman phase parameters $\theta_B = 1.5$ and 0.8, and asymmetry parameters $\alpha_B = \sqrt{3}$ and 1.1. The induced phase shift $\delta\theta \propto \theta_B(\alpha_B - 1)/(\alpha_B + 1)$ breaks phase-reversal symmetry, producing a skewed ABS dispersion and a non-reciprocal current-phase relation associated with the JDE.

Additional modifications arise when IS is broken through either the presence of Rashba SOC and/or Zeeman coupling. In this case, left- and right-moving quasiparticles acquire

different Fermi velocities ($v_{F1} \neq v_{F2}$), resulting in unequal phase accumulation factors ($\lambda_1 \neq \lambda_2$). As illustrated in Fig. 2.10(c), unequal dynamical phase accumulation for opposite propagation directions produces tilted "W"-shaped ABS dispersions characteristic of inversion-symmetry-broken transport. In systems where both IS and TRS are broken, the current-phase relation can become shifted away from the conventional sinusoidal form. In particular, the junction may acquire a finite ground-state phase offset ϕ_0, leading to a so-called ϕ_0 junction characterised by a finite supercurrent at zero phase bias.

A phenomenological description of the interplay between SOC and Zeeman coupling was developed by Yokoyama *et al.* [111, 112]. Within this framework, finite junction length and asymmetric quasiparticle propagation generate an additional phase shift in the ABS spectrum when both inversion and TRS are broken. The ABS energies are described by

$$E_{\pm}(\phi) = \pm\Delta\sqrt{\frac{1+\Gamma(\phi)}{2}}, \tag{2.35}$$

where the modulation function $\Gamma(\phi)$ accounts for the different transport contributions and takes the form

$$\Gamma(\phi) = T(1-\epsilon_{SO})\cos(\phi) + (1-T)\cos(\theta_B) + T\epsilon_{SO}\cos(\phi+\delta\theta). \tag{2.36}$$

Here, T is the transmission probability, ϵ_{SO} parametrises the SOC strength, and θ_B describes the Zeeman-induced phase accumulation. The additional phase shift $\delta\theta$ phenomenologically captures the asymmetry between opposite propagation directions induced by the combined action of SOC and magnetic fields.

As shown in Fig. 2.10(d), the phase shift $\delta\theta$ removes the phase-reversal symmetry of the ABS spectrum such that

$$E(\phi) \neq E(-\phi). \tag{2.37}$$

Consequently, the ABS dispersion becomes intrinsically non-reciprocal.

Because the supercurrent is determined by the phase derivative of the ABS energies,

$$I(\phi) \propto \sum_n \partial_\phi E_n, \tag{2.38}$$

the asymmetry of the ABS spectrum directly produces a non-reciprocal current-phase relation. The resulting difference between positive and negative critical currents constitutes the microscopic origin of the Josephson diode effect.

Orbital Effects from external fields Orbital coupling to an external magnetic field can generate finite-momentum pairing and non-reciprocal superconducting transport even in the absence of strong SOC [118]. A magnetic field perpendicular to the junction induces screening currents in the superconducting leads, producing a spatially varying superconducting phase

$$\phi(x) = \phi_0 + qx, \tag{2.39}$$

where q is the induced phase gradient. In junctions with finite width, this spatial phase modulation breaks inversion symmetry and provides an additional mechanism for generating a non-reciprocal critical current [34].

The Role of Higher Harmonics Even when both TRS and IS are broken, a finite diode effect requires a non-sinusoidal CPR. A purely sinusoidal CPR, even when phase-shifted by a finite ϕ_0, remains symmetric in its extrema ($I_{c+} = |I_{c-}|$) and therefore does not yield a non-reciprocal response. This is illustrated by the red curve in Fig. 2.11, where a phase shift of $\phi_0 = 0.3\pi$ is introduced:

$$I(\phi) = I_1 \sin(\phi + \phi_0). \tag{2.40}$$

While this relation describes a ϕ_0-junction where the supercurrent is finite at zero phase difference, the magnitude of the critical current is identical in both directions.

A genuine diode effect requires higher harmonic contributions to the supercurrent [101, 119], typically expressed as:

$$I(\phi) = \sum_{n=1}^{\infty} I_n \sin(n\phi + \phi_n) = I_1 \sin(\phi + \phi_0) + I_2 \sin(2\phi + \phi_1) + \cdots \tag{2.41}$$

The inclusion of a second harmonic I_2 introduces a skewness into the CPR that allows the positive and negative extrema to differ. Physically, these higher-order terms originate from high junction transparency ($\tau \to 1$) and finite-length effects, where multiple Andreev reflections contribute significantly to the transport.

As shown by the green curve in Fig. 2.11, a second harmonic component of $I_2 = 0.3I_1$ with a relative phase shift $\phi_1 = 0.05\pi$ is sufficient to break the symmetry of the critical currents. This results in a non-reciprocal supercurrent where $I_{c+} \neq |I_{c-}|$.

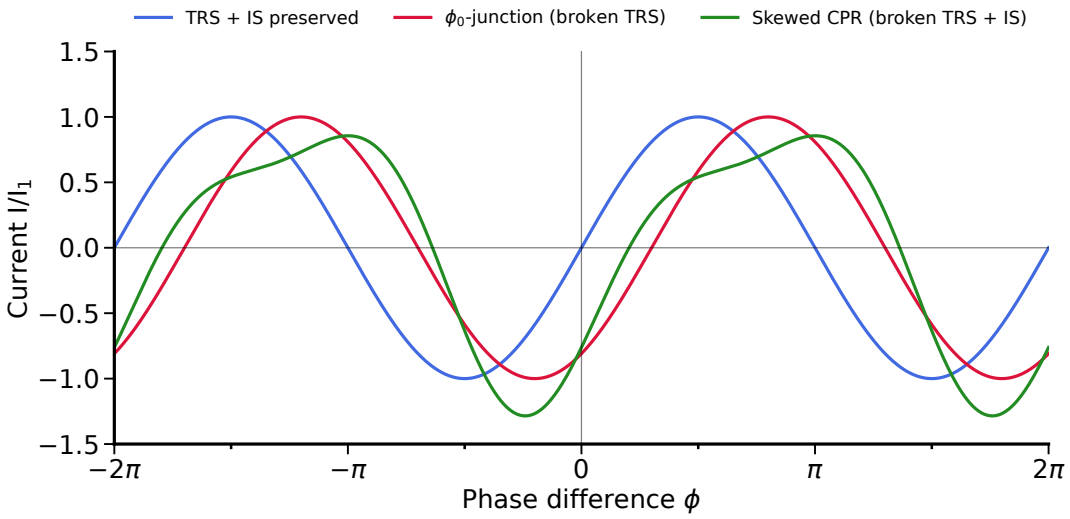

Figure 2.11: Current-phase relations (CPR) under different symmetry conditions. All currents are normalised to the primary critical current I_1. **Blue curve:** Conventional Josephson relation $I(\phi) = \sin\phi$, preserving both TRS and IS. **Red curve:** A ϕ_0-junction with $\phi_0 = 0.3\pi$. Despite the phase shift, the relation remains symmetric ($I_{c+} = |I_{c-}| = 1$). **Green curve:** A skewed CPR with broken TRS and IS, incorporating a second harmonic $I_2 = 0.3$ and $\phi_1 = 0.05\pi$. The resulting asymmetry ($I_{c+} \neq |I_{c-}|$) constitutes the origin of the JDE.

This establishes the direct connection between symmetry breaking at the microscopic

level and the emergence of non-reciprocal superconducting transport, providing the foundation for the JDE discussed in Sec. 2.3.3.

Topological Superconductivity and Majorana Bound States

The Hamiltonian in Eq. (2.31) provides a minimal framework for describing the emergence of topological superconductivity in spin-orbit-coupled NWs. As the Zeeman energy V_Z ($V_Z = E_Z$ as defined in Eq. (2.29)) is increased, the system undergoes a topological phase transition characterised by the closing and reopening of the bulk excitation gap. For a homogeneous system, the gap closing occurs at $k = 0$, where the competition between Zeeman splitting, chemical potential, and superconducting pairing is most pronounced. Evaluating the spectrum yields the criterion for the lowest subband

$$V_Z = \sqrt{\mu^2 + \Delta^2}, \tag{2.42}$$

which marks the transition between trivial and topological superconducting phases. For $V_Z > \sqrt{\mu^2 + \Delta^2}$, the gap reopens with an inverted band character, signalling entry into the topological regime [27, 28].

The evolution of the spectrum across this transition, described by Eq. (2.31) and governed by Eq. (2.42), is illustrated in Fig. 2.12. In the absence of a Zeeman field (a), superconducting pairing opens a full gap in the Rashba-split spectrum. The faint grey curves indicate the underlying normal-state Rashba bands in the absence of superconductivity. As the Zeeman field is increased (b), the excitation gap at $k = 0$ gradually decreases while the system remains in the trivial superconducting regime for $V_Z < \sqrt{\mu^2 + \Delta^2}$. At the critical point (c), the gap closes at $k = 0$, signalling the topological phase transition. For $V_Z > \sqrt{\mu^2 + \Delta^2}$ (d), the gap reopens with inverted band character, indicating the emergence of the topological superconducting phase.

Physically, this transition reflects the formation of an effectively spinless, helical system in which superconducting pairing acquires an effective p-wave character. While the parent superconductor remains s-wave, the combination of SOC and Zeeman splitting removes spin degeneracy and enforces pairing between states with locked spin and momentum, realising the conditions for a one-dimensional topological superconductor [18, 120].

We emphasise that the same ingredients, SOC and Zeeman splitting, that enable the topological phase transition are also responsible for the symmetry-broken Josephson effects discussed in Sec. 2.2.2. In particular, a Zeeman field component parallel to the spin-orbit field gives rise to asymmetric quasiparticle propagation and anomalous phase shifts, while a perpendicular component is required to open the gap at $k = 0$ and drive the system into the topological regime. The distinction between these effects therefore lies not in the underlying mechanisms, but in their relative strength and orientation.

A defining consequence of this phase is the emergence of MBS at the boundaries of the system. In a NW geometry, these boundaries correspond to the interfaces between topological and trivial regions, such as the physical ends of the wire or junction interfaces where the chemical potential or pairing potential changes. These states are localised near the boundaries and decay into the bulk over a length scale set by the coherence length. Importantly, they appear at zero energy and are protected by the bulk topological gap.

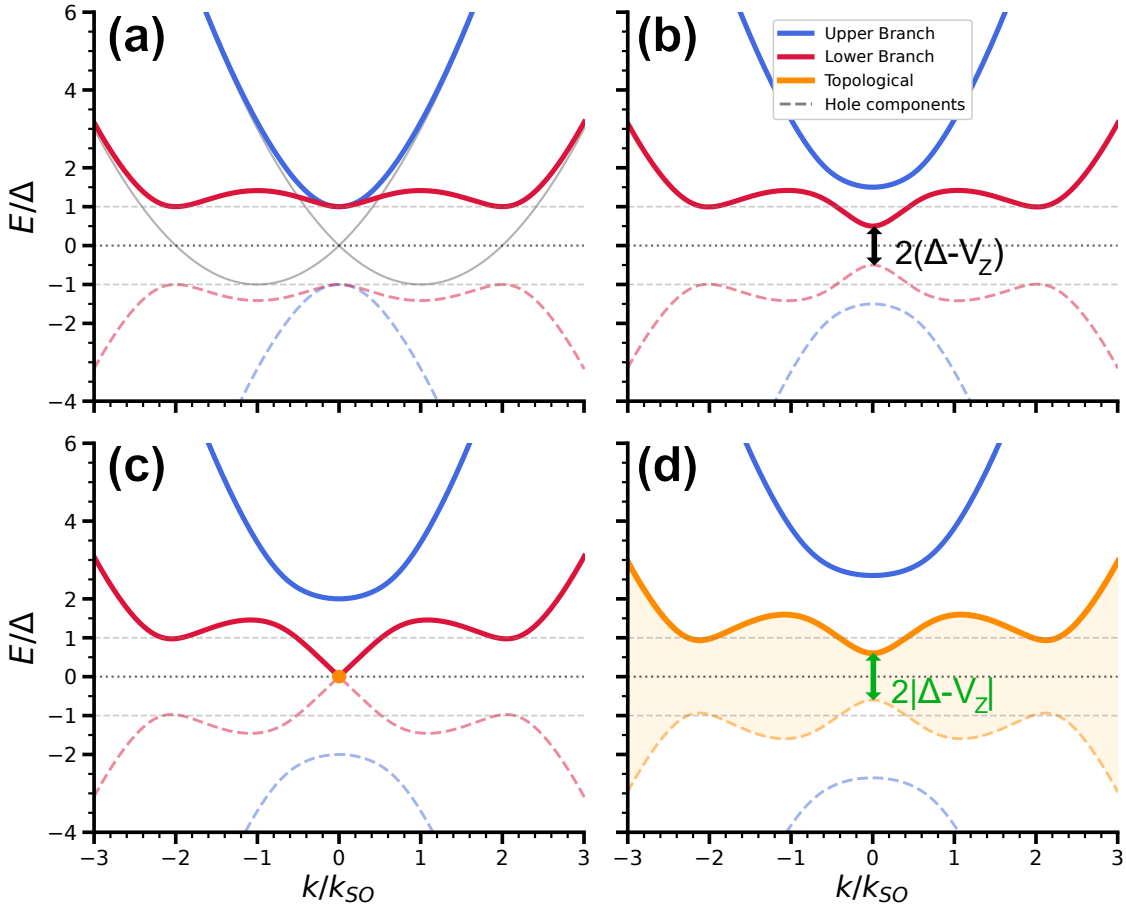

Figure 2.12: Evolution of the BdG spectrum and the topological phase transition in a 1D Rashba NW. Energy spectra are normalised by the induced superconducting gap Δ and plotted against the normalised momentum k/k_{SO} with the chemical potential $\mu = 0$ for all cases. **(a) Superconducting state with SOC:** In the absence of a Zeeman field ($B_x = 0$), the electron and hole branches are separated by the full superconducting gap of 2Δ. Dashed lines represent the hole-like components, faint grey solid lines show SOC states in absence of superconductivity. **(b) Trivial superconducting phase:** As a Zeeman field is introduced ($B_x/\Delta = 0.5$), the gap at $k = 0$ begins to shrink. The remaining trivial gap, given by $2(\Delta - B_x)$, is indicated by the **black arrow**. **(c) Topological critical point:** At $B_x/\Delta = 1.0$, the Zeeman energy exactly compensates the pairing potential, causing the gap to close at the zone centre. This transition point is marked by an **orange dot** at $(k, E) = (0, 0)$. **(d) Topological superconducting phase:** In the high-field regime ($B_x/\Delta = 1.6$), the gap re-opens with an inverted band character (orange branches). The size of this topological gap, $2|B_x - \Delta|$, is indicated by a **green arrow** at $k = 0$. In a finite-length wire, this phase supports Majorana zero modes localised at the boundaries.

In transport experiments where two adjacent nanowires host MBS and nearby MBS combine through a normal region into an ABS spectrum [20], Majorana modes are expected to manifest through characteristic signatures such as zero-bias conductance peaks

[121, 122], modified CPRs, and the fractional Josephson effect.

In a conventional JJ, the ABS spectrum is 2π-periodic in the superconducting phase difference ϕ. In contrast, in a topological junction hosting Majorana modes, a protected zero-energy crossing leads to an energy-phase relation

$$E(\phi) = \pm\Delta\sqrt{T_N}\cos\left(\frac{\phi}{2}\right), \tag{2.43}$$

where T_N is the normal region transparency, which is 4π-periodic in ϕ [60, 123]. This crossing is protected by fermion parity conservation, preventing hybridisation at $\phi = \pi$.

The distinction between trivial and topological energy-phase relations is shown in Fig. 2.13. For finite transmission ($\tau < 1$), conventional Andreev states remain gapped and 2π-periodic. At perfect transmission ($\tau = 1$), a zero-energy crossing can occur, but it is not protected and can be lifted by perturbations. In contrast, the topological crossing is robust and directly tied to fermion parity conservation.

In practice, quasiparticle poisoning and other relaxation processes can break parity conservation, restoring an effective 2π periodicity in time-averaged measurements.

Experimentally, topological states in JJs can manifest as the suppression of odd Shapiro steps in microwave-driven devices, as observed in semiconductor NWs [124]. However, it is important to note that such fractional Josephson signatures are not unique to topological systems. Similar effects can arise from non-topological mechanisms, such as Landau-Zener transitions in highly transparent trivial junctions [48]. Consequently, these signatures must be interpreted with care and in conjunction with other experimental observables.

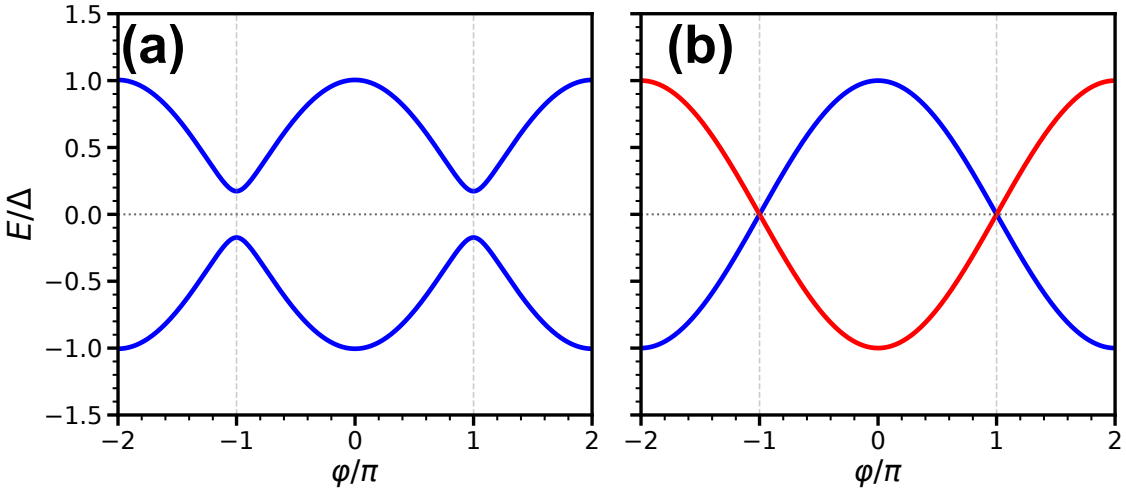

Figure 2.13: Comparison of trivial and topological energy-phase relations. **(a)** Conventional Andreev bound states exhibit a gapped, 2π-periodic dispersion ($\tau < 1$). **(b)** In a topological junction, a protected zero-energy crossing leads to a 4π-periodic contribution to the spectrum due to fermion parity conservation [48, 123]. Note, here the junction has perfect transparency.

Recent experimental efforts have moved beyond initial transport signatures toward controlled realisations and readout of Majorana modes. Engineered minimal Kitaev chains, consisting of a small number of coupled superconducting islands, provide a platform where

fermion parity and its dynamics can be directly probed [125–127]. These capabilities are central for topological quantum computation [18, 24, 128].

Advances in hybrid semiconductor platforms, including NW-based devices and two-dimensional electron gas (2DEG) systems, have further improved material quality and scalability. The use of epitaxial superconductors combined with electrostatic gating enables the creation of well-defined topological regions and tuneable junctions [19, 69, 129].

A key recent development is single-shot parity readout, providing direct access to the non-local degrees of freedom associated with Majorana modes. Interferometric measurements in InAs-Al hybrid devices have demonstrated parity-sensitive readout [130], while minimal Kitaev chain implementations enable time-resolved parity detection [127]. These advances are crucial for distinguishing true topological Majorana states from trivial low-energy excitations.

These developments reflect a broader shift from purely spectroscopic signatures toward phase-coherent and parity-sensitive probes of Majorana physics.

It is important to note that while a single pair of MBS emerges at the ends of a topological segment, the implementation of topological qubits and non-Abelian operations requires multiple spatially separated Majorana modes, typically arranged in networks or coupled pairs [18, 126].

While the concepts discussed in this section are closely related to the physical systems investigated in this thesis, no direct experimental signatures of MBS are reported here. Instead, the focus of the following chapters is on JJs in large Zeeman fields, symmetry-broken superconducting transport, and Josephson physics in TIs, which provide the necessary foundation for future investigations of topological superconductivity.

2.3 Experimental Probes and Interference Phenomena

The preceding sections established how superconducting transport in hybrid NW systems is governed by ABS, and how symmetry breaking through SOC and Zeeman fields modifies their spectrum, giving rise to phenomena such as anomalous Josephson effects and topological superconductivity.

Experimentally accessing this physics requires probing both the relevant energy scales and the phase-coherent transport processes that govern these effects. In practice, this is achieved through a hierarchy of transport measurements, ranging from basic spectroscopy of the superconducting gap and interface transparency to phase-sensitive measurements that reveal interference, coherence, and symmetry breaking.

We begin by establishing the fundamental transport characteristics of the JJs used in this work. These measurements provide direct access to key parameters such as the superconducting gap (Δ), the normal-state resistance (R_n), and the interface transparency, which strongly influence the ABS spectrum discussed in Sec. 2.2.1 and Sec. 2.2.2.

The measurement configuration plays an important role in determining which transport properties are most directly accessible experimentally. As shown in Fig. 2.14(a-b), voltage-biased measurements provide direct access to quasiparticle tunnelling and the superconducting density of states in SIS junctions. The I-V trace yields the normal-state

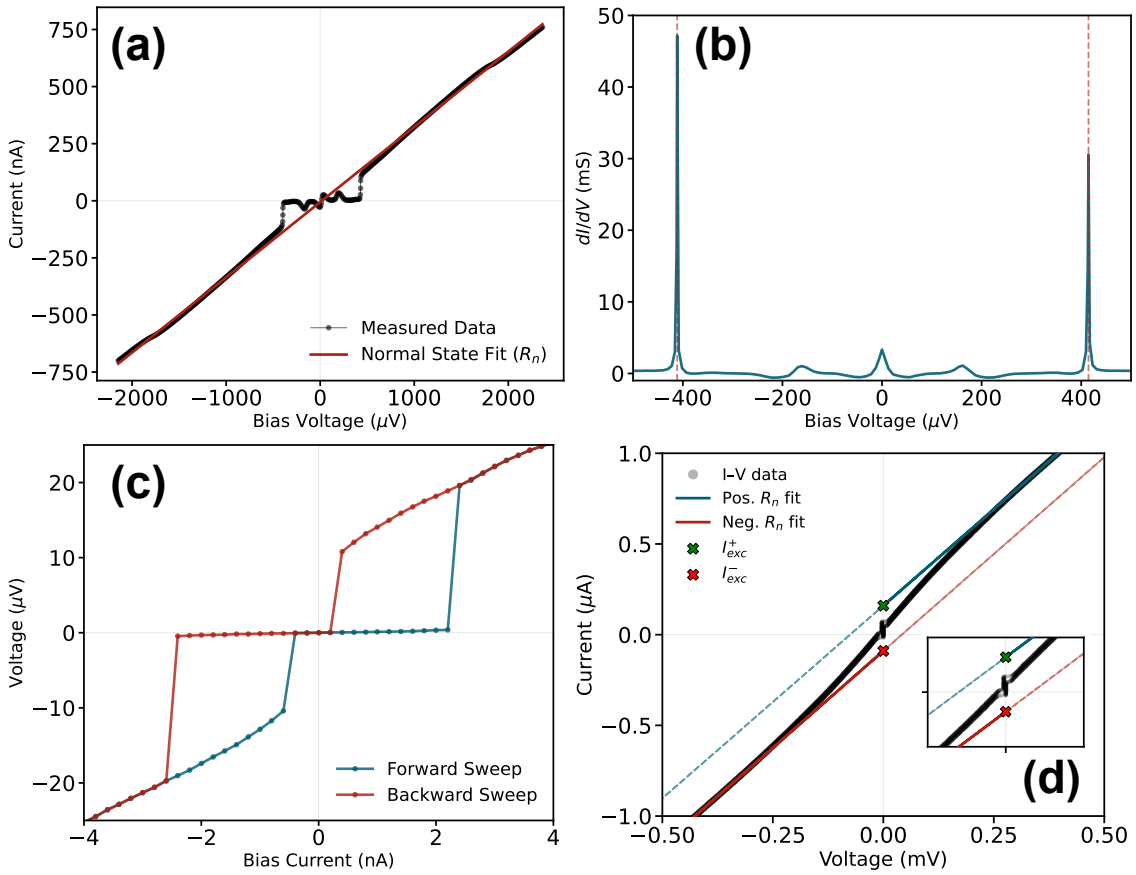

Figure 2.14: Basic transport characterisation of Josephson junctions measured in the devices investigated throughout this thesis. **(a)** Current-voltage (I-V) characteristics of a voltage-biased $\mathrm{Al} - \mathrm{AlO_x} - \mathrm{Al}$ SIS junction from Paper I. The normal-state resistance, R_N, is extracted from the linear slope in the high-bias regime. **(b)** Differential conductance (dI/dV) of the same SIS junction, revealing distinct superconducting coherence peaks at $V = \pm 2\Delta/e \approx \pm 400\,\mu\mathrm{V}$, which define the quasiparticle gap edge. At larger bias magnitudes, the conductance approaches the normal-state value. **(c)** Hysteretic I-V characteristics of a current-biased $\mathrm{EuS} - \mathrm{Al} - \mathrm{InAs}$ nanowire SNS junction from Paper II. During the forward current sweep, the junction switches into the resistive state at the I_{sw}, while during the reverse sweep it retraps into the superconducting state at the lower I_{ret}. **(d)** Extraction of I_{exc} in a current-biased $\mathrm{Bi_2Se_3}$ SNS junction from Paper III. The excess current is obtained by extrapolating the linear high-bias regime ($|V| \gg \Delta/e$) back to the zero-voltage intercept. The inset shows a magnified view of the low-bias switching region.

resistance R_N from the high-bias ($eV > 2\Delta$) slope, while the differential conductance (dI/dV) probes the quasiparticle DOS. Coherence peaks at $V = \pm 2\Delta/e$ define the superconducting gap, with suppressed sub-gap conductance indicating a high-quality tunnel barrier.

The extracted values of Δ and R_N are related to the critical current of a tunnel junction

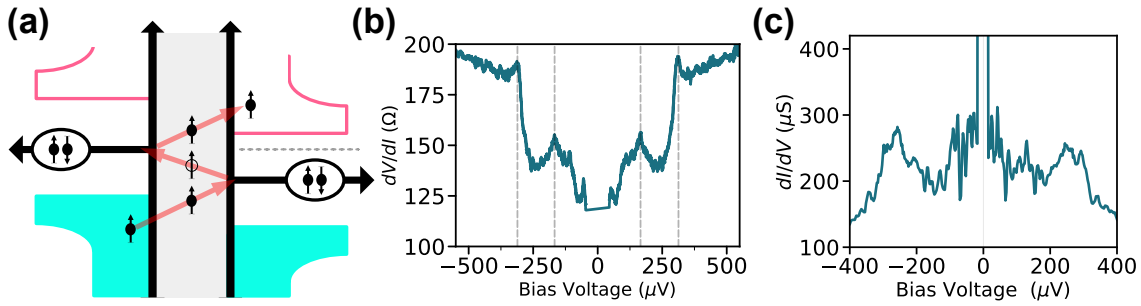

Figure 2.15: MARs in SNS junctions. **(a)** Schematic of MAR: quasiparticles undergo successive Andreev reflections, gaining an energy eV per traversal until reaching the continuum above Δ. **(b)** Differential resistance of a Bi_2Se_3 junction showing MAR features at $eV = 2\Delta/n$. **(c)** Differential conductance of a EuS-Al-InAs NW junction, where dense sub-gap structure indicates strong MAR and high transparency.

through the Ambegaokar-Baratoff relation [131],

$$I_c R_N = \frac{\pi\Delta}{2e} \tanh\left(\frac{\Delta}{2k_B T}\right), \tag{2.44}$$

which reduces to $I_c R_N = \pi\Delta/2e$ in the zero-temperature limit, linking quasiparticle spectroscopy to the equilibrium supercurrent. While this relation is strictly valid in the tunnelling limit of low-transparency SIS junctions, significant deviations can occur in highly transparent SNS and hybrid junctions, where transport is dominated by Andreev processes and the detailed ABS spectrum. These as discussed further in Sec. 2.1.2.

Current-biased measurements, on the other hand, provide direct access to the switching dynamics and non-equilibrium transport properties of Josephson junctions. Figure 2.14(c) shows a typical hysteretic I-V characteristic of a SNS junction: as the current is increased, the junction switches from the superconducting to the resistive state at the switching current (I_{sw}), while upon decreasing the current it retraps at a lower current (I_{ret}). In highly transparent SNS junctions, such hysteresis is often attributed primarily to electronic self-heating and non-equilibrium quasiparticle dynamics rather than capacitive effects, since quasiparticles in the weak link may not thermalise efficiently during the current sweep [3].

A defining feature of SNS junctions is the presence of an excess current (I_{exc}), arising from Andreev reflection at the SN interfaces (Fig. 2.14(d)), similar to the excess current discussed in Sec. 2.1.2. This reflects significant Andreev transport across relatively transparent SN interfaces.

Multiple Andreev Reflection At finite bias voltages below the superconducting gap ($eV < 2\Delta$), quasiparticles can undergo repeated Andreev reflections between superconducting interfaces, giving rise to Multiple Andreev Reflection (MAR) processes and characteristic subharmonic gap structures in the conductance spectrum [85, 132, 133]. As observed in Fig. 2.15(b-c), highly transparent junctions exhibit enhanced MAR processes leading to dense, overlapping sub-gap features, reflecting strong quasiparticle transport mediated by repeated Andreev reflections. Consequently, MAR provides an important

experimental probe of interface transparency and superconducting transport in hybrid junctions, complementary to quantities such as $I_c R_N$ and I_{exc}. A more detailed discussion of MAR and its spectroscopic signatures is presented in Sec. 2.1.2.

2.3.1 Electrodynamics of Josephson Junctions

A practical description of a JJ embedded in a dissipative electrical environment is provided by the resistively and capacitively shunted junction (RCSJ) model [134, 135]. The junction is modeled as an ideal Josephson element in parallel with a resistance R and a capacitance C. The total current through the junction is given by

$$I = I_c \sin\phi + \frac{\hbar}{2eR}\dot{\phi} + C\frac{\hbar}{2e}\ddot{\phi}, \tag{2.45}$$

where ϕ is the superconducting phase difference. This equation is formally equivalent to the motion of a particle in a *tilted washboard potential*,

$$U(\phi) = -E_J \cos\phi - \frac{\hbar I}{2e}\phi. \tag{2.46}$$

This analogy is illustrated in Fig. 2.16(a). The applied current tilts the potential and reduces the barrier separating adjacent minima. For $I < I_c$, the phase is trapped in a local minimum, corresponding to the zero-voltage superconducting state. As the tilt increases, the barrier height decreases and vanishes at $I = I_c$, beyond which the phase enters a running state associated with a finite voltage.

The damping of the phase dynamics is characterised by the McCumber parameter $\beta_c = \frac{2e}{\hbar} I_c R^2 C$. In the presence of thermal fluctuations, the phase particle can escape from a local minimum of the washboard potential even for $I < I_c$, resulting in stochastic phase slips and a finite voltage. In the overdamped limit ($\beta_c \ll 1$), this phase-diffusive regime is quantitatively described by the Ivanchenko-Zilberman (I-Z) model [136].

By treating the phase as a Brownian particle in the potential defined by Eq. (2.45), the time-averaged voltage can be calculated analytically. The resulting IVCs are expressed through modified Bessel functions of complex order, where the degree of rounding is determined by the ratio of the Josephson coupling energy to the thermal energy, $E_J/k_B T$. As shown in Fig. 2.16(b), thermal activation over the barriers leads to a suppression and broadening of the supercurrent peak. At elevated temperatures, the stochastic nature of the phase evolution replaces the sharp zero-voltage branch with a resistive transition, a behaviour characteristic of small-capacitance junctions coupled to a resistive environment [137, 138].

The presence or absence of hysteresis in the IVC is determined by the damping of the phase dynamics within the RCSJ model, quantified by the McCumber parameter β_c.

In the underdamped regime ($\beta_c \gg 1$), the phase exhibits inertial dynamics, leading to hysteretic behaviour characterised by distinct switching (I_{sw}) and retrapping (I_{ret}) currents. In contrast, in the overdamped regime ($\beta_c \ll 1$), strong dissipation suppresses inertial effects, typically resulting in non-hysteretic, single-valued IVC.

In hybrid SNS junctions, however, hysteresis can also arise from non-equilibrium effects such as electronic self-heating in the normal region. In this case, the retrapping current is reduced due to elevated quasiparticle temperature, even when the junction is nominally overdamped [3].

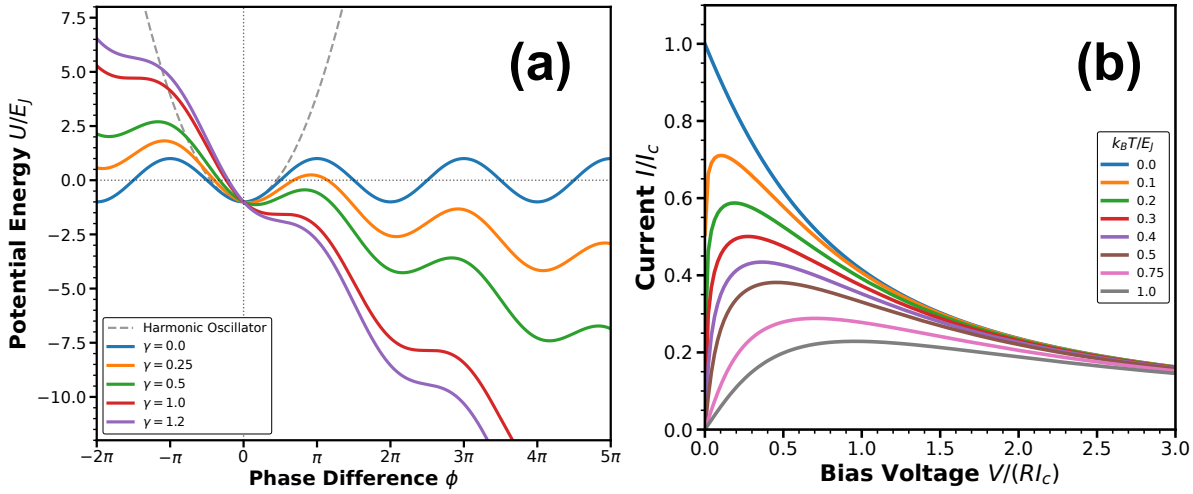

Figure 2.16: Phase dynamics and thermally activated transport in a resistively shunted JJ. (a) Normalised washboard potential $U(\phi)/E_J$ as a function of the superconducting phase difference ϕ for increasing normalised bias current $\gamma = I/I_c$. The applied current tilts the potential, reducing the barrier height between neighboring minima, which vanishes at $\gamma = 1$, marking the transition to the running (finite-voltage) state. **(b)** IVCs described by the Ivanchenko-Zilberman model for different reduced temperatures $t = kT/E_J$. Increasing temperature enhances thermal activation over the potential barriers in (a), resulting in suppression and broadening of the supercurrent peak [136, 138].

Inelastic Cooper-Pair Tunnelling and Environmental Spectroscopy Beyond phase diffusion, additional sub-gap features can arise from inelastic Cooper-pair tunnelling (ICPT). In this process, a Cooper pair tunnels across the junction while exchanging energy with the local electromagnetic environment, in contrast to tunnelling elastically at constant energy [139]. This energy transfer allows the tunnelling pair to irreversibly excite modes within the surrounding circuit, giving rise to distinct resonant features in the DC transport characteristics.

The physical mechanism is illustrated in Fig. 2.17. A tunnelling Cooper pair can emit a photon into an environmental mode (a). Crucially, this inelastic process requires the environment to act as an energy sink, meaning the environmental circuit must be dissipative. Reactive components (imaginary impedance, $\mathrm{Im}(Z)$) only store and return energy over a complete cycle and therefore cannot facilitate the irreversible energy loss required for an inelastic tunnelling event to occur. Consequently, the absorption spectrum of the environment is determined specifically by the frequency-dependent real part of the total impedance, $\mathrm{Re}(Z_{\mathrm{env}}(\omega))$ (b). As shown in (c), resonant peaks appear in the I-V characteristic when the energy supplied by the voltage bias matches a mode in the dissipative environmental spectrum, satisfying

$$2eV = hf_0. \tag{2.47}$$

Within the weak-tunnelling regime, where Cooper-pair tunnelling can be treated perturbatively, the DC current generated by inelastic Cooper-pair tunnelling is proportional

to the dissipative part of the environmental impedance,

$$I_{\mathrm{DC}} = \frac{|I_c^{\mathrm{spec}}|^2}{2V_{\mathrm{DC}}} \mathrm{Re}(Z_{\mathrm{env}}(\omega)) \,, \tag{2.48}$$

where $\omega = 2eV_{\mathrm{DC}}/\hbar$ is the Josephson frequency and $Z_{\mathrm{env}}(\omega)$ is the effective frequency-dependent environmental impedance [73, 140].

For a resonant electromagnetic environment, the dissipative response may be approximated by a Lorentzian resonance of quality factor Q,

$$\mathrm{Re}(Z(\omega)) = \frac{Z_{\mathrm{ext}} Q}{1 + Q^2 \left(\frac{\omega_0}{\omega}\right)^2 \left[1 - \left(\frac{\omega}{\omega_0}\right)^2\right]^2}, \tag{2.49}$$

where ω_0 is the resonance frequency and Z_{ext} characterises the external impedance.

These relations demonstrate that the junction functions as a frequency-tuneable, on-chip spectroscopic probe of the dissipation in its electromagnetic environment [141].

While Eq. (2.48) provides a convenient and intuitive spectroscopic mapping, it is formally valid in the weak-coupling regime and typically describes single-photon exchange processes [140]. A more general description of inelastic Cooper-pair tunnelling is provided by $P(E)$ theory [139, 142], which describes the probability for a tunnelling Cooper pair to exchange energy with its electromagnetic environment. Within this framework, the environmental mode spectrum is directly reflected in the measured transport characteristics.

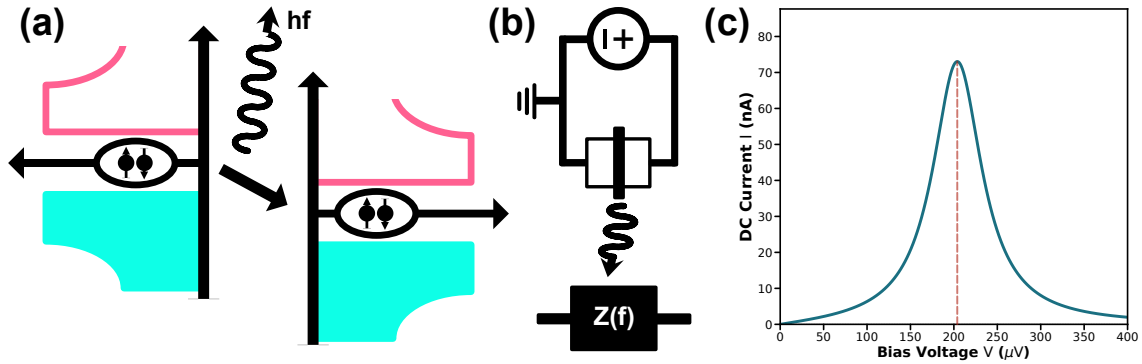

Figure 2.17: Inelastic Cooper-pair tunnelling and environmental coupling. **(a)** Schematic of a Cooper pair tunnelling while emitting a photon of energy hf_0 into the environment. **(b)** Equivalent circuit representation with frequency-dependent impedance $Z(\omega)$. **(c)** Resulting I-V characteristic showing a resonance at $2eV = hf_0$.

Modelling the Electromagnetic Environment To quantitatively describe the spectroscopic response discussed above, the electromagnetic environment surrounding the junction is commonly modeled as an effective resonant circuit characterised by a resonance frequency ω_0 and quality factor Q. Within this framework, resonant features in the transport characteristics originate from energy exchange between the junction and dissipative modes of the surrounding circuit.

In realistic hybrid devices, the effective environmental impedance $\mathrm{Re}(Z_{env}(\omega))$ depends on both geometric and material contributions, including stray capacitances, lead inductances, kinetic inductance, and coupling to external circuitry. The origin and quantitative modeling of these contributions are discussed in the context of the experimental devices in Sec. 4.1.

Kinetic Inductance In nanostructured superconducting circuits, the total inductance L consists of two contributions: the geometric inductance L_g, arising from the magnetic field generated by the current distribution, and the kinetic inductance L_k, arising from the inertia of the Cooper-pair condensate. For ultra-thin films (such as the ones in Paper I) where the thickness t is much smaller than the London penetration depth λ, the kinetic inductance typically dominates the total inductive response. Microscopically, L_k originates from the finite effective mass m^* of the superconducting charge carriers. For a superconducting wire of length l and cross-sectional area $A = wt$, the kinetic inductance can be expressed as

$$L_k = \left(\frac{m^*}{n_s e^{*2}}\right)\frac{l}{wt} = \mu_0\lambda^2\frac{l}{wt}, \tag{2.50}$$

where n_s is the Cooper pair density and $e^* = 2e$ is the Cooper-pair charge [56]. In the Al leads utilised in this work, the effective penetration depth λ deviates significantly from the bulk value $\lambda_L(0)$. Due to the thin-film geometry and the presence of impurities, the system operates in the dirty limit, where the mean free path l_e is much smaller than the bulk BCS coherence length ($l_e \ll \xi_0$). In this regime, the penetration depth is enhanced according to:

$$\lambda_{eff} = \lambda_L(0)\sqrt{\frac{\xi_0}{l_e}}, \tag{2.51}$$

where for aluminium, $\lambda_L(0) \approx 16$ nm and $\xi_0 \approx 1.6$ μm [143]. This enhancement can increase the effective λ by an order of magnitude, making the leads highly inductive. For the complex lead geometries often found in hybrid devices, the total kinetic inductance must be calculated by summing the contributions of individual segments according to their respective geometric ratios:

$$L_k^{tot} = \sum_i \mu_0\lambda_{eff}^2\frac{l_i}{w_i t_i}. \tag{2.52}$$

2.3.2 Interference Phenomena

Phase-coherent transport in hybrid junctions gives rise to interference phenomena that probe both the coherence of electronic motion and the spatial structure of the superconducting phase. The specific form of interference depends on the underlying transport regime and on which phase variable dominates the dynamics.

In diffusive systems ($\ell_e < L < \ell_\phi$), electrons traverse many different scattering trajectories whose quantum phases interfere with one another. This interference produces Universal Conductance Fluctuations (UCF), manifested as aperiodic, sample-specific conductance variations that act as a fingerprint of the disorder landscape. These fluctuations are characterised by a correlation field $B_{cor} \sim \Phi_0/A_{cor}$, where $\Phi_0 = h/e$ is the flux quantum and A_{cor} is the phase-coherent area. B_{cor} represents the field scale required to

shift the relative phase of interfering paths by 2π, thereby generating an uncorrelated conductance value [33, 144, 145].

If the system geometry includes closed loops, phase coherence instead facilitates periodic oscillations in the magnetoconductance. These manifest as the Aharonov-Bohm (AB) and Altshuler-Aronov-Spivak (AAS) effects, with periods h/e and $h/2e$, respectively, the latter originating from interference between time-reversed diffusive paths [33, 145–147].

In the ballistic regime ($\ell_e \gg L$), where scattering is weak and reflections occur primarily at device boundaries, interference is governed by coherent multiple reflections within the junction. Under suitable conditions, this can give rise to FP interference, manifested as periodic oscillations in conductance that reflect the cavity geometry and mode structure of the system. The observation of FP oscillations therefore provides strong evidence for quasi-ballistic, phase-coherent transport.

In superconducting junctions, a parallel magnetic field induces a spatial gradient in the phase difference across the link. The resulting Fraunhofer-like interference pattern in $I_c(B)$ provides a direct measure of the effective junction area and is used to resolve the spatial distribution of the critical current density as detailed below.

In the following sections, we focus first on FP interference as a probe of ballistic transport and transmission properties, and then on Fraunhofer interference as a probe of the effective cross-sectional area of Al junctions.

Fabry-Pérot Interference and Subband Quantisation

In ballistic Josephson junctions, where the elastic mean free path exceeds the junction length ($\ell_e \gg L_N$), the normal region can act as an electronic Fabry-Pérot cavity. Electronic wavefunctions undergo multiple coherent reflections at the cavity interfaces and interfere with one another. When several Fermi wavelengths fit inside the cavity ($\lambda_F < L_N$), constructive interference occurs whenever the accumulated phase satisfies

$$2k_n L_N = 2\pi n, \tag{2.53}$$

where k_n is the longitudinal wave vector and n is an integer (in the simplest cavity approximation) [87, 89, 90, 148]. Experimentally, these resonances manifest as oscillations in conductance as a function of gate voltage and source-drain bias.

A simple way to understand FP interference is to view the system as a particle-in-a-box problem with confinement both along and transverse to the transport direction. The electron wave vector can therefore be decomposed into longitudinal and transverse components,

$$k^2 = k_n^2 + q_n^2, \tag{2.54}$$

where k_n and q_n correspond to the longitudinal and transverse momenta, respectively. The ratio between these components determines the propagation angle of each transport mode,

$$\theta = \tan^{-1}\left(\frac{q_n}{k_n}\right). \tag{2.55}$$

In Dirac materials such as TI nanoribbons, spin-momentum locking suppresses backscattering and allows highly transparent transport channels. As a result, FP interference can

remain visible over comparatively long distances, with transmission resonances enhanced by Klein tunnelling of the Dirac surface states [149, 150].

In TI nanoribbons, the transverse momentum is quantised around the perimeter of the nanoribbon according to

$$q_n = \frac{2\pi}{P}\left(n + \frac{1}{2} - \frac{\Phi}{\Phi_0}\right), \tag{2.56}$$

where $P = 2(W + t)$ is the perimeter of the nanoribbon, Φ is the magnetic flux threading the device, and $\Phi_0 = h/e$ is the magnetic flux quantum [79, 87, 89, 90, 151]. The half-integer shift originates from the π Berry phase associated with spin-momentum locking of the topological surface states. In the high-aspect-ratio limit ($W \gg t$), the perimeter simplifies to $P \approx 2W$, yielding

$$q_n \simeq \frac{\pi}{W}\left(n + \frac{1}{2} - \frac{\Phi}{\Phi_0}\right). \tag{2.57}$$

The subband structure can be manipulated by an axial magnetic flux through the AB effect. At half a flux quantum ($\Phi = \Phi_0/2$), the AB phase compensates the Berry phase, causing the $n = 0$ mode to become gapless ($q_n = 0$) [87].

Interference between multiple reflections leads to an oscillatory transmission probability for each transport mode. For a mode with longitudinal momentum k_n, the transmission as a function of chemical potential $\mu = \epsilon - \epsilon_D$, measured relative to the Dirac point ϵ_D, is given by [148, 152]

$$\tau_n(\mu) = \frac{k_n^2}{k_n^2 \cos^2(k_n L_N) + (\mu/\hbar v_F)^2 \sin^2(k_n L_N)}, \tag{2.58}$$

with

$$k_n = \sqrt{\left(\frac{\mu}{\hbar v_F}\right)^2 - q_n^2}. \tag{2.59}$$

At resonance, the phase accumulation satisfies $k_n L_N = n\pi$, minimising the denominator of Eq. (2.58) and allowing the transmission to approach unity. The corresponding zero-bias conductance can be obtained within the Landauer formalism (Eq. (2.7)) where $G(\mu)$ depends on $\tau(\mu)$, evaluated at the Fermi energy in the zero-temperature limit [33, 153].

In the ideal single-mode limit with linear dispersion, FP resonances are strictly periodic in chemical potential. In realistic 2D devices, however, the oscillations generally become quasi-periodic due to finite transverse confinement, non-uniform gating, and mode-dependent transmission. Tuning the chemical potential via gate voltage therefore produces oscillatory conductance patterns, as shown in Fig. 2.18(b). The oscillation period depends on the cavity dimensions through the longitudinal and transverse quantisation conditions and evolves systematically with the nanoribbon width. At higher chemical potentials, additional faster oscillations associated with transverse subband quantisation become increasingly prominent. In contrast to the smooth longitudinal FP oscillations, these transverse resonances can acquire a strongly non-sinusoidal character, producing sharper conductance features and higher-order harmonics in the corresponding Fourier spectra.

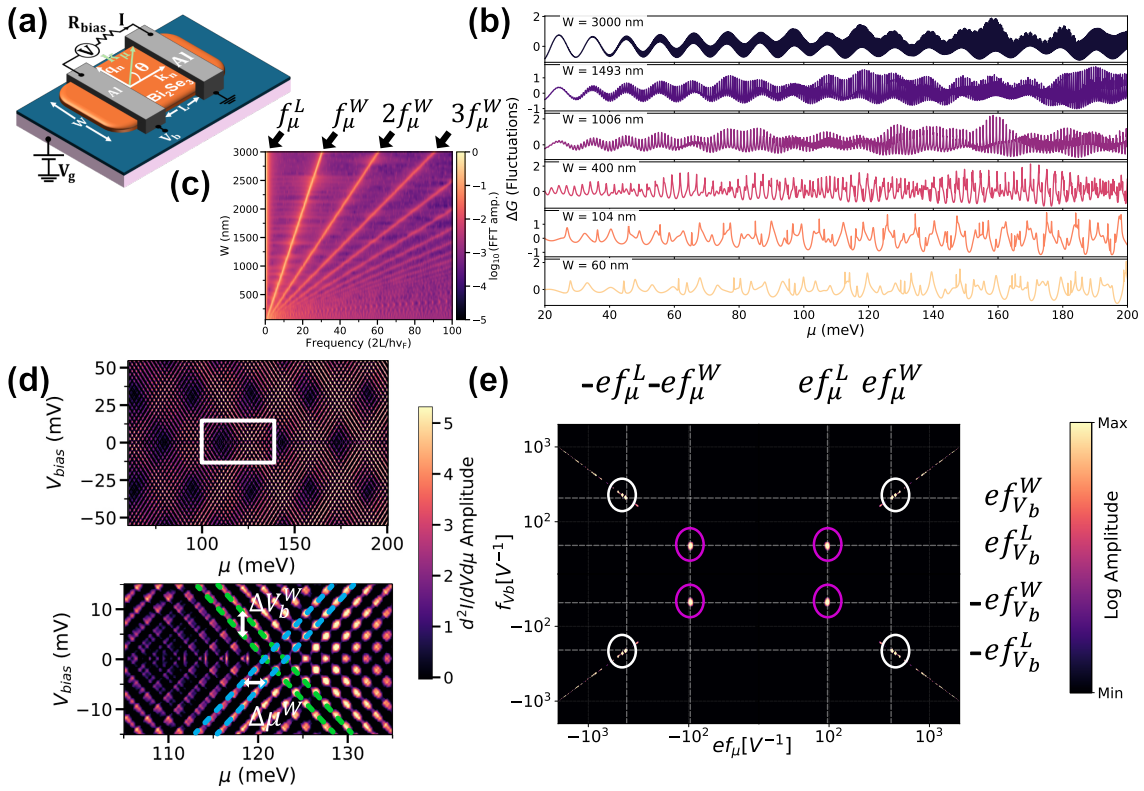

Figure 2.18: Fabry-Pérot interference and transverse subband quantisation in TI nanoribbons [84]. **(a)** Schematic illustration of the electronic cavity and device geometry. **(b)** Numerically calculated conductance versus chemical potential μ for a fixed junction length $L = 100$ nm and varying widths W ranging from 60 nm to 3 μm. Data are presented in vertically stacked panels with linear backgrounds subtracted to isolate quantum fluctuations. **(c)** One-dimensional Fourier transforms of the conductance traces shown in (b), highlighting the width-dependent resonance frequencies. **(d)** Differential conductance maps versus chemical potential μ and bias voltage V_b for a cavity with $L = 100$ nm and $W = 430$ nm. In the full range map (upper panel), the primary longitudinal FP diamonds appear broadened due to real-space beating effects in the underlying conductance curve. The lower panel provides a high-resolution zoom-in of the low-bias regime, where the finer FP diamonds associated with width quantisation are highlighted with green and blue dashed lines, characterised by the energy spacings $\Delta\mu^W$ and $e\Delta V_b^W = 2\Delta\mu^W$. **(e)** Two-dimensional Fourier transform of the FP conductance map shown in (d). The transform reveals coexisting resonance signatures from both the device length and width along both the f_μ and f_{V_b} frequency axes. White dashed crosshairs mark the calculated theoretical positions of the longitudinal (f_μ^L, $f_{V_b}^L$) and transverse (f_μ^W, $f_{V_b}^W$) resonance frequencies, confirming that the correct geometric periodicities are successfully recovered from the modulated cavity profiles.

The spacing of these resonances provides direct access to the cavity dimensions. Longitudinal resonances originate from phase accumulation along the junction length and exhibit a characteristic energy spacing

$$\Delta\mu^L = \frac{hv_F}{2L_N}, \tag{2.60}$$

while transverse subband quantisation produces an additional energy scale

$$\Delta\mu^W = \frac{hv_F}{2W}. \tag{2.61}$$

In finite-bias spectroscopy, these correspond to bias periodicities

$$e\Delta V_b^L = 2\Delta\mu^L, \tag{2.62}$$

and

$$e\Delta V_b^W = 2\Delta\mu^W. \tag{2.63}$$

The underlying geometry and gate-dependent confinement effects are illustrated in Fig. 2.18(a-b), while the corresponding one-dimensional Fourier spectra in Fig. 2.18(c) reveal the systematic emergence of width-dependent transverse modes alongside the primary longitudinal cavity resonances.

To evaluate how these transmission probabilities govern transport away from equilibrium, the total current can be related directly to the energy-dependent transmission through the Landauer formalism,

$$I = \frac{2e}{h}\int_{\epsilon_l}^{\epsilon_r} \tau(\epsilon - \epsilon_D)\, d\epsilon, \tag{2.64}$$

where $\tau(\epsilon)$ is the energy-dependent transmission, ϵ_D denotes the position of the Dirac point, and ϵ_l and ϵ_r are the electrochemical potentials of the left and right contacts, respectively.

At finite source-drain bias, this energy-dependent transmission maps out characteristic diamond-shaped structures in the differential conductance, as shown in Fig. 2.18(d). The corresponding two-dimensional Fourier spectrum presented in Fig. 2.18(e) cleanly isolates the distinct longitudinal and transverse resonance frequencies, confirming the multi-directional nature of the quantum confinement within the mesoscopic cavity.

The visibility of FP interference is ultimately limited by phase coherence. Interference requires the cavity length to remain shorter than the phase coherence length ($L_N < \ell_\phi$), while elevated temperatures and non-uniform gating can reduce the visibility of the oscillations through phase averaging and subband-dependent electrostatic effects.

Fraunhofer Interference in Thin-Film SIS Junctions

While the RCSJ model and spectroscopic probes capture the temporal dynamics of the superconducting phase, magnetotransport measurements provide complementary information about the spatial variation of the critical current density across the junction. In particular, they probe the real-space distribution of the supercurrent density, the effective junction area, and possible inhomogeneities or unconventional transport channels.

In the thin-film limit, where the film thickness is small compared to both the London penetration depth and the Pearl length ($t \ll \lambda_L$, $t \ll \Lambda$ [154]), magnetic screening is weak and the field penetrates the superconducting electrodes nearly uniformly. The resulting screening currents are distributed across the full thickness of the film and change direction when crossing between electrodes. This framework is particularly relevant for ultrathin Al-AlO$_x$-Al junctions (such as in Paper I), where both the coherence length and London penetration depth exceed the film thickness [143, 155].

In this geometry, the magnetic interference pattern provides a direct means of determining the effective flux-threading area of the junction.

We first calculate the Meissner screening currents in the superconductors by solving the Maxwell-London equations in the presence of an external magnetic field [3]

$$\mu_0 \nabla \times (\lambda^2 \mathbf{j}) + \mathbf{B} = 0, \qquad \nabla \times \mathbf{B} = \mu_0 \mathbf{j}. \tag{2.65}$$

where $\mathbf{B}$ is the magnetic induction containing both the externally applied field B_{ext} and the field generated by the supercurrents, μ_0 the vacuum permeability, $\mathbf{j}$ is the supercurrent density and λ is the London penetration depth. $\mathbf{B}$ can be written $\mathbf{B} = \nabla \times \mathbf{A}$ where $\mathbf{A}$ is a vector potential.

The resulting Meissner screening-current distribution obtained from a numerical solution of Eq. (2.65) is shown in Fig. 2.19(a).

Next we calculate the difference between the gauge invariant phase differences across the junction at the left edge $\gamma_1 = \gamma(-w/2)$ and right edge $\gamma_2 = \gamma(+w/2)$ of the junction (see Fig. 2.19(a). From the above calculated Meissner currents and resulting magnetic fields we can readily compute $\Delta\gamma = \gamma_2 - \gamma_1$ making use of the property that the superconducting phase is single valued in the electrodes by choosing an appropriate integration path shown as black line in Fig. 2.19(a)

$$\Delta\gamma = \frac{2\pi}{\phi_0} \oint \mathbf{A} \cdot d\mathbf{l} + \frac{2\pi\mu_0\lambda^2}{\phi_0} \oint \mathbf{j} \cdot d\mathbf{l}. \tag{2.66}$$

Here $\phi_0 = 2 \cdot 10^{-15}$ Vs is the superconducting flux quantum , and the second integral on the right hand side of eq. (2.66) is taken only inside the superconducting electrodes. The path is chosen such that $\mathbf{j} \cdot \partial\mathbf{l}$ is zero everywhere, either $\mathbf{j}$ is zero (horizontal parts of the integration path) or $\mathbf{j}$ is orthogonal to the integration path (diagonal parts of the integration path).

This leaves only the vector potential component

$$\Delta\gamma = \frac{2\pi}{\Phi_0} \oint \mathbf{A} \cdot d\mathbf{l} = \frac{2\pi}{\Phi_0} \iint (\nabla \times \mathbf{A}) \cdot d\mathbf{S} = \frac{2\pi}{\Phi_0} \iint \mathbf{B} \cdot d\mathbf{S} \tag{2.67}$$

By applying Stokes' theorem we obtain a relation the effective area A_{eff} and the difference of the gauge invariant phase differences at the two edges of the junction $\Delta\gamma$,

$$\Delta\gamma = \frac{2\pi B A_{eff}}{\phi_0}. \tag{2.68}$$

with A_{eff} the area enclosed by the thick black lines, which can be approximated by a rectangle with width w and height $t/2$, $A_{eff} \simeq wt/2$ in this geometry.

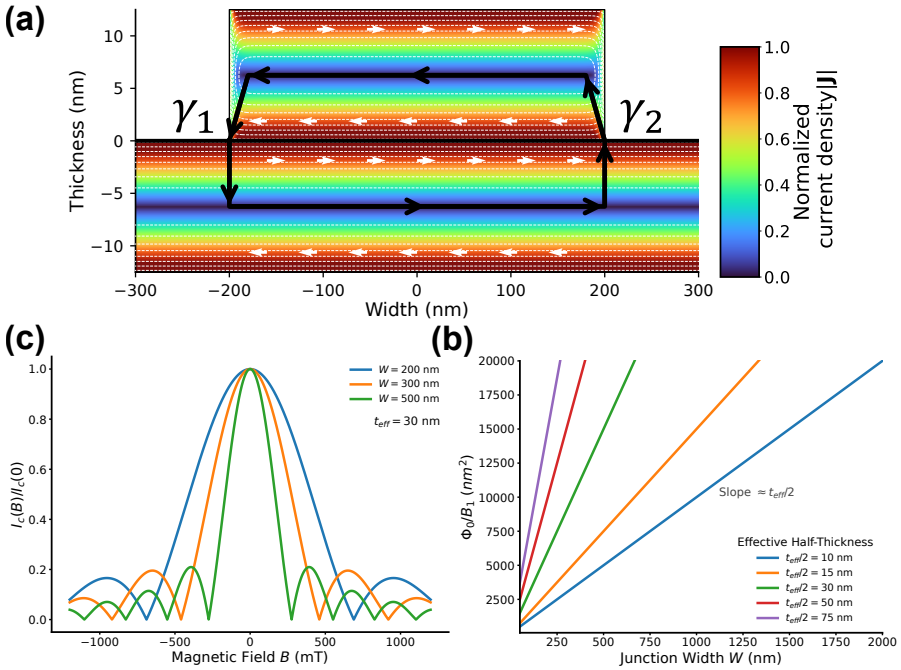

Figure 2.19: Magnetic field response of a planar SIS junction and extraction of the effective thickness. The oxide layer is situated in the middle of the vertical stack. **(a)** Calculated current density distribution in the junction, showing screening currents in the superconducting leads. The magnetic field is applied along the z-direction, with the junction width defined along x and the thickness along y. The dashed contour indicates the integration path used to evaluate the enclosed flux. Because the Meissner screening currents circulate in opposite directions in the two electrodes, the magnetic flux contributions partially cancel. As a result, only approximately half of the total superconducting thickness contributes to the effective flux-threading area. **(b)** Fraunhofer patterns $I_c(B)$ for junctions of different widths w, assuming an effective area $A_{eff} = w \cdot t_{eff}/2$. The periodicity increases with decreasing width, consistent with flux quantisation. **(c)** Extracted effective area $A_{eff} = \Phi_0/B_1$ as a function of junction width. The linear dependence confirms $A_{eff} \propto w$, with the slope corresponding to $t_{eff}/2$.

The minimum current is obtained when $\Delta\gamma = \pi \pmod{2\pi}$. As discussed below, the magnetic field corresponding to the first minimum in the Fraunhofer pattern can be used to extract the effective area.

The magnetic flux threading the junction generates a spatially varying superconducting phase difference across the junction width. For a uniform magnetic field, the local phase varies linearly as

$$\phi(x) = \phi_0 + \frac{2\pi}{\Phi_0} B x \frac{t_{eff}}{2}, \tag{2.69}$$

where t_{eff} is the effective flux-threading thickness extracted from the screening-current geometry.

Assuming a a sinusoidal current-phase relation and uniform critical current density, the

local Josephson current density is

$$j_s(x) = j_c \sin[\phi(x)]. \tag{2.70}$$

The total supercurrent follows from integrating across the junction width,

$$I(B) = \int_{-w/2}^{w/2} j_c \sin[\phi(x)]\, dx, \tag{2.71}$$

yielding the standard Fraunhofer interference pattern

$$I_c(B) = I_c(0) \left| \frac{\sin(\pi\Phi/\Phi_0)}{\pi\Phi/\Phi_0} \right|, \tag{2.72}$$

where the enclosed magnetic flux is

$$\Phi = BA_{eff}. \tag{2.73}$$

The resulting magnetic interference pattern is shown in Fig. 2.19(b) for junctions of different widths. As expected from the relation $\Phi = BA_{eff}$, the oscillation period is set by the condition $\Phi = \Phi_0$, such that the characteristic field scale is inversely proportional to the effective area.

This provides a direct experimental route to extract A_{eff} from the position of the first minimum, $B_1 = \Phi_0/A_{eff}$. As shown in Fig. 2.19(c), the extracted effective area scales linearly with the junction width allowing the effective thickness t_{eff} to be determined from the slope.

Deviations from this ideal behaviour provide direct information about non-uniform current distributions, disorder, and the presence of unconventional transport channels [156].

Kinetic Inductance and Magnetic Evolution

The kinetic inductance is sensitive to pair-breaking mechanisms such as an applied magnetic field, which suppress superconductivity and reduce the critical temperature. In thin films, this effect can be described through the magnetic-field-dependent critical temperature $T_c(B)$ [157]. Because the kinetic inductance scales inversely with the superfluid density, it increases as superconductivity is progressively suppressed. To leading order,

$$L_k(B) \propto \frac{1}{T_c(B)}. \tag{2.74}$$

In thin superconducting films, the magnetic-field dependence of the kinetic inductance reflects the same pair-breaking mechanisms that suppress the critical temperature $T_c(B)$ [157]. The relative change in kinetic inductance can therefore be expressed as

$$\frac{L_k(B) - L_k(0)}{L_k(0)} = -\frac{T_c(B) - T_c(0)}{T_c(0)}. \tag{2.75}$$

The reduction of T_c due to pair breaking is described by the Abrikosov-Gor'kov relation [3]:

$$\ln \frac{T_c(\alpha)}{T_c(0)} = \psi\left(\frac{1}{2}\right) - \psi\left(\frac{1}{2} + \frac{\alpha}{2\pi k_B T_c(\alpha)}\right), \tag{2.76}$$

where $\psi(z)$ is the digamma function.

In the thin-film limit with an applied parallel magnetic field, the depairing parameter is given by

$$\alpha = \frac{1}{6}\frac{De^2B^2t^2}{\hbar}, \tag{2.77}$$

where D is the diffusion constant and t is the film thickness.

Expanding in the weak pair-breaking limit leads to a quadratic dependence of the inductance on magnetic field,

$$\frac{L_k(B) - L_k(0)}{L_k(0)} = \frac{\pi}{24}\frac{De^2B^2t^2}{\hbar k_B T_c(0)} = A_1 B^2, \tag{2.78}$$

reflecting the suppression of superconductivity by pair-breaking effects.

Using the relation $T_c(0) = \Delta(0)/(1.76\,k_B)$ allows us to extract the critical temperature at zero external field. Using this we can extract the diffusion constant D from the measured magnetic-field dependence of the inductance.

2.3.3 Josephson Diode Effect in Hybrid devices

The JDE is defined by a non-reciprocal supercurrent response,

$$I_{c+} \neq |I_{c-}|, \tag{2.79}$$

where the critical current depends on the direction of bias or in terms of symmetry $I(\phi) \neq -I(-\phi)$. The JDE is of fundamental and practical interest as it provides a direct probe of symmetry breaking in superconducting systems and enables non-reciprocal superconducting devices without dissipation. In particular, it offers a sensitive diagnostic of the interplay between SOC, magnetism, and phase-coherent transport. This behaviour imposes strict symmetry constraints on the CPR [34, 35].

The microscopic origin of non-reciprocal superconducting transport in a multiband system with Rashba SOC has been established in Sec. 2.2.2, where the combined breaking of inversion and time-reversal symmetries leads to an asymmetric ABS spectrum. We now discuss how this asymmetry manifests experimentally as a JDE.

TRS enforces antisymmetry of the CPR,

$$I(\phi) = -I(-\phi), \tag{2.80}$$

which guarantees that the positive and negative critical currents are equal in magnitude. Breaking TRS alone can shift the CPR by a finite phase ϕ_0, but does not change the symmetry of its extrema.

IS, on the other hand, relates transport under spatial inversion and enforces equivalence between forward and backward propagation. Breaking IS alone can generate momentum-asymmetric spin-split dispersions. However, if TRS remains preserved, Kramers pairs still enforce reciprocal transport, as illustrated in Fig. 2.6 for the case of Rashba SOC and multimode transport.

Only when both TRS and IS are simultaneously broken is this compensation lifted. In this case, left- and right-moving quasiparticles acquire different phase dispersions, resulting in $E_n(\phi) \neq E_n(-\phi)$ and consequently unequal extrema of the CPR, $I_{c+} \neq |I_{c-}|$.

Typical ways of achieving these are summarised in Table 2.3. Structural asymmetry refers to the absence of IS in the device geometry or electrostatic environment, for example due to asymmetric gating, substrate-induced electric fields, or asymmetric superconductor coverage.

Table 2.3: Minimal symmetry requirements for the Josephson diode effect.

Required Condition	Typical Breaking Mechanism
Broken TRS	B_{ext}, exchange field B_{exc}
Broken IS	Rashba SOC, structural asymmetry

In hybrid superconducting systems, IS breaking can arise from SOC associated with structural asymmetry or orbital effects due to an external magnetic field. In semiconductor NWs such as InAs, this is commonly described in terms of Rashba SOC, which is typically the dominant contribution due to electric fields at the superconductor-semiconductor interface. More generally, multiple spin-orbit components may coexist. In particular, the interplay of Rashba and Dresselhaus SOC can introduce additional anisotropies in the supercurrent response, leading to direction-dependent magnetochiral effects and modifications of the diode efficiency [118].

In the systems considered here, transport is therefore treated in a regime where Rashba SOC provides the leading contribution to IS breaking.

TRS is lifted either by an external Zeeman field or by intrinsic exchange fields (B_{exc}) arising from magnetic proximity, for example in junctions coupled to ferromagnetic insulators such as EuS [29, 61].

The microscopic origin of this symmetry breaking in semiconductor systems is discussed in Sec. 2.2.1, where the interplay of SOC and Zeeman fields leads to momentum- and spin-dependent band asymmetries.

These broken symmetries fundamentally reshape the ABS spectrum, as discussed in Sec. 2.2.2 and illustrated in Fig. 2.10. In particular, while SOC lifts spin degeneracy, the addition of TRS breaking removes the compensation between counter-propagating states, leading to an asymmetric phase dependence of the sub-gap spectrum (Fig. 2.10(d) [111, 112].

Experimental Platforms The JDE has been realised across a wide range of material systems, reflecting multiple microscopic routes to achieving the required symmetry breaking. Representative platforms and their mechanisms are summarised in Table 2.4.

JDE as a Mesoscopic Probe The magnitude and polarity of the diode effect provide a sensitive probe of the underlying transport regime. In particular, the observation of a finite JDE at zero external field indicates indicates the presence of internal symmetry breaking, for example through magnetic proximity effects combined with structural inversion asymmetry.

Importantly, while the coexistence of SOC and broken TRS is also a prerequisite for topological superconductivity, the observation of a JDE alone does not constitute evidence for topological phases or MBS. Rather, it should be interpreted as a sensitive diagnostic of symmetry breaking and phase-coherent transport.

Table 2.4: Representative experimental platforms realising the Josephson diode effect and their underlying symmetry-breaking mechanisms.

Platform	TRS breaking	IS breaking	Mechanism
Rashba NW + B_{ext} [118, 158]	Yes	Yes	SOC + Zeeman
Planar InAs JJ [74, 118, 159]	Yes	Yes	SOC + Zeeman
EuS hybrid junction [29, 61]	Intrinsic	Yes	SOC + Magnetic proximity
Twisted bilayer graphene [160]	Yes	Gate-tuneable	Broken IS in moiré bands
Asymmetric SQUID [119]	Yes	Geometric	Interference effects

EuS is a ferromagnetic insulator used in hybrid NW devices to induce an exchange field (B_{exc}) in the semiconductor, reducing the need for large external magnetic fields that can suppress superconductivity in the Al shell [29, 61]. Bulk EuS exhibits a Curie temperature on the order of several tens of kelvin [161], while thin films typically show reduced values around $T_{Curie} \approx 20$ K due to finite-size effects, strain, and disorder [29, 162].

At the EuS-InAs interface, magnetic proximity effects induce an effective exchange field in the semiconductor, resulting in a spin splitting of the electronic states. The magnitude of this induced exchange field can be substantial, allowing access to regimes that would otherwise require large externally applied magnetic fields [29, 61].

EuS thin films typically exhibit soft magnetic behaviour with relatively low coercive fields, and domain formation and pinning, particularly in confined geometries, may influence transport through spatial variations in the induced exchange field.

2.4 Summary and Scope of This Thesis

2.4.1 Overview of Platforms and Research Goals

While topological superconductivity and MBS offer a promising route toward fault-tolerant quantum computing, naturally occurring realisations remain rare. This motivates the development of engineered hybrid platforms designed to realise these phases.

This thesis investigates such systems using mesoscopic JJs, probing unconventional Josephson effects and the underlying ABS spectrum to understand the symmetry-breaking mechanisms associated with engineered topological superconductivity.

Since Majorana physics requires the coexistence of superconductivity, SOC, and broken time-reversal symmetry, often under elevated magnetic fields, this work combines the development of high-field-compatible on-chip spectrometers with the fabrication of semiconductor and TI heterostructures supporting quasi-ballistic transport.

More broadly, the work addresses two central challenges: enabling spectroscopy under extreme conditions and disentangling intrinsic symmetry breaking from extrinsic mesoscopic effects.

2.4.2 Connection to the Results Presented

The experimental results of this thesis are structured around three distinct material platforms, each addressing a critical component in the pursuit of engineered topological superconductivity:

Magnetotransport in Ultra-Thin Josephson Junctions (Sec. 4.1) To access the high magnetic fields required for topological phase transitions, the superconducting electrodes used to probe these systems must be exceptionally robust. We investigate ultra-thin Al-AlO_x-Al JJs that minimise orbital depairing. We demonstrate that these devices remain superconducting and maintain their spectroscopic functionality via ICPT in in-plane magnetic fields exceeding 1 T. This establishes them as a vital on-chip tool for probing ABS in hybrid quantum devices under strong magnetic fields.

Non-Reciprocal Transport in Ferromagnetic Hybrid Nanowires (Sec. 4.2) A core requirement for engineered topological superconductivity is the precise control of symmetry breaking. Using a highly tuneable platform consisting of InAs NWs with epitaxial Al and the ferromagnetic insulator EuS, we investigate the JDE. By systematically varying the magnitude and orientation of external magnetic fields, we identify distinct regimes of non-reciprocal transport. These results highlight the complex interplay between SOC, applied fields, and proximity-induced exchange fields in breaking time-reversal and inversion symmetries.

Crossover of Transport Regimes in Topological Insulators (Sec. 4.3) Finally, the realisation of robust quantum states relies critically on the nature of electronic transport and the preservation of phase coherence in the underlying channels. We investigate quantum transport in hybrid devices based on Bi_2Se_3 NRs by performing a systematic study of junctions with varying geometry.

From normal-state and Josephson transport measurements, we identify a crossover from a quasi-ballistic regime at short junction lengths to a more diffusive regime in longer devices. In particular, the observed length dependence of transport quantities deviates from the scaling expected for purely diffusive systems, indicating the presence of ballistic transport modes in the topological surface states of Bi_2Se_3

In the quasi-ballistic regime, additional signatures consistent with FP interference of surface states are observed in narrow devices.

Together, these measurements provide insight into the geometry-dependent transport regimes in TI nanoribbons and highlight differences between quasi-ballistic surface-state transport and more diffusive bulk transport. In particular, the observation of FP interference is consistent with coherent transport in the surface states, while the overall length dependence is consistent with an increasing contribution from diffusive bulk transport in longer devices. These results help provide a framework for interpreting transport measurements in hybrid TI-superconductor structures.

Taken together, these three platforms provide complementary insight into high-field superconducting spectroscopy, symmetry-breaking mechanisms, and phase-coherent transport. This combined approach establishes both the experimental tools and the physical understanding required for future studies of sub-gap states and engineered topological superconductivity.

3 Experimental Methods

This chapter outlines the experimental foundations required to investigate the hybrid superconducting phenomena presented in this thesis. The realisation of topological superconductivity and non-reciprocal effects hinges on the integration of materials, ranging from thin-film metallic superconductors to ferromagnetic insulators and TIs. Here, we detail the multi-stage fabrication protocols optimised for these disparate platforms and describe the cryogenic measurement infrastructure. Particular emphasis is placed on the electromagnetic environment and filtering techniques necessary to perform phase-coherent spectroscopy in the presence of strong magnetic fields.

3.1 Nanofabrication Methods of Hybrid Devices

All devices were fabricated according to detailed recipes outlined in Appendix A. Depending on the specific device architecture, substrates consisted either of insulating intrinsic silicon, highly doped silicon wafers with a thermally grown SiO_2 insulating layer, or sapphire wafers which in this work were used for future radio-frequency (RF) applications discussed in the outlook (Chapter 5).

For hybrid devices requiring semiconductor NWs or TI NRs (such as the InAs/EuS/Al and Bi_2Se_3 platforms), the NW and NRs were transferred from their growth substrate to the target device chip using a custom nanomanipulator with six degrees of freedom. This technique enabled the deterministic placement and precise angular alignment of individual NWs with spatial accuracy on the order of a few micrometres.

3.1.1 Material-Specific Protocols

Ultra-Thin Al-AlO_x-Al Junctions for Spectroscopy The Josephson tunnel junctions were fabricated using a double-angle evaporation process on Si/SiO_2 substrates. Standard electron-beam lithography was used to define nanoscale openings in a bilayer resist stack, enabling the shadow evaporation of aluminium films at controlled angles.

In the first evaporation step, a thin aluminium base electrode was deposited with a thickness of approximately 10–15 nm. Following this, the samples were exposed to an oxygen environment at a controlled pressure and duration to form a thin AlO_x tunnel barrier. In the second evaporation step, a counter-electrode was deposited at an angle perpendicular to the first evaporation [163], with the thickness chosen to ensure that the total junction stack height remained below 30 nm. The fabrication details of these junctions can be seen in Appendix A.

This fabrication approach allowed for the precise definition of lateral junction dimensions between 80 nm and 900 nm while maintaining reproducibility across multiple devices. The resulting structures combine a thin-electrode geometry which significantly

enhances magnetic-field resilience with a well-controlled oxide barrier, ensuring the formation of high-quality Josephson tunnel junctions. The double-angle evaporation technique also enables straightforward integration with on-chip circuit elements, such as coplanar waveguides or LC resonators, which are utilised for the spectroscopy measurements. The complete, step-by-step recipe is detailed in Appendix A.

Hybrid Nanowire Josephson Devices The fabrication of hybrid NW devices relied on InAs core NWs featuring an epitaxial EuS/Al shell [69, 162]. Following deterministic deposition via the nanomanipulator, the devices were processed in two primary variations depending on the measurement modality:

DC Devices A PMMA/MMA resist mask was defined by EBL, after which the exposed epitaxial Al shell was selectively removed using an MF-319 wet etch to define the weak link. In a second lithography step, the contact electrodes were patterned. Prior to metal deposition, the sample was loaded into an evaporation chamber equipped with an *in-situ* ion milling source. A brief argon ion milling step was performed to strip native oxides from the NW facets, followed immediately by the electron-beam evaporation of a Ti/Al contact stack. The devices were completed by a standard lift-off process. Full fabrication details are provided in Appendix A.

RF Resonator Devices For devices intended for RF spectroscopy, high-kinetic-inductance resonators were patterned prior to NW placement. Sapphire wafers were sputter-coated with niobium titanium nitride (NbTiN) in a near-UHV system. The resonator structures were defined via EBL using a negative ma-N2403 resist mask, supplemented with an ESPACER conductive layer to mitigate substrate charging on the insulating sapphire. Following development, the NbTiN was etched using an Ar/Cl_2 inductively coupled plasma (ICP). The remaining resist was then stripped using a dedicated mr-REM700 remover followed by sonication in organic solvents, replacing the previously used HF-based stripping method. After dicing the wafer, the InAs/EuS/Al NWs were deposited and aligned precisely with the pre-patterned resonators. The subsequent junction definition and Ohmic contact formation followed the same procedure as the DC devices. The full process flow is documented in Appendix A.

Topological Insulator Nanoribbon Devices The Bi_2Se_3 NRs were grown using physical vapor deposition [80, 164]. These NRs typically exhibit two-dimensional carrier densities on the order of 10^{13} cm^{-2}, indicating that both topological surface states and bulk states contribute to electrical transport [86].

The NRs were transferred onto Si/SiO_2 substrates pre-patterned with alignment marks, utilising a dry flip-chip technique or by nanomanipulator. The backside of the substrates was coated with a Ti/Au layer to serve as a global back-gate. The superconducting electrodes were defined by EBL, followed by the electron-beam evaporation of a Pt(3 nm)/Al(80–120 nm) bilayer. Crucially, before metal evaporation, the native oxide residing on the Bi_2Se_3 NRs was removed *in-situ* via Ar^+ ion milling to ensure highly transparent contacts [80, 165]. The detailed lithography and milling parameters are listed in Appendix A.

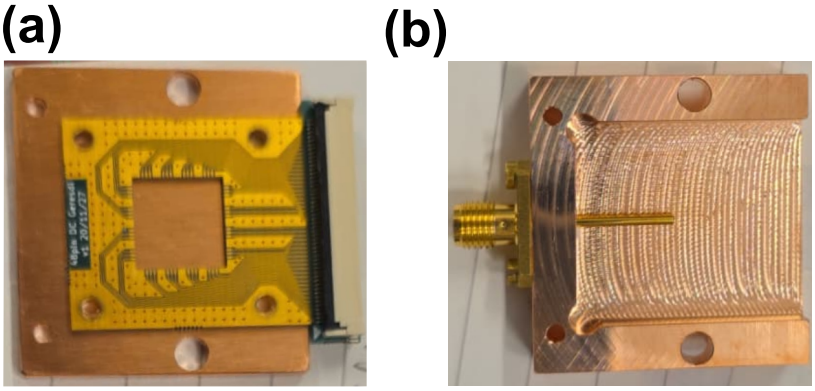

Figure 3.1: **(a)** DC sample holder with 48 line PCB. **(b)** Copper box cover for DC sample holder with a simple antenna.

3.2 Experimental Setup and Measurement Techniques

The low-temperature measurements discussed in this thesis were carried out either in a *Bluefors* dilution refrigerator with a base temperature of approximately 20 mK (Sec. 4.1, Sec. 4.2, i.e. Papers I and II) or in an *Oxford Instruments* cryostat with with comparable base temperature, filtering and magnetic-field capability (one direction). (Sec. 4.3 or Paper III).

The bottom-loading Bluefors cryostat, together with its main components, is shown in Fig. 3.4. These include a copper powder filter (a), a sample-holding probe with sample and filter PCB (b), the cryostat itself (c-d), and a vector magnet (e). Prior to the installation of the copper powder filter and the probe filter, the results pertaining to ultra-thin Al Josephson junctions (Sec. 4.1 and Paper I) were obtained. To improve thermalisation and electromagnetic isolation at the sample, these two filters were subsequently added.

The following sections detail the signal chain, which is routed via a switch matrix box (Fig. 3.2). In its current configuration, the signal line includes multiple stages of filtering. These are described in Fig. 3.3. While this description is based on the Bluefors setup, which was primarily used in this thesis, the Oxford setup is qualitatively similar, with the exception of the bottom-loading mechanism.

3.2.1 Room-Temperature Electronics and Isolation

To eliminate noise injection from the measurement computer and the power grid, the room-temperature instrumentation utilises several layers of filters (see Fig. 3.3(b-c). Excitation voltages and currents are generated by an Isolated Voltage and Voltage Interface (IVVI) rack (Fig. 3.2(b)). Moreover, modules include amplification of signals for both input and output. For details concerning the IVVI rack see Ref. [166]. The IVVI system is powered by internal battery modules, circumventing 50/60 Hz mains ripple and switching noise. To ensure pristine power delivery, these batteries are charged via internal gyrator circuits, which act as active inductive filters to prevent charging noise from reaching the

Figure 3.2: **(a)** Photograph of the matrix module managing the 48 separate DC channels. Each channel features a dedicated switch to toggle the line between a closed circuit, an open circuit, and the measurement ground. **(b)** Photograph of the isolated voltage source (IVVI) rack with several input and output modules. The far-left module contains isolated input ports, while the far-right shows the bias DAC setup connected via an orange optical fibre cable to the measurement computer. The summing module allows individual DACs to be routed internally to dedicated slots for integrated control.

supply rails. Furthermore, the control logic for the digital-to-analog converters is transmitted via an optical fibre, providing complete galvanic decoupling between the noisy digital ground of the measurement computer and the sensitive analog experiment.

Signals from the IVVI rack are routed to the cryostat via a matrix module (Fig. 3.2(a)), which serves as a reconfigurable telephone-style switchboard for the 48 DC lines. This module allows individual lines to be quickly grounded, opened, or connected to specific instruments. Internally, each DC line within the matrix is conditioned by a π-filter and an EMI suppression ferrite bead to attenuate high-frequency interference before it even enters the cryogenic environment. The matrix module is tied to a dedicated low-noise instrument ground, while the cryostat itself is maintained in a floating configuration to prevent large-scale ground loops. Only the primary data acquisition instruments, such as the *Keithley* multimeters and the Zürich Instruments lock-in amplifier are connected to mains power.

3.2.2 Cryogenic Transmission and Low-Temperature Filtering

Signals enter the cryostat head via *Fischer* connectors and propagate down to the mixing chamber (MXC) stage. The cryogenic transmission lines are made of twisted pairs of low ohmic copper wires from room temperature down to the 4K stage and Niobium-

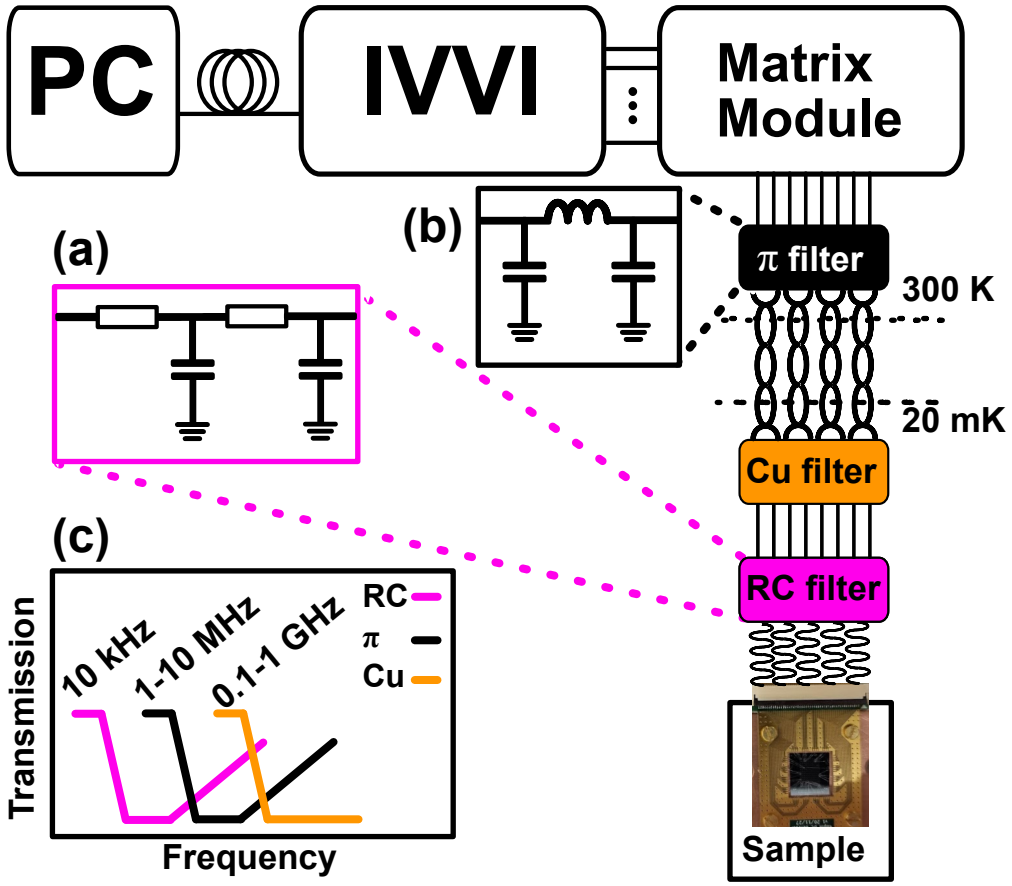

Figure 3.3: Overview of the measurement line filtering within the cryostat [167]. **(a)** Schematic of the RC filter circuit (pink box), which has a roll-off frequency of approximately 10 kHz. This filter is located on a printed circuit board (PCB) inside the measurement probe (see Fig. 3.4(b). Each line of the filter connects to the sample PCB via a meandered trace. **(b)** Schematic of the π-filter circuit (black box), which connects the lines at the Matrix module to the Fischer cable routed to the top of the cryostat. Signal attenuation for this filter begins in the low MHz range. **(c)** Combined frequency attenuation profile of the measurement lines. The RC filter provides the lowest cut-off frequency (tens of kHz), followed by the π-filter which attenuates noise in the MHz regime, and finally the copper powder filter, which suppresses high-frequency noise from 100 MHz up to the GHz range.

Titanium (NbTi) superconducting wire below the 4K stage. NbTi is chosen for its zero DC electrical resistance and extremely low thermal conductivity, which minimises the parasitic heat load on the coldest stages of the fridge. The lines are configured as twisted pairs to suppress inductive pickup and improve common-mode noise rejection.

At the MXC stage, the lines undergo filtering to improve thermalisation toward the 20 mK base temperature (Fig. 3.4(a-b)). The signals first pass through a large copper enclosure containing a printed circuit board (PCB) with meandered traces encased in a copper-powder epoxy. This ”lossy” filter acts as a distributed attenuator, absorbing gigahertz-range radiation through eddy current dissipation in the metallic powder.

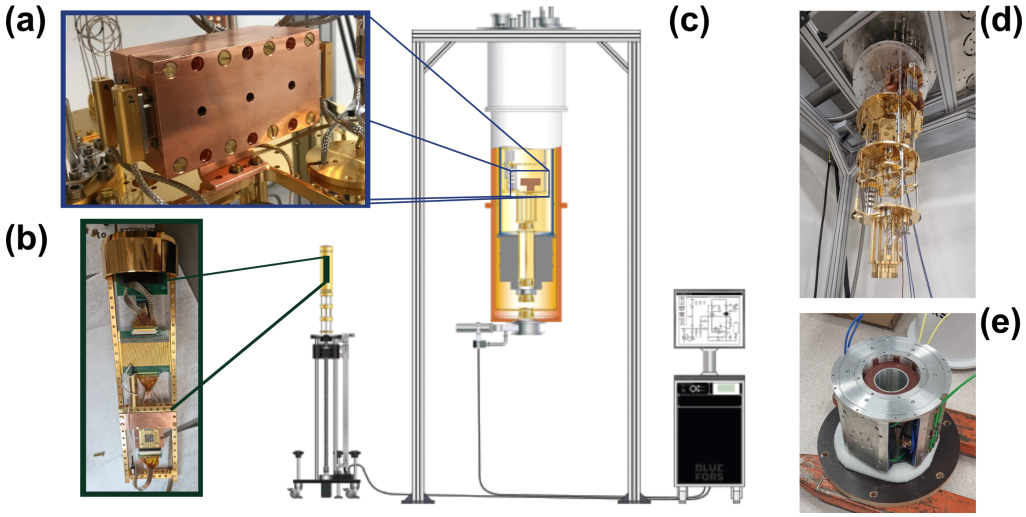

Figure 3.4: Experimental setup used for low-temperature transport measurements. (a) Copper powder filter providing broadband attenuation of high-frequency noise. (b) Measurement probe including RC filters, meander-line filtering stages, and the sample holder. (c) Schematic of the dilution refrigerator equipped with a fast sample exchange system and control unit. (d) Photograph of the dilution refrigerator insert without radiation shields, showing the different temperature stages, 50K at the top and then in descending order, 4K, Still (1K), Cold Plate (100 mK) and MXC at 20 mK. (e) Vector magnet which mounts at the 4 K stage, enabling the application of magnetic fields with arbitrary orientation.

Downstream of the copper powder, the lines connect to a secondary filter PCB containing meandered thermalisation traces and a second-order passive RC low-pass filter ($R_1 = R_2 = 500\,\Omega$, $C_1 = C_2 = 3\,\mathrm{nF}$). This RC stage provides a steep $-40\,\mathrm{dB/decade}$ roll-off with a cutoff frequency near 40 kHz, effectively stripping away residual kilohertz-to-megahertz noise before the signals finally reach the 48-line sample PCB.

3.2.3 Magnetotransport and Lock-in Techniques

The sample is mounted such that its substrate plane lies in the yz-plane of the $(1, 1, 9)$ T vector magnet (Fig. 3.4(e)). This allows specific junction axes to be aligned parallel or perpendicular to the external magnetic field. Magnetotransport measurements were executed by systematically stepping the magnetic field magnitude or angle; at each step, the bias was swept from negative to positive values and back to capture any hysteretic behaviour in the complete current-voltage characteristic (IVC).

Transport measurements utilised both voltage-biased and current-biased configurations, primarily employing a combined DC and lock-in technique (illustrated in Fig. 3.5). For a typical current-bias measurement, a DC current was applied to the device via an isolated IVVI voltage source placed in series with a large biasing resistor.

To simultaneously acquire the differential resistance ($\mathrm{d}V/\mathrm{d}I$), a small AC excitation from the lock-in amplifier was superimposed onto the DC signal. To avoid artificial smearing of fine spectral features, the AC excitation was strictly limited to an RMS

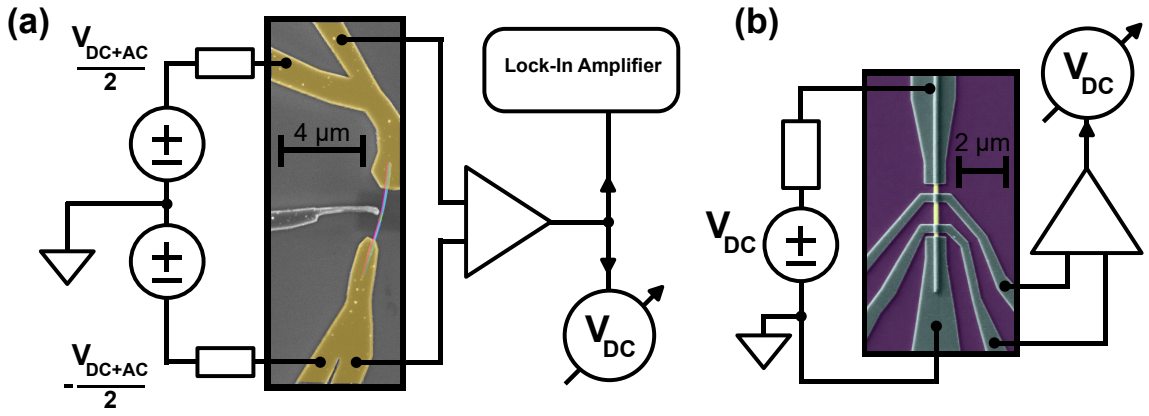

Figure 3.5: Schematic of the DC current-bias measurement setups. **(a):** Schematic of the lock-in and DC current-bias setup used in Paper II, where a DC current bias is combined with a small AC excitation from a lock-in amplifier and injected into the device. The resulting voltage across the device is measured using a voltmeter referenced to ground. The voltage signal is recorded in DC and simultaneously fed to the lock-in amplifier input to measure the differential resistance $\mathrm{d}V/\mathrm{d}I$. **(b):** Schematic of the DC current-bias setup used in Paper III. The current is biased asymmetrically, with the source and one side of the device connected to ground. The resulting voltage across the device is measured using a voltmeter referenced to ground, and the voltage signal is recorded in DC.

amplitude of approximately 1% of the maximum DC bias. Furthermore, the AC frequency (e.g. 377 Hz) was chosen to avoid harmonics of the 50 Hz power-line frequency. The resulting voltage drop across the device was monitored by a ground-referenced voltmeter to capture the DC IVC, while the AC response was simultaneously demodulated by the lock-in amplifier.

The fabrication and measurement techniques described in this chapter provide the tools necessary to probe the limits of superconducting coherence. By combining deterministic nanomanipulation with high-frequency environmental engineering, we have developed a platform capable of high-resolution spectroscopy under extreme magnetic fields.

In the following chapters, we apply these methods to investigate distinct regimes of mesoscopic superconductivity. We begin in section 4.1 by utilising ultra-thin Al-AlO_x-Al junctions to probe the local electromagnetic environment and probe the robustness of the superconducting gap up to the Tesla regime. This is followed by the subsequent investigations into the Josephson diode effect in ferromagnetic hybrid NWs (Sec. 4.2) and the crossover between ballistic and diffusive transport in topological NRs (Sec. 4.3).

4 Results

This chapter presents the primary experimental results of this thesis, exploring the engineering of superconducting transport regimes, high-field resilience, and broken symmetries in low-dimensional hybrid architectures.

We begin in Sec. 4.1 by investigating ultrathin Al-AlO_x-Al tunnel junctions under strong in-plane magnetic fields, using inelastic Cooper-pair tunnelling to extract the local lumped-element RLC environment and validate their functionality as robust high-field spectrometers. We then transition to engineering broken symmetries in Sec. 4.2, exploring the Josephson diode effect and magnetic anisotropy in hybrid InAs-EuS-Al nanowires where proximity-induced exchange fields and spin-orbit coupling drive non-reciprocal supercurrents. Finally, in Sec. 4.3, we examine the transport medium itself by analysing the crossover between diffusive bulk and quasi-ballistic surface transport in Bi_2Se_3 topological insulator nanoribbons. In this final study, we utilise normal-state Fabry-Pérot interferometry and superconducting Josephson transport as complementary probes to map these conduction regimes.

4.1 Magnetotransport in Ultra-Thin Josephson Junctions

Josephson tunnel junctions are central components in superconducting quantum devices, serving both as non-linear circuit elements [168] and as spectroscopic probes of microwave photons [138, 169]. For many emerging applications, particularly in hybrid superconductor-semiconductor systems, it is essential that these junctions remain operational in strong in-plane magnetic fields. Such fields are required to induce Zeeman splitting and access regimes relevant for topological superconductivity as discussed in Sec. 2.2.2.

Conventional aluminium-based junctions, while offering low dissipation and established fabrication protocols, are typically limited to sub-tesla magnetic fields due to orbital depairing and suppression of the critical current [63, 170]. A key strategy to enhance field resilience is to reduce the thickness of the superconducting electrodes, thereby minimising orbital effects.

In this section, we investigate ultrathin Al-AlO_x-Al Josephson junctions with total stack thickness below 30 nm and lateral dimensions ranging from 80 nm to 900 nm. Through low-temperature transport measurements, we examine their current-voltage characteristics, magnetic-field response, and spectroscopic functionality via inelastic Cooper pair tunnelling (ICPT). These measurements demonstrate that such junctions remain robust in magnetic fields exceeding 1 T, establishing them as a versatile platform for high-field superconducting spectroscopy.

The ultrathin Al-AlO_x-Al Josephson junctions were fabricated using a Manhattan-style geometry [62], as detailed in Sec. 3.1.1. In this approach, the junction area is defined by the overlap of two orthogonal aluminium arms, such that the lateral arm width directly sets the junction size.

4.1.1 Device Geometry and Measurement Concept

A representative device and measurement configuration are shown in Fig. 4.1(a). The junction is embedded in a four-terminal voltage-biased measurement circuit, where the surrounding circuitry is represented by an effective electromagnetic environment. This environment plays a central role in the spectroscopic response of the device.

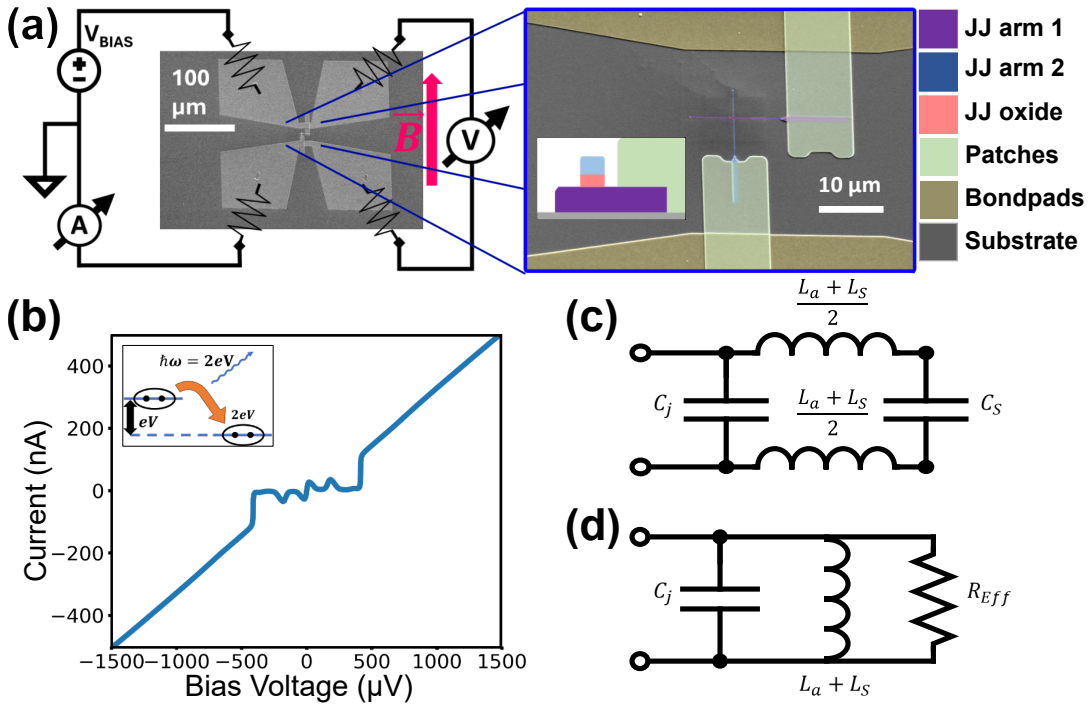

Figure 4.1: **(a)** Scanning electron micrograph of the device and measurement circuit. External circuitry is represented by effective impedances connected to the bond pads. Inset: high-magnification cross-section and false-colour material layers. **(b)** Representative current-voltage characteristic at $T = 25$ mK. Quasiparticle onset is visible at $V \approx 2\Delta/e$. Inset: schematic illustration of the ICPT process. **(c)** Full equivalent circuit of the electromagnetic environment including external bonding pad parasitics. **(d)** Simplified local RLC model used for the spectroscopic analysis. At high frequencies, the pad capacitance acts as an effective short, isolating the junction and its local environment (described by Eq. (4.4)).

A typical current-voltage characteristic measured at $T = 25$ mK is shown in Fig. 4.1(b). Several key features can be identified. At high bias, a sharp onset of current occurs at $V \approx 2\Delta/e \approx 400$ μV, corresponding to quasiparticle tunnelling across the superconducting gap. Above this threshold, the slope of the curve defines the normal-state resistance $R_n \approx 3$ kΩ.

At low bias, a broadened supercurrent peak is observed around zero voltage. The suppression of this peak relative to the Ambegaokar-Baratoff prediction ($I_c \simeq 116.6$ nA for the 360 nm junction in Fig. 4.1(b)) indicates the presence of phase diffusion driven by noise from the electromagnetic environment [171, 172]. In addition, a pronounced subgap resonance appears at $V \approx 200$ μV, arising from inelastic Cooper-pair tunnelling (ICPT) (which was outlined in Sec. 2.3.1 and will be discussed in more detail further down) [134, 135].

To model the ICPT response, we consider the frequency-dependent impedance $Z(\omega)$ seen by the junction. Although the full experimental environment includes complex external circuitry (Fig. 4.1(c)), the dominant high-frequency contributions arise from the local metallic structures surrounding the junction, illustrated in Fig. 4.2(a).

To estimate the relevant circuit elements contributing to the electromagnetic environment shown in Fig. 4.1(c), we consider the metal structures surrounding the junction illustrated in Fig. 4.2(a). There are two distinct structures in the device, the ultra-thin arms and the thick bondpads and patches. These differ a order of magnitude in thickness and the vast area is covered by the bondpads. Thus we will consider these two constituents when we construct the model circuit for our device. Since the arms whose dimensions are labelled in Fig. 4.2(d) are much smaller and also very thin, we approximate their geometric capacitance and geometric inductance as negligible compared to the kinetic inductance. This inductance is something that will be a dynamic property and thus we treat it later. The bond pads, however, are geometrically non-negligible and their inductive and capacitive contributions must be evaluated using the geometries shown in Fig. 4.2(b-e).

We first estimate the stray inductance of the bond pads using the microstrip geometry shown in Fig. 4.2(e) [174]. The inductance is approximated by

$$L = \frac{60\,l}{c_0} \ln\left(\frac{8h}{w} + \frac{w}{4h}\right), \tag{4.1}$$

where $l = 300$ μm is the length of the bondpad, $w = 300$ μm is the width, $h = 380$ μm is the thickness of the substrate. Using these parameters, we estimate the bondpad inductance to be approximately $L_S \approx 140$ pH.

We next estimate the capacitance of the bond pads by considering both the microstrip capacitance to ground illustrated in Fig. 4.2(c,e) and the coplanar capacitance between adjacent bond pads shown schematically in Fig. 4.2(b) [175]. The microstrip capacitance is given by

$$C_{\text{microstrip}} = \frac{\varepsilon_r\, l}{60\, c_0 \,\ln\left(\frac{8h}{w} + \frac{w}{4h}\right)}, \tag{4.2}$$

where $\varepsilon_r = 12$ is the relative permittivity of intrinsic silicon [173], $l = 150$ μm is the bondpad length, $w = 150$ μm is its width, $h = 380$ μm is the silicon substrate thickness, and $c_0 = 3 \times 10^8$ m/s is the speed of light in vacuum. Using these values, we calculate the microstrip capacitance to be approximately 30 fF.

The coplanar capacitance, which accounts for the coupling between adjacent bondpads, is estimated using

$$C_{\text{coplanar}} = \frac{\varepsilon_r\, l}{377\pi c_0} \ln\left(-\frac{2}{\sqrt[4]{1-\frac{s^2}{(s+2w)^2}}-1}\left(1+\sqrt[4]{1-\frac{s^2}{(s+2w)^2}}\right)\right), \tag{4.3}$$

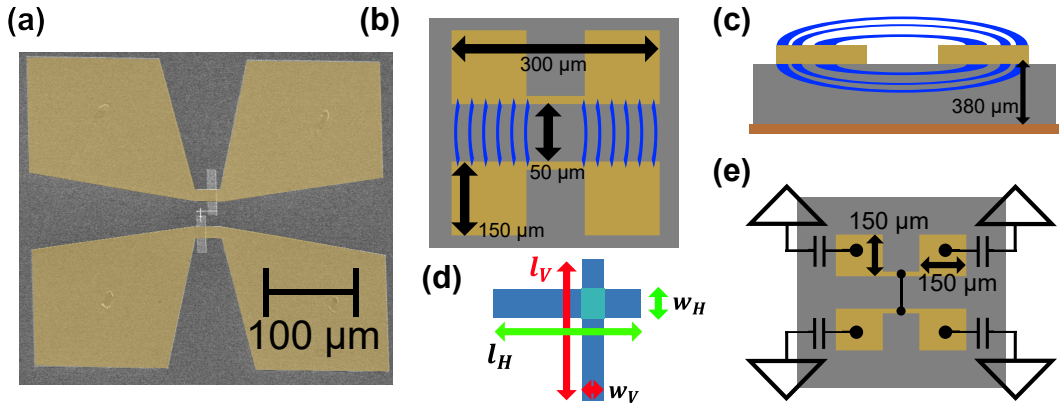

Figure 4.2: **(a)** False-colour scanning electron micrograph of the device and measurement circuit. The large bond pads introduce both capacitance to ground and a stray inductive contribution, modifying the effective circuit environment from the simple RCSJ model shown in Fig. 4.1(c) to the extended circuit shown in Fig. 4.1(d). **(b)** Schematic with dimensions used for the coplanar capacitance calculation in Eq. (**??**). **(c)** Electric field line schematic. The silicon substrate thickness is approximately 380 μm and the relative permittivity is $\epsilon_r = 12$ [173]. This value is used for the microstrip capacitance calculation, while for the coplanar geometry an effective permittivity of $\epsilon_r/2$ is assumed to account for electric field lines extending partially into vacuum. **(d)** Schematic of the ultra-thin junction arms forming the Josephson junction. The dimensions of the horizontal and vertical arms are varied throughout the experiment and strongly influence the inductive environment experienced by the junction. **(e)** Schematic with dimensions used for the microstrip capacitance calculation in Eq. (4.1).

where here $\varepsilon_r = 6$ is the effective relative permittivity, approximated as half that of silicon to account for field lines partly in vacuum, $l = 300$ μm (twice the bondpad length, due to the geometry of the coplanar structure), $w = 150$ μm is the conductor width, $s = 50$ μm is the gap between conductors, and c_0 is again the speed of light. Evaluating this expression gives a coplanar capacitance of approximately 30 fF.

By summing these contributions, we estimate the total bond pad capacitance to be approximately $C_S \approx 60$ fF. Within the 50-100 GHz frequency range relevant for the ICPT process, the impedance of this parasitic capacitance becomes sufficiently small that the bond pads effectively shunt high-frequency signals to ground. As a result, the coupling between the junction and the distant external circuitry is strongly reduced, allowing the high-frequency response to be well approximated by the simplified local parallel *RLC* circuit shown in Fig. 4.1(d) rather than the full electromagnetic environment illustrated in Fig. 4.1(c).

This lumped-element approximation is justified because the ICPT response is well approximated by the fundamental electromagnetic mode formed by the combined inductive environment and the intrinsic junction capacitance within this frequency range. Here, the effective inductance contains contributions both from the stray inductance of the bond pads and from the kinetic inductance of the ultra-thin superconducting leads. The corresponding frequencies map to bias voltages in the range of approximately 100-200 μV

through the Josephson relation, which coincides with the experimentally observed subgap ICPT resonance shown in Fig. 4.1(b).

4.1.2 Extraction of the Electromagnetic Environment

Having established the effective high-frequency RLC environment shown in Fig. 4.1(d), we now turn to the extraction of its parameters from the measured subgap current-voltage characteristics. The real part of the environmental impedance for the simplified parallel

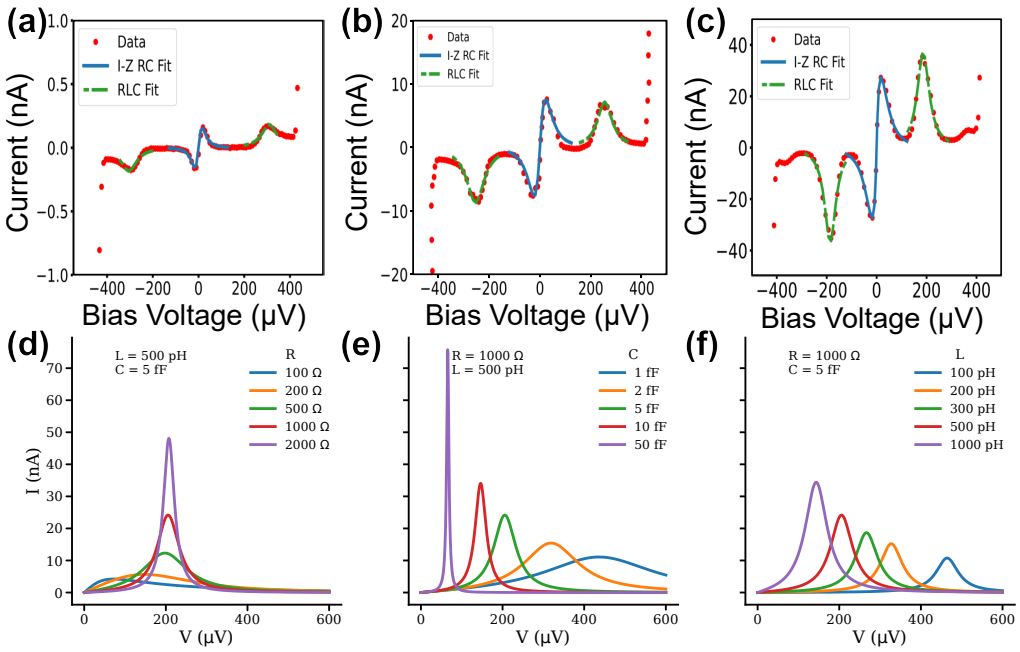

Figure 4.3: **(a-c)** Subgap current-voltage characteristics for junctions with increasing arm width. Solid blue lines represent fits to the broadened supercurrent peak using the Ivanchenko-Zilberman model, while dashed green lines represent the fitted ICPT resonance. **(d-f)** Simulated evolution of the ICPT resonance within the simplified parallel RLC model shown in Fig. 4.1(d). The panels illustrate how variations in **(d)** resistance R, **(e)** capacitance C, and **(f)** inductance L modify the resonance frequency, damping, and overall lineshape.

RLC model is given by [176]

$$\mathrm{Re}(Z_{env}(\omega)) = \frac{\omega^2 \frac{L^2}{R}}{(1-\omega^2 LC)^2 + \omega^2 \left(\frac{L}{R}\right)^2}, \tag{4.4}$$

where R represents the effective dissipation, L the total effective inductive response of the local electromagnetic environment, and C the effective junction capacitance. The impedance exhibits a resonance at a characteristic frequency $\omega_0 = 1/\sqrt{LC}$ with corresponding quality factor $Q = R\sqrt{C/L}$.

Through the AC Josephson relation, this resonance appears experimentally as an en-

hancement of the DC current at a voltage

$$V = \frac{\hbar\omega_0}{2e}. \tag{4.5}$$

For the present devices, the relevant frequency range of approximately 50-100 GHz corresponds to bias voltages between roughly 100-200 μV, consistent with the experimentally observed ICPT resonances shown in Fig. 4.1(b). Representative measurements for junctions of different geometries are shown in Fig. 4.3(a-c). As the junction dimensions increase, the ICPT resonance systematically shifts in position and evolves in shape, indicating modifications of the effective electromagnetic environment surrounding the junction.

To analyse these measurements, we follow the approach of Ref. [138] using the I-Z model introduced in Sec. 2.3.1. The broadened supercurrent peak around zero bias is fitted using the voltage-biased I-Z formalism, allowing the estimatiton of the critical current, the effective environmental dissipation, and the effective electron temperature. The finite-bias ICPT resonance is modelled using the parallel RLC environment introduced in Fig. 4.1(d) together with Eq. (4.4).

The influence of these parameters on the resonance shape is illustrated in Fig. 4.3(d-f). Variations in R primarily modify the damping and resonance broadening through the quality factor, while changes in L and C shift the resonance frequency and alter the overall lineshape. By comparing the measured ICPT resonances to simulations of the model, the environmental parameters can therefore be extracted systematically for different device geometries.

An example of the fitting procedure is shown in Fig. 4.4(a). From the blue I-Z fit, we extract characteristic parameters of approximately $R_{I-Z} \approx 400\ \Omega$, $C_{I-Z} \approx 20$ fF, and $T_{I-Z} \approx 2$ K, with variations below 10% between devices. The elevated electron temperature T_{I-Z} is attributed to the lack of proper electrical filtering during the experiment.

From the ICPT fit (green dashed line), we obtain $R_{RLC} \approx 1\ \text{k}\Omega$, $C_{RLC} \approx 6$ fF, and $L_{RLC} \approx 600$ pH. Repeating this analysis for junctions of different sizes enables the geometry dependence of the extracted inductive and capacitive contributions to be investigated.

Inductance Scaling and Kinetic Contribution The extracted inductance values, shown in Fig. 4.4(b), scale approximately inversely with the junction width w with an additional finite offset L_S. This behaviour indicates that the total inductance contains both a geometry-independent stray contribution and a geometry-dependent kinetic inductance contribution arising from the ultra-thin superconducting leads,

$$L = L_S + L_a. \tag{4.6}$$

Because the arm thickness and width satisfy $wt \ll \lambda^2$, where λ is the London penetration depth, the inductive response is dominated by kinetic inductance. We model the lead contribution as

$$L_a = \mu_0\lambda^2 \left(\frac{l_H}{w_H t_H} + \frac{l_V}{w_V t_V} \right), \tag{4.7}$$

where $l_{H,V}$, $w_{H,V}$, and $t_{H,V}$ denote the dimensions of the horizontal and vertical junction arms shown in Fig. 4.2(d).

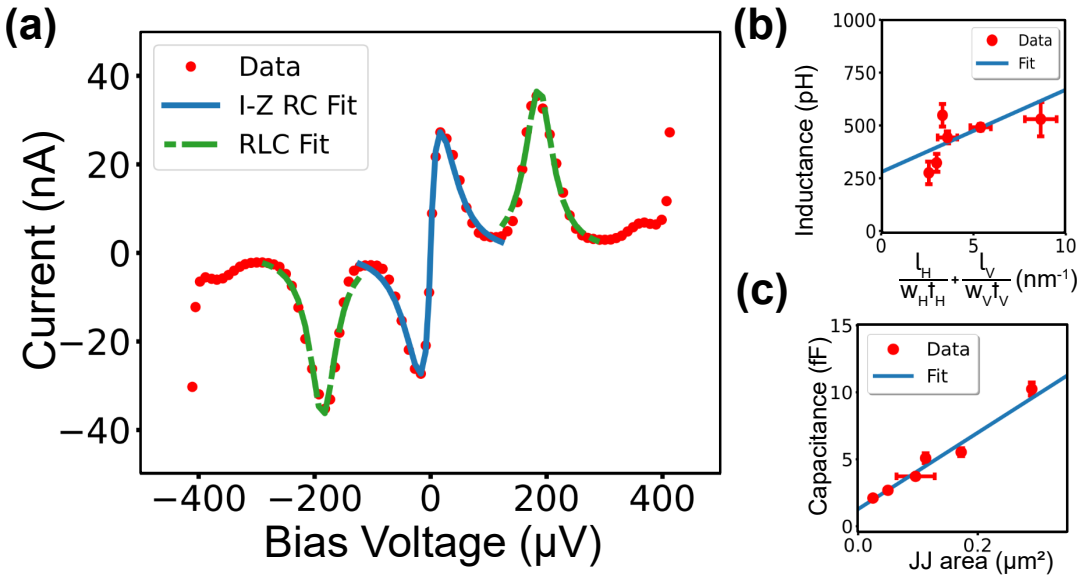

Figure 4.4: **(a)** Example fit of the subgap current-voltage characteristic combining the Ivanchenko-Zilberman model and the ICPT resonance for a 360 nm wide junction. **(b)** Extracted inductance as a function of junction geometry, showing a dominant kinetic inductance contribution. **(c)** Extracted capacitance as a function of junction area, exhibiting approximately linear scaling with device size.

Fitting this expression to the extracted inductances yields $L_S \simeq 250$ pH and $\lambda \simeq 176$ nm. This extracted penetration depth is consistent with the expected value for thin Al films in the dirty limit, where $\lambda = \lambda_L(0)\sqrt{\xi_0/l} \simeq 200$ nm [143]. This calculation assumes bulk Al parameters ($\lambda_L(0) = 16$ nm, $\xi_0 \simeq 1.6$ μm) and a mean free path $l_e \simeq 9.5$ nm, a value slightly smaller than the film thickness, as is typical for evaporated thin films [143]. The finite offset L_S agrees reasonably well with the stray bond pad inductance estimated from the geometric model discussed previously and is comparable to values reported in related Josephson circuits [137].

Capacitance Scaling and Geometric Contributions The extracted capacitance values shown in Fig. 4.4(c) scale approximately linearly with the junction area, consistent with a dominant geometric junction capacitance. The scaling

$$C_j = c_j w^2 \tag{4.8}$$

yields a specific capacitance of approximately $c_j \simeq 29$ fF/μm^2, comparable to values reported for Al-AlO$_x$-Al tunnel junctions fabricated using double-angle evaporation [177].

A small finite offset remains even at vanishing junction area, which we attribute to parasitic capacitance from the surrounding bond pads and junction leads. These parasitic contributions are consistent with the geometric capacitance estimates introduced in the previous section.

Together, these results support the interpretation that the observed subgap resonances originate from a well-defined on-chip electromagnetic mode formed by the junction capacitance and the combined kinetic and stray inductive environment.

4.1.3 Magnetic Field Dependence

To further characterise the junctions, we investigate the evolution of the current-voltage characteristics (IVCs) under an applied in-plane magnetic field $B_{\text{ext}}^{\parallel}$ parallel to one of the junction arms. Figure 4.5(a) illustrates this evolution for a representative 360 nm wide junction measured at $T = 25$ mK. As $B_{\text{ext}}^{\parallel}$ increases, the Josephson peak is progressively

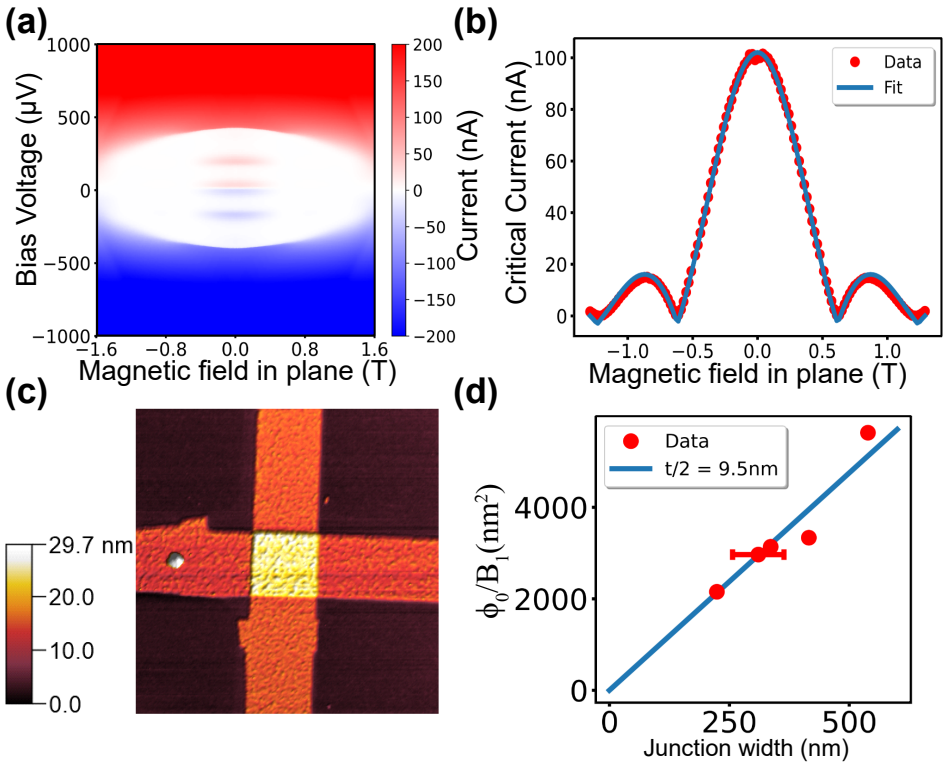

Figure 4.5: **(a)** Current-voltage characteristics as a function of in-plane magnetic field at $T = 25$ mK. **(b)** Extracted critical current showing a Fraunhofer-like interference pattern. The solid line is a fit to the standard interference model. **(c)** Atomic force microscopy (AFM) image of the junction area ($2\,\mu\text{m} \times 2\,\mu\text{m}$). **(d)** Extracted effective junction area as a function of junction width, showing linear scaling.

suppressed, disappearing almost completely at $B_{\text{ext}}^{\parallel} = 0.5$ T (Figure 4.5(b)), while the superconducting gap Δ shrinks by less than 10%. Above an upper critical field $B_c^{\parallel} \approx 1.6$ T, the Al electrodes transition to the normal state and the IVC becomes ohmic and featureless, consistent with reports for thin Al films.

The critical current $I_c(B)$ is extracted by fitting the supercurrent peak using a modified I-Z model in which the ohmic environmental impedance is replaced by the real part of the frequency-dependent impedance of a parallel RC circuit [138].

The fitting procedure is initialised using the $B = 0$ line cut from Fig. 4.5(a). From this measurement, the Ambegaokar-Baratoff estimate for the equilibrium critical current is calculated and used together with the modified I-Z model to extract the environmental parameters, yielding $R_{I-Z} \approx 400\ \Omega$, $C_{I-Z} \approx 20$ fF, and an effective electron temperature $T_{I-Z} \approx 2$ K. These parameters are subsequently fixed for all finite-field fits, leaving the critical current as the only free fitting parameter.

The resulting $I_c(B)$ dependence, shown in Fig. 4.5(b), exhibits a clear Fraunhofer-like interference pattern well described by

$$I_c(B) = \frac{\Delta(B)}{\Delta(0)} I_c(0) \left| \frac{\sin(\pi B A_{\text{eff}}/\Phi_0)}{\pi B A_{\text{eff}}/\Phi_0} \right|, \tag{4.9}$$

where the prefactor $\Delta(B)/\Delta(0)$ accounts for the gradual suppression of the superconducting gap with magnetic field. From this fit, the effective junction area A_{eff} is extracted.

Geometric Scaling and Effective Thickness We analyse the magnetic interference pattern using the methodology outlined in Sec. 2.3.2.

The extracted effective areas are plotted as a function of junction width in Fig. 4.5(d). A clear linear scaling is observed, indicating that the interference pattern is governed by a well-defined geometrical area. In the thin-film limit ($t \ll \lambda$), the magnetic field fully penetrates the superconducting electrodes, and the effective area can be approximated as $A_{\text{eff}} \simeq w t_{\text{eff}}/2$. From a linear fit to the data, we extract $t_{\text{eff}}/2 \approx 9.5$ nm.

This result is consistent with independent atomic force microscopy (AFM) measurements of the junction stack shown in Fig. 4.5(c), which yield an average thickness of approximately 24.2 nm. The reduced effective superconducting thickness can be explained by the presence of oxidised aluminium layers: approximately 4-5 nm of the top Al electrode and 1-2 nm near the substrate interface are converted into oxide, leaving an effective superconducting thickness of roughly 18-20 nm [178, 179]. The extracted effective area therefore agrees well with the expected geometrical dimensions of the junctions.

4.1.4 High-Field Spectroscopy

We now investigate the spectroscopic response of the junctions at high magnetic fields, focusing on the evolution of the ICPT resonance. Figure 4.6(a) shows the differential conductance of a 360 nm junction for $B_{\text{ext}}^{\parallel} > 0.8$ T. While both the Josephson peak and superconducting gap are reduced, the ICPT current peaks remain clearly visible as inflection points (V_r, marked by black stars) in the conductance.

Importantly, the resonance shifts systematically towards lower bias voltages with increasing magnetic field. Since the resonance frequency is defined by $f_r = 1/\sqrt{(L_a + L_s)C_j}$, this shift directly reflects an increase in the kinetic inductance L_a of the junction arms. Using previously extracted values of $L_s \simeq 0.25$ nH and $C_j = 6$ fF, we extract the field dependence of L_a. The normalised variation, shown in Fig. 4.6(c), exhibits a clear quadratic increase with the applied magnetic field.

Pair-Breaking and Diffusion Constant This quadratic behaviour is consistent with magnetic-field-induced pair breaking in the thin-film limit. Within the pair-breaking framework for thin superconducting films (see Sec. 2.3.2), the kinetic inductance variation follows:

$$\frac{L_a(B) - L_a(0)}{L_a(0)} = \frac{\pi}{24} \frac{D e^2 B^2 t^2}{\hbar k_B T_c(0)} = A_1 \cdot B^2, \tag{4.10}$$

where A_1 is a prefactor determined by the diffusion constant D and film thickness t. Fitting this dependence and using $T_c(0) \approx 1.26$ K (extracted from $\Delta(B = 0)$), we obtain

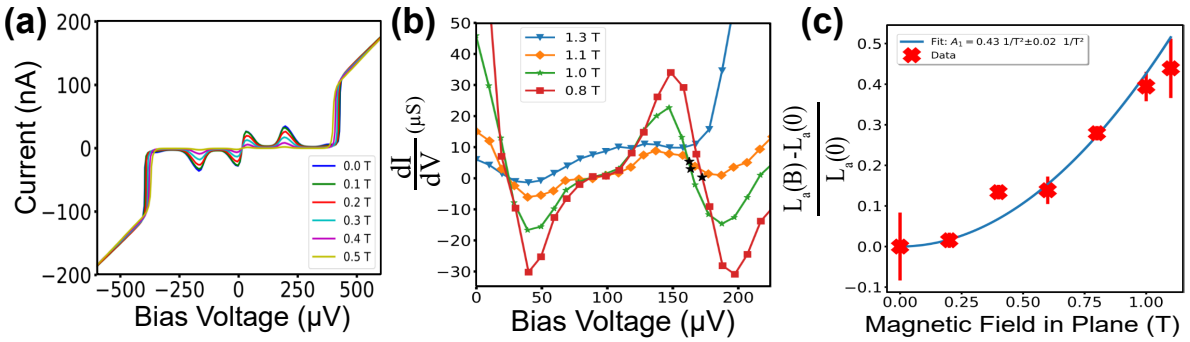

Figure 4.6: **(a)** Voltage-biased IVC at 20 mK as a function of magnetic field. **(b)** Differential conductance showing the evolution of the ICPT resonance with increasing field. The resonance shifts to lower bias, reflecting a change in the environmental mode frequency. **(c)** Extracted kinetic inductance as a function of magnetic field. The solid line shows a quadratic dependence consistent with pair-breaking.

diffusion constants D ranging from 19 to 36 cm^2/s for film thicknesses between 11 and 8 nm, respectively. These values are in good agreement with previously reported findings for thin aluminium films of similar thickness [155, 157, 180].

Spectrometer Functionality at High Fields Crucially, the persistence of the ICPT resonance in the IVCs at $B_{\mathrm{ext}}^{\parallel} > 1$ T establishes these ultrathin Al-AlO_x-Al junctions as robust on-chip spectrometers capable of probing microwave-frequency excitations. These devices are well-suited for investigating sub-gap features, such as Andreev bound states (ABS), under the high-field conditions necessary to access topological regimes. Even at $B_{\mathrm{ext}}^{\parallel} \sim 1.3$ T, the superconducting gap remains finite, corresponding to frequencies on the order of $\sim$ 70-100 GHz. The potential implementation of a spectrometer based on these junctions, including a detailed assessment of possibilities and challenges, is further discussed in Sec. 5.

4.2 Magnetic-Field Anisotropy of the Josephson Diode Effect in Ferromagnetic Hybrid Nanowires

The Josephson diode effect serves as a critical diagnostic for hybrid systems, as its realisation requires the same fundamental symmetry-breaking conditions as those needed for topological superconductivity (see Secs. 2.2 and 2.2.1, and Figs. 2.8, 2.10(d). Beyond its fundamental significance, the JDE provides a superconducting analogue for dissipationless rectification and direction-dependent signal control, with high potential for on-chip isolators and circulators in quantum information architectures [181–183]. Non-reciprocal supercurrents arise when both IS and TRS are lifted. In hybrid heterostructures, IS is intrinsically broken by structural inversion asymmetry (SIA) via Rashba spin-orbit coupling (SOC), or extrinsically through device geometry and asymmetric contacts (extrinsic device asymmetry, EDA) [184]. TRS is lifted either by an external magnetic field B_{ext} or an internal exchange field B_{exc} (see Sec. 2.2.1 and Fig. 2.11). These fields, occasionally aided by orbital-induced phase gradients [34], reshape the Andreev spectrum to produce an asymmetric current-phase relation (CPR) and unequal critical currents ($I^+ \neq I^-$) [118, 185–190].While the JDE has been demonstrated in diverse platforms, ranging from planar InAs-based junctions [74, 158, 159] to twisted bilayer graphene [191] and SQUIDs [192], the InAs-EuS-Al nanowire system is uniquely suited to hosting these ingredients in a single hybrid architecture (see Sec. 2.3.3 and Table 2.4). In this work, we utilise these hybrid nanowires to combine strong Rashba SOC, Al-induced pairing, and proximity-induced magnetism [193, 194]. Building on earlier studies of EuS-based hybrids [61, 76], we employ B_{ext} as a vector probe. By varying the three-dimensional orientation of the magnetic field relative to the effective spin-orbit field axis, we investigate the evolving internal symmetry-breaking configuration and the mechanisms governing robust non-reciprocity in this platform [58, 75, 195].

4.2.1 Device Architecture and Measurement Setup

The morphology and structural characteristics of the three devices investigated in this study are shown in the scanning electron micrographs in Fig. 4.7(a-c). Devices A, B, and C are fabricated from the same InAs-EuS-Al hybrid nanowire platform and share the same overall junction architecture, illustrated schematically in the cross-section shown in Fig. 4.7(d). Despite these similarities, the devices exhibit distinct geometric differences. In particular, Devices A and C display noticeable mechanical bending of the nanowire, whereas Device B remains comparatively straight. As discussed in later sections, these structural differences may influence the magnetic configuration and the resulting non-reciprocal transport response.

Device A provides the most comprehensive dataset and is therefore used for the primary analysis throughout this section. Devices B and C are subsequently introduced for comparison, with Device B exhibiting qualitatively different behaviour from Device A, while Device C shows a response more closely resembling that of Device A.

All low-temperature measurements were performed at a base temperature of 25 mK using the experimental setup described in Sec. 3.2 and the measurement configuration illustrated in Fig. 3.5(a).

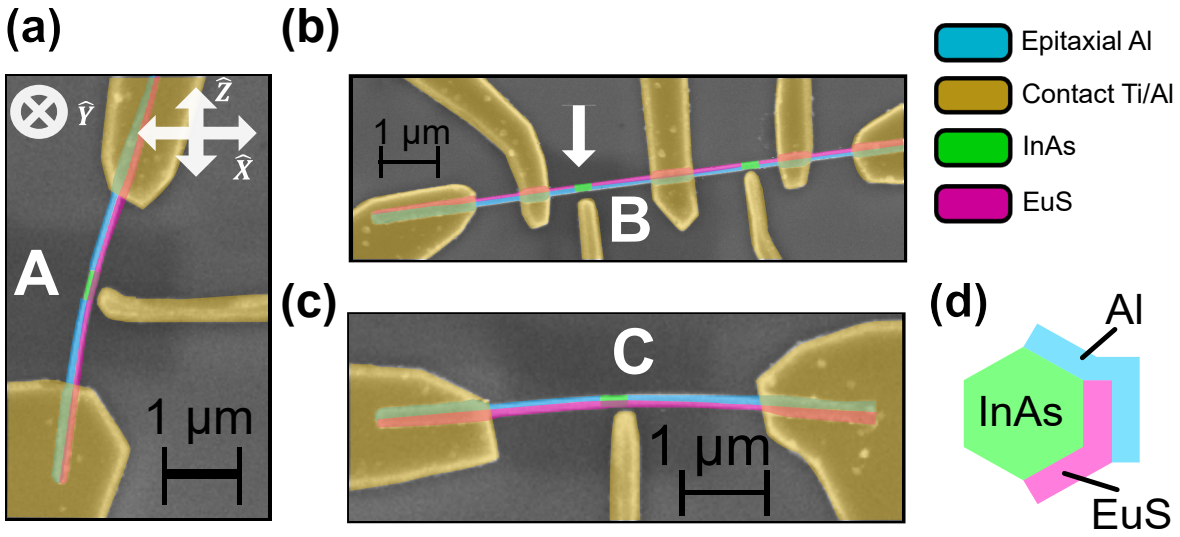

Figure 4.7: Morphology and architecture of InAs-EuS-Al hybrid nanowire junctions. **(a-c)** False colour Scanning electron micrographs of Devices A, B, and C, respectively. Each device features a central weak link defined by selectively etching Al. False colouring highlights the epitaxial Al shell (blue), the exposed InAs core (green), the EuS layer (pink), and the evaporated Ti/Al contacts (yellow). In **(a)** the three axes of the vector magnet used in the measurements are indicated in white. **(d)** Schematic cross-section of the hybrid nanowire, illustrating the InAs core with 6 nm-thick epitaxial Al and EuS layers. Devices A and C exhibit characteristic mechanical bending, while Device B maintains a straight morphology.

Initial Characterisation of Device A Prior to the application of external magnetic fields, the transport properties of Device A were characterised at base temperature after zero-field cooldown. Representative current-voltage characteristics are shown in Fig. 4.8. From the high-bias regime (Fig. 4.8(b)), we extract a normal-state resistance of approximately $R_N \approx 6.0$ kΩ, while the low-bias regime (Fig. 4.8(a)) exhibits a critical current of approximately $I_c \approx 2.3$ nA.

The differential resistance shown in Fig. 4.8(c) reveals pronounced superconducting gap and subgap features associated with MAR. Additionally, the overlap of the positive and negative normal-state branches indicates that the transport asymmetry discussed later primarily originates from the superconducting state rather than from an asymmetric normal-state resistance.

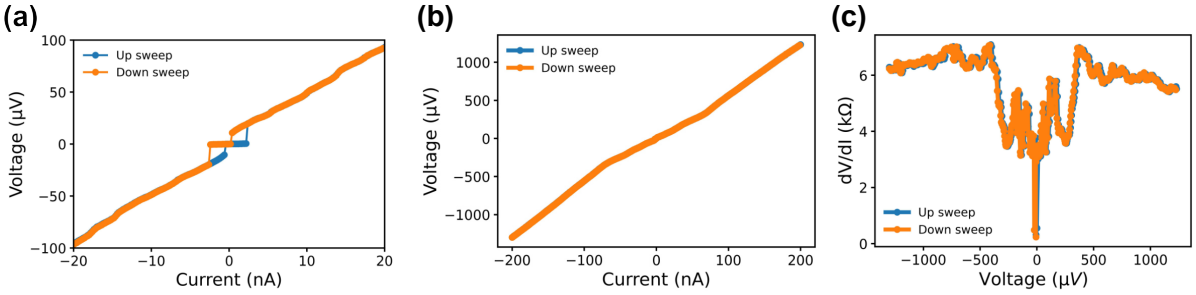

Figure 4.8: Current-voltage characteristics of Device A measured at base temperature after zero-field cooldown and prior to the application of any external magnetic field. **(a)** Low-bias current-voltage characteristics showing the superconducting branch and switching into the resistive state at critical currents of approximately $I_c \approx 2.3$ nA. **(b)** High-bias current-voltage characteristics extending into the normal regime, from which a normal-state resistance of $R_N \approx 6.0$ kΩ is extracted. The positive and negative normal-state branches overlap closely, indicating negligible asymmetry in the normal-state transport. **(c)** Differential resistance (dV/dI) obtained from lock-in measurements as a function of voltage, revealing pronounced superconducting gap and subgap features associated with MAR.

Critical Current Extraction Procedure We use a well-established definitition of the diode efficiency η which is defined as

$$\eta = \frac{|I^+| - |I^-|}{|I^+| + |I^-|}, \tag{4.11}$$

where I^+ and I^- are the critical currents associated with the positive and negative branches of the current biased IVC. To obtain these values we utilise a threshold voltage V_{th}. The data were obtained by sweeping the bias current from the maximum negative value to the maximum positive value and back, passing zero bias twice (see Fig. 4.9(a).

To extract the critical current we first remove the negative voltage data points for the upward sweep and the positive voltage data points for the downward sweep as these will be associated with the retrapping current (see Fig. 4.9(b)). Then we flip the negative data points into the positive quadrant and we adjust both the negative and positive data to remove any voltage offset. Afterwards we set a $V_{th} = 3\mu$V (for device A), using this threshold we identify the current value corresponding to the threshold crossing in both branches and establish these as our I^+ and I^- (see Fig. 4.9(c)). For the data in Fig. 4.9 which is a line cut from a magnetotransport measurement of device A we obtain a remanent diode efficiency of $\eta(0) \approx 8.2\%$. This finite zero-field diode efficiency is consistent with a remanent exchange field associated with the EuS layer.

4.2.2 Common Transport Signatures of the EuS Hybrid Devices

To establish a common baseline for the transport properties of the InAs-EuS-Al hybrid nanowire devices, we first examine the signatures that are reproducible across multi-

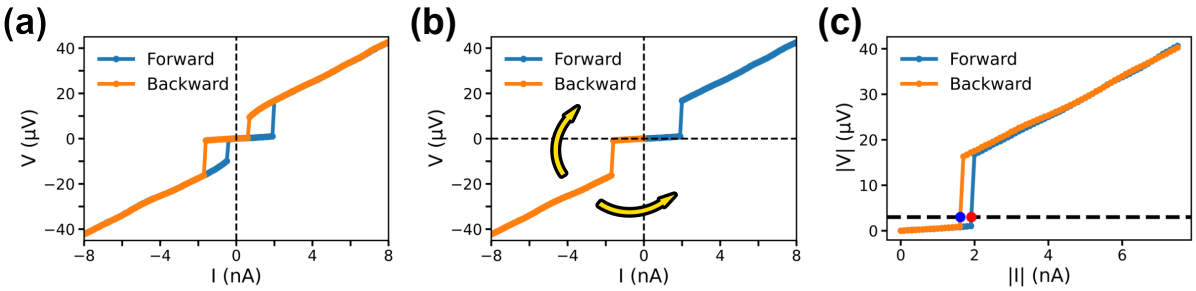

Figure 4.9: critical current extraction protocol and zero-field non-reciprocity for Device A, note that this data is taken after an external field was used to polarise the EuS layer. **(a)** Representative full-bias current-voltage characteristic (IVC). **(b)** Isolated forward and backward branches. **(c)** Precise determination of positive (I^+) and negative (I^-) critical currents using a fixed 3 μV voltage threshold (horizontal dashed line). Even in the absence of an external polarising field ($B_{\text{ext}} = 0$), the device exhibits a remanent diode efficiency of $\eta(0) \approx 8.2\%$, calculated via Eq. (4.11).

ple samples. We begin by characterising the transport response immediately following zero-field cooldown, where two of the investigated devices exhibit a finite diode efficiency prior to the application of any external magnetic field. For the third device, comparable cooldown measurements were not available, preventing a direct determination of whether a similar finite diode efficiency is also present. We then investigate the magnetic-field evolution of the superconducting transport to determine the coercive fields and characterise the hysteretic magnetotransport associated with the EuS-induced exchange field. In contrast to the cooldown diode efficiency, the magnetic hysteresis exhibits qualitatively similar behaviour across all investigated devices.

Initial Finite Diode Efficiency Following zero-field cooldown, both Device A and Device B exhibit unequal positive and negative critical currents prior to the application of any external magnetic field, as shown in Fig. 4.10. For Device A, we find a difference of approximately 0.2 nA between I^+ and I^-. Using Eq. (4.11) this corresponds to a cooldown diode efficiency of $\eta \approx 4.2\%$. Device B exhibits a comparable cooldown efficiency of $\eta \approx 3.8\%$.

The presence of a finite diode efficiency in the absence of an externally applied magnetic field suggests an intrinsic TRS breaking contribution in these devices. One possible explanation is that, upon cooling, magnetic domains may form in the EuS layer with sizes large enough that their effects do not average out over the junction length or the Al coherence length [196].

Coercive field To investigate the magnetic influence of the EuS layer across different samples, we perform magnetotransport measurements on Devices A, B, and C. Figure 4.11 presents the differential conductance dI/dV as a function of external magnetic field B_{ext} and bias voltage V.

The full dI/dV maps shown in Fig. 4.11(a,c,e) illustrate the evolution of the superconducting gap and subgap structure under the combined influence of the external magnetic field and the proximity-induced exchange field. A clear hysteretic behaviour is

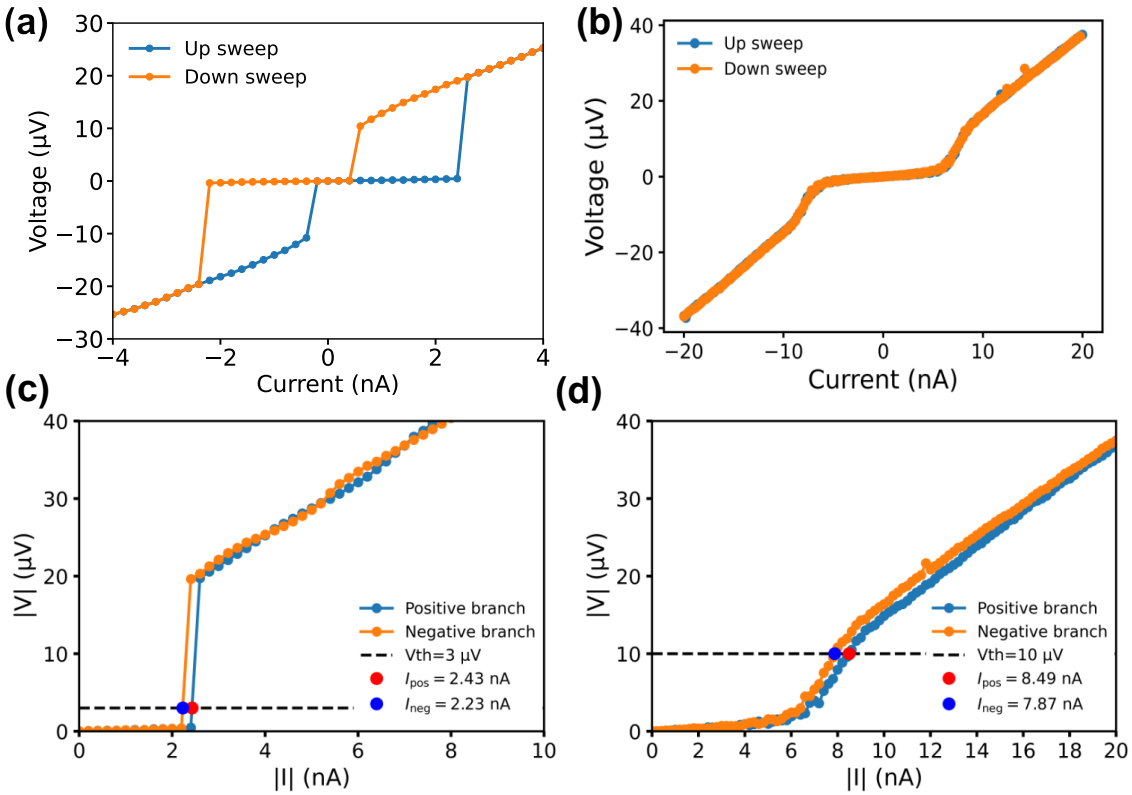

Figure 4.10: Current-voltage characteristics (IVCs) of devices A and B measured at base temperature ($T = 20$ mK) prior to the application of any external magnetic field. **(a)** Current-biased IVCs of device A. **(b)** Current-biased IVCs of device B. **(c)** Extracted critical currents of device A using the procedure shown in Fig. 4.9, yielding a cooldown diode efficiency of $\eta \approx 4.2\%$. **(d)** Extracted critical currents of device B, yielding a cooldown diode efficiency of $\eta \approx 3.8\%$.

observed in all three devices, as highlighted by the side-by-side polarisation comparisons in Fig. 4.11(b,d,f). From these measurements, we extract coercive fields of approximately 20 mT for Devices A and C and 18 mT for Device B. The consistency of the coercive fields across all three devices demonstrates that the EuS layer is robustly coupled to the superconducting transport in each junction.

The primary motivation for incorporating a ferromagnetic EuS layer is the induction of an effective internal exchange field, B_{exc}. Such exchange fields are important ingredients for realising both the JDE and topological superconductivity, as they can partially replace the need for externally applied magnetic fields [29].

Further insight into the magnetic proximity effect is obtained from the evolution of the superconducting gap and MAR features. The positions of the gap and subgap maxima shift depending on the polarisation state of the EuS layer, producing a hysteretic offset of approximately ±20 mT between opposite sweep directions. This behaviour is consistent with a remanent B_{exc} that persists even when the external magnetic field is returned to zero [29, 61, 76].

With increasing magnetic field strength, the gap and subgap features shift towards lower voltages. While previous studies have reported proximity-induced spin splitting of

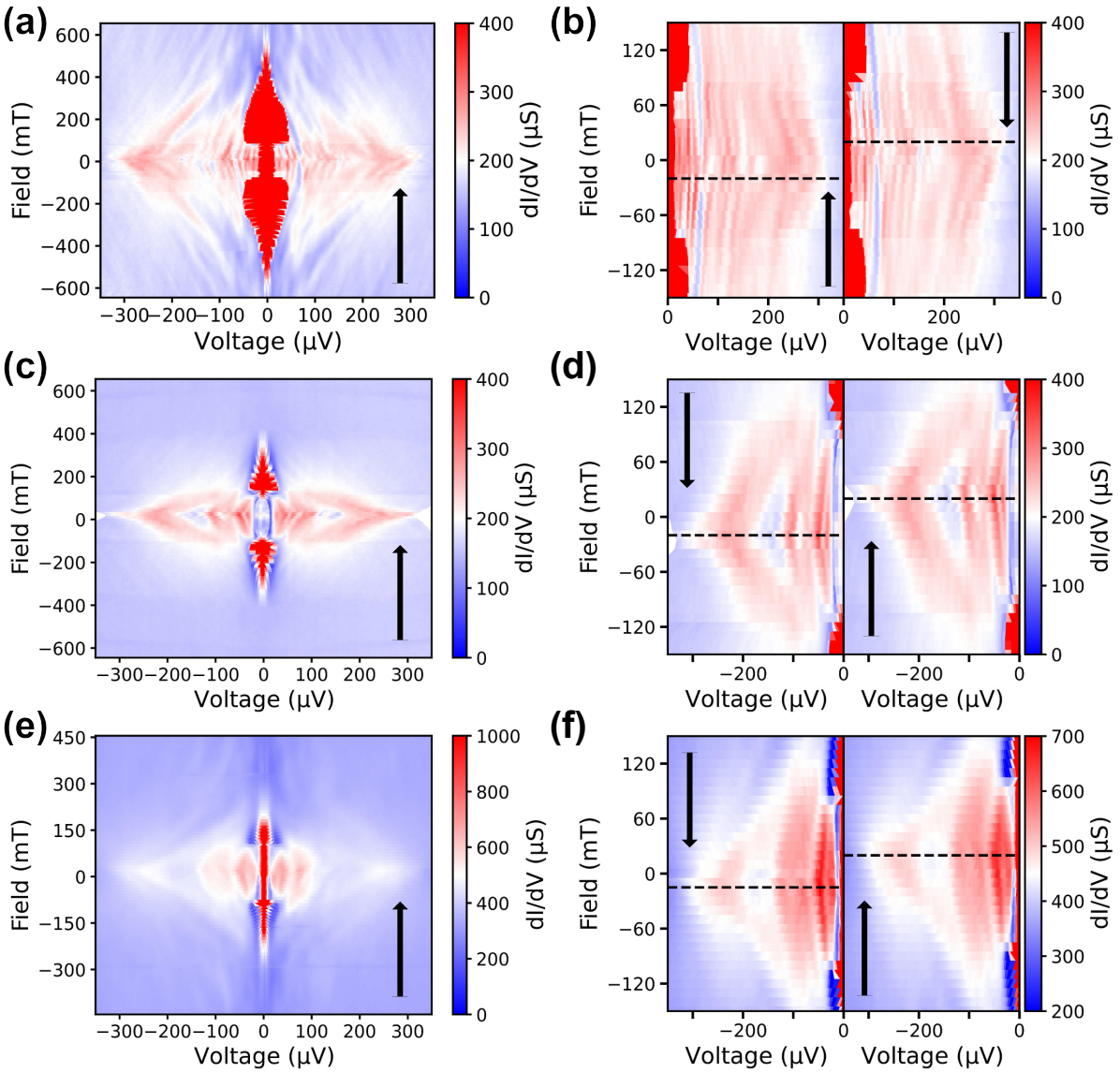

Figure 4.11: Comparative magnetotransport and hysteresis characterisation for Devices A, B, and C. **(a, c, e)** Full dI/dV maps showing the conductance as a function of bias voltage and B_{ext} for one polarisation (B_{ext} sweep direction as indicated by the black arrows) of the EuS layer for Device A, B, and C, respectively. **(b, d, f)** Detailed views of the superconducting gap and sub gap features. Each panel displays side-by-side images comparing positive and negative polarisations of the EuS. The observed hysteresis in all three devices, with coercive fields of 20 mT (Device A), 18 mT (Device B), and 20 mT (Device C) confirms the consistent magnetic coupling of the EuS layer to the junction.

the superconducting gap [61], these observations were primarily made in the tunnelling regime. In the present devices, the relatively high conductance ($G > e^2/h$) places the junction outside the tunnelling limit, likely preventing a direct spectroscopic resolution of the spin-split density of states despite the clear influence of the exchange field.

Having established that all devices exhibit both finite cooldown non-reciprocity and robust magnetic proximity effects, we next investigate how the Josephson diode efficiency evolves under externally applied magnetic fields, beginning with the detailed case of Device A.

4.2.3 Magnetic Field Magnitude Dependence

Having established that an external magnetic field applied along the nanowire axis can modify the polarisation state of the EuS layer and produce a remanent exchange field, we next investigate how the Josephson diode efficiency evolves under an applied axial magnetic field. In this configuration, the external field may influence the non-reciprocal transport both indirectly through the EuS-induced exchange field and directly through Zeeman and orbital coupling to the superconducting weak link. To probe these effects, we perform axial magnetic-field sweeps while recording full current-voltage characteristics, allowing the positive and negative critical currents to be extracted using the procedure established in Fig. 4.9.

Impact on diode efficiency η Axial magnetic field sweeps on Device A are shown in Fig. 4.12(a). The extracted positive and negative critical currents are presented in Fig. 4.12(b). As $|B_{\text{ext}}|$ approaches ≈ 85 mT, both critical currents exhibit a sharp increase before decreasing again at higher magnetic fields. This feature coincides with the magnetic field range where the thick superconducting leads are expected to transition to the normal state [3, 197].

Magnetising the device by sweeping to large field magnitudes induces a finite diode effect that persists at $B_{\text{ext}} = 0$, demonstrating that the remanent exchange field alone can generate non-reciprocal transport in these device with Rashba SOC. Following such magnetisation, we observe a zero-field efficiency of $\eta \approx 8.2\%$ (calculated from $I^+ \neq I^-$ in Fig. 4.12(b)). This value, obtained without electrostatic gating, is comparable to results in similar nanowire devices where gating and external fields were required to reach the superconducting regime [76].

The evolution of the diode efficiency $\eta(B_{\text{ext}})$ is shown in Fig. 4.12(c). As the magnetic-field magnitude increases, η initially decreases before increasing again at larger fields. However, the response is not symmetric under magnetic-field sign inversion. In particular, the magnitude of the diode efficiency differs substantially between positive and negative magnetic fields, with $\eta(-200\text{ mT}) > \eta(+200\text{ mT})$. A similar overall behaviour is observed for both sweep directions (Fig. 4.12(d)), with a small hysteresis near zero field associated with the coercive field of the EuS layer.

These observations indicate that the diode response contains both a field-dependent contribution and an approximately field-independent baseline component [76]. The persistence of a finite diode efficiency at zero external magnetic field suggests that the non-reciprocal transport is not governed solely by B_{ext}, but also by an internal symmetry-breaking configuration associated with the interplay between spin-orbit coupling and the EuS-induced exchange field. One possible origin is the direct EuS contact on a single InAs facet, which could locally modify the effective spin-orbit coupling depending on the magnetisation state of the EuS layer. More generally, the asymmetric field response may reflect a complex interplay between spin-orbit coupling, exchange fields, and multiple

Andreev bound states [111, 112]. However, such models would typically predict a sign reversal of η upon magnetic-field inversion, which is not observed here.

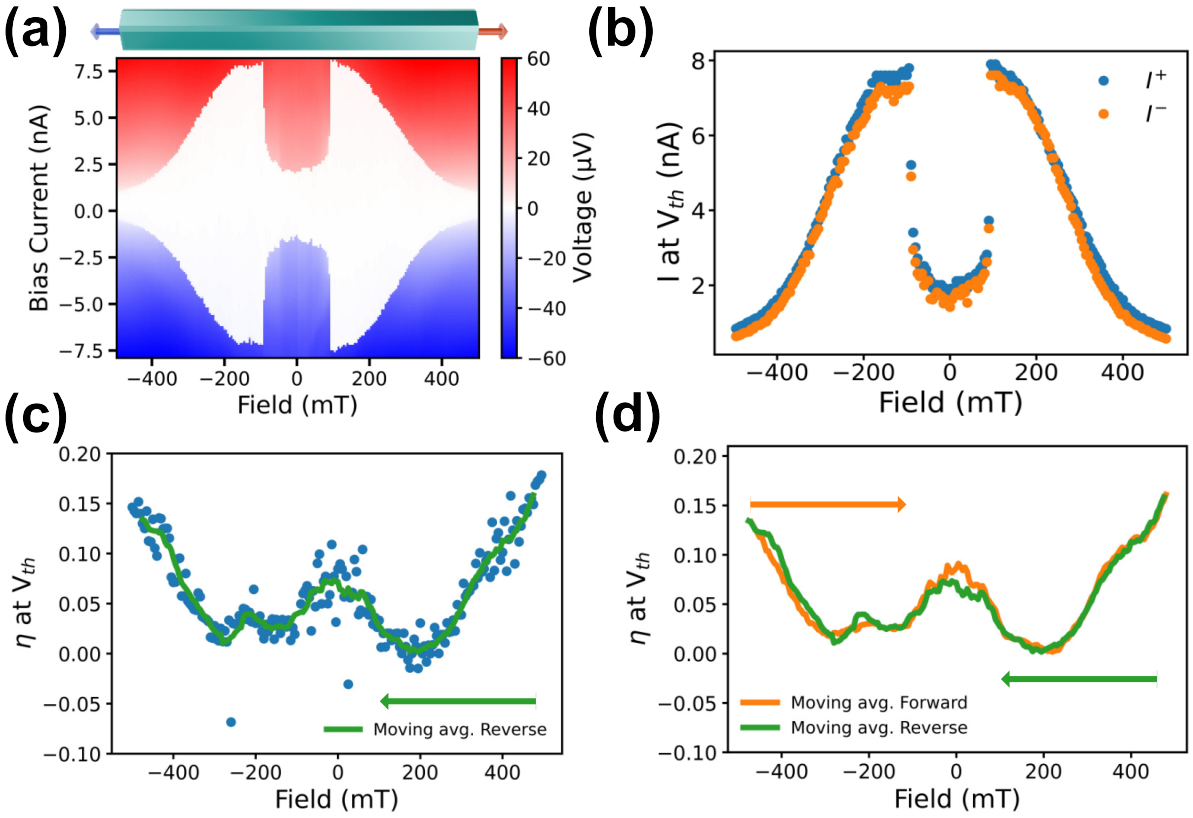

Figure 4.12: Axial field dependence of Device A. **a)** Magnetotransport map of voltage as a function of bias current and B_{ext} along the nanowire axis. **b)** Magnetic-field dependence in Device A of the positive and negative critical currents, I^+ and I^- at a 3 μV voltage threshold. **c)** Diode efficiency η (blue dots) as a function of magnetic field. The solid green line indicates a ten-point moving average. The magnetic field was stepped from positive to negative as indicated by the green arrow. **d)** Moving averages of the diode efficiency for forward (orange arrow) and reverse (green arrow) magnetic-field sweeps.

The absence of a simple sign reversal of η under inversion of the axial magnetic field suggests that the diode response is not determined solely by the magnitude or polarity of B_{ext}. Instead, the results indicate a more complex symmetry-breaking configuration involving the interplay between the external field, the EuS-induced exchange field, and the effective spin-orbit field of the junction. To further investigate the directional dependence of this interplay, we next examine the response to magnetic fields applied perpendicular to the nanowire axis.

4.2.4 Perpendicular Magnetic Field Dependence

Following the characterisation of the axial field response, we investigate the influence of magnetic fields applied perpendicular to the nanowire axis within the substrate plane. In

this configuration, enhanced non-reciprocal transport is expected when the external field B_{ext} aligns with the effective spin-orbit field of the junction, assuming that SOC field lies within the substrate plane [74].

As shown in Fig. 4.13(a), the critical currents I^+ and I^- exhibit a sharp peak around $|B_{\text{ext}}| \approx 90$ mT. As in the axial-field configuration, this feature coincides with the field range where the thick superconducting leads transition to the normal state. Beyond this peak, however, the perpendicular configuration reveals a much more pronounced modulation of the diode efficiency η over a broad field range compared to the axial case.

The corresponding diode efficiency is shown in Fig. 4.13(b). In contrast to the axial-field configuration, the diode efficiency is significantly enhanced in the $|B_{\text{ext}}| = 100$-200 mT field range when B_{ext} is applied perpendicular to the nanowire axis. The efficiency exhibits a pronounced oscillatory dependence on magnetic field with a characteristic scale of approximately 100 mT and reaches values between 5% and 15%, which are comparable to, or larger than, values reported for gate-tuned III-V nanowire Josephson diode devices [74, 76, 192].

At magnetic fields approaching ±300 mT, superconductivity is nearly fully suppressed and the diode efficiency vanishes. A comparison of forward and reverse magnetic-field sweeps, shown in Fig. 4.13(c), reveals a hysteretic shift of the diode efficiency along the magnetic-field axis that exceeds the coercive field (~ 20 mT) extracted from the axial-field measurements. This behaviour likely reflects the magnetic anisotropy of the elongated EuS layer [162, 196].

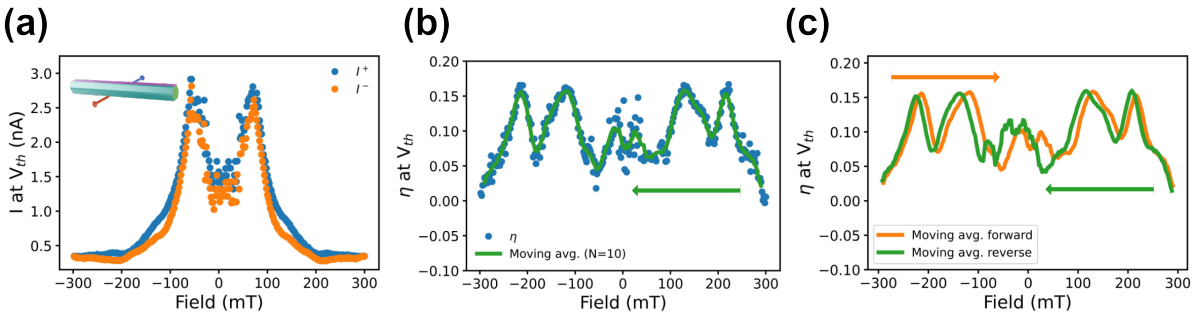

Figure 4.13: a) Magnetic-field dependence in Device A of the positive and negative critical currents, I^+ and I^- at a 3 μV voltage threshold. Insert **a)** Illustration of the nanowire (light blue) and the magnetic-field orientations (red and blue arrows) perpendicular to the nanowire axis within the substrate plane, used for the transport measurements. The critical current increases around $|B| \approx 90$ mT, corresponding to the transition of the thick electrodes to the normal state, resulting in the lowering of the effective temperature in the junction. **b)** Diode efficiency η as a function of magnetic field. The solid green line denotes a ten-point moving average. The magnetic field was swept from positive to negative values as indicated by the green arrow. An oscillatory behaviour is observed, and the efficiency is asymmetric with respect to zero field. **c)** Moving averages of the diode efficiency for forward (negative ferromagnetic polarisation, orange arrow) and reverse (positive ferromagnetic polarisation, green arrow) magnetic-field sweeps. The forward sweep is approximately symmetric in field, whereas the reverse sweep is shifted towards negative fields.

Despite the hysteretic shift observed in the perpendicular-field configuration, the overall sign of η remains unchanged for both sweep directions. Similar to the axial-field measurements, this suggests the presence of a robust baseline contribution to the diode efficiency that is not solely determined by the external magnetic field, but also by an internal symmetry-breaking configuration associated with the EuS-induced exchange field and spin-orbit coupling. This also indicates that the effective SOC field may not lie entirely within the substrate plane [74]. To further investigate the three-dimensional symmetry-breaking configuration of the device, we therefore next examine the angular dependence of the diode response for magnetic-field rotations in multiple orthogonal planes.

4.2.5 Angular Dependence

To further investigate the role of magnetic-field orientation, we perform angle-dependent measurements at a fixed magnetic-field magnitude of $|B_{\text{ext}}| = 100$ mT. This field magnitude was chosen to ensure that the thick Al electrodes remain in the normal state, thereby improving the thermalisation of the junction to the bath temperature (see Figs. 4.12(a) and 4.13(a)). Given the faceted geometry of the nanowire and its asymmetric shell coverage, the magnetotransport response is expected to depend sensitively on the magnetic-field orientation [162]. The field was rotated through $\theta = [0°, 406°]$ in 203 discrete steps across three orthogonal spatial planes, with a full IVC recorded at each angle.

We first consider rotations in the plane normal to the nanowire axis (Fig. 4.14(a, d, g). In this configuration, the diode efficiency $\eta(\theta)$ exhibits pronounced maxima near $\theta = 80°$ and 240°. These peaks coincide with the angles where the critical current I_c is most suppressed (Fig. 4.14(d)), a correlation often associated with orbital contributions to the JDE [198]. However, we do not observe the expected simple sign reversal of η when the polarity of B_{ext} is inverted [34]. Although, η undergoes a sign change specifically in the angular regions where I_c is maximised ($\theta = 160°$ and 340°, green arrows in Fig. 4.14(g)). At these orientations, the diode response may be dominated by an orbital contribution or by the alignment of B_{ext} with the effective spin-orbit field.

A different behaviour emerges when the field is rotated parallel to the Al-coated facets (Fig. 4.14(b, e, h)). In this plane, I_c remains relatively large and exhibits only weak angular modulation. Correspondingly, η is significantly suppressed, never exceeding the minima observed in the previous rotational plane in Fig. 4.14(a, d, g).

Finally, rotations within the substrate plane (xz-plane, Fig. 4.14(c, f, i)) reveal critical currents with pronounced modulations similar to the plane in Fig. 4.14(a, d, g). A clear maximum in η appears near $\theta = 130°$ (Fig. 4.14(i); however, this feature lacks a symmetry-related counterpart at $\theta + 180°$.

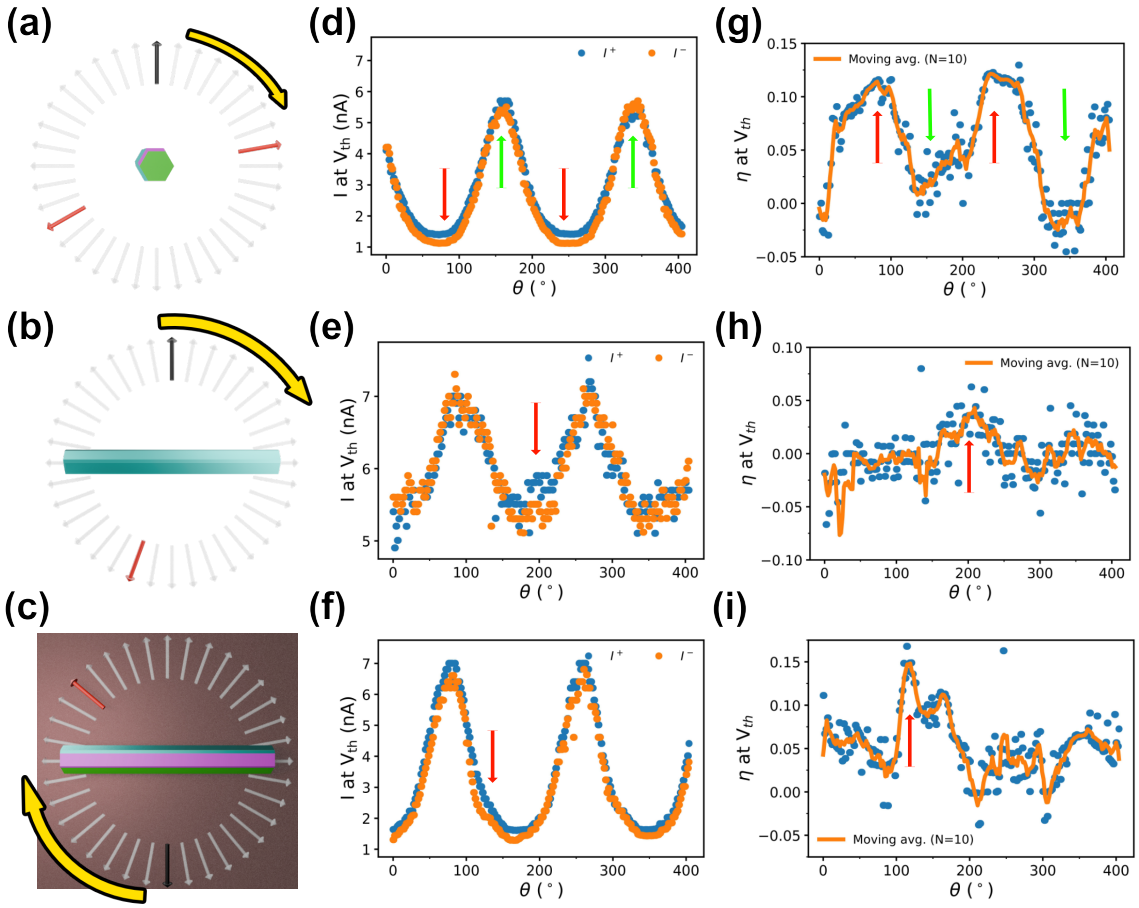

Figure 4.14: Angular dependence of Device A at a fixed $|B_{\text{ext}}| = 100$ mT. **(a-c)** Schematic of the rotational planes: (a) perpendicular to the nanowire axis (the axis is tilted approximately $-12°$ relative to the z-axis), (b) parallel to the Al facets (plane normal is perpendicular to both the nanowire and the substrate plane), and (c) the substrate plane (x–z plane, see Fig. 4.7(a)). Black arrows indicate $\theta = 0°$; yellow arrows denote the direction of rotation. **(d-f)** critical currents I^+ and I^- extracted using a 3 μV threshold. Red arrows indicate angular regions where η is maximised. In (d), green arrows highlight regions where I_c is maximised and η reaches a local minimum, coinciding with the field being parallel to the Al facets. **(g-i)** Diode efficiency $\eta(\theta)$ for the three rotation planes. The non-reciprocity directly reflects the angular modulation of I^+ and I^-. In (g), η is heavily modulated; in (h), η remains relatively static as the critical currents do not vary significantly; in (i), the substrate plane rotation exhibits a single pronounced maximum without a symmetric counterpart.

The persistence of a finite baseline contribution to η across all rotation planes indicates that the diode efficiency is not governed solely by the external magnetic field. In particular, reversing the direction of B_{ext} does not simply invert the sign of the diode efficiency. Instead, the non-reciprocal response likely reflects an interplay between the external field, the EuS-induced exchange field, and the effective spin-orbit coupling of the device. This interplay may contribute to the complex angular dependence summarised in Table 4.1.

Table 4.1: Summary of angular dependence and Josephson diode efficiency for Device A ($|B_{\text{ext}}| = 100$ mT).

Rotation Plane	Max η Angle	I_c Correlation	Key Observations
Perpendicular	$\theta \approx 80°, 240°$	minimised I_c	Maximum η observed ($\eta \approx 15\%$).
(Normal to NW-axis)	$\theta \approx 160°, 350°$	Maximised I_c	Polarity reversal observed (partial) ($I_c^+ \gtrless I_c^-$).
Parallel to Al	$\theta \approx 200°$ range	Suppressed I_c	Relatively large η at I_c local minima; significant baseline offset persists.
Substrate plane	$\theta \approx 130°$ range	Suppressed I_c	Maximum η where I_c is lowest; highly anisotropic modulation.

The absence of a robust sign reversal under magnetic-field inversion suggests that the diode response cannot be understood solely in terms of the externally applied field. This motivates a broader comparison between different devices to determine whether the observed baseline contribution is an intrinsic feature of the InAs-EuS-Al platform or instead depends on device-specific properties such as morphology and magnetic configuration.

4.2.6 Comparative Analysis of Device-Dependent JDE

To determine whether the magnetic evolution of the JDE is reproducible across the InAs-EuS-Al platform, we compare the transport response of Devices A, B, and C. As established in Figs. 4.10 and 4.11, the devices share several common features, including finite cooldown diode efficiencies in Devices A and B, pronounced magnetic hysteresis, remanent exchange fields, and qualitatively similar superconducting gap evolution under applied magnetic field. These observations demonstrate that the EuS layer is magnetically coupled to the superconducting transport in all investigated devices.

Having established these common characteristics, we now examine whether the magnetic-field dependence of the diode efficiency η evolves similarly across the different samples.

Divergent Axial Response Compared to Device A, Device B exhibits a more strongly field-dependent evolution of the diode efficiency. Axial field sweeps of Device B (Fig. 4.15) show that the diode efficiency can be tuned continuously by the applied field. For magnitudes $|B_{\text{ext}}| < 100$ mT, Device B displays a clear polarity reversal when the sign of the field is changed. In this low-field range, the diode efficiencies for forward and reverse sweeps are mirrored (Fig. 4.15(c), consistent with an approximately antisymmetric response governed by the reversal of the EuS polarisation. However, for $|B_{\text{ext}}| > 100$ mT, Device B transitions into a regime more similar to Device A, where the polarity switch is no longer observed upon field reversal.

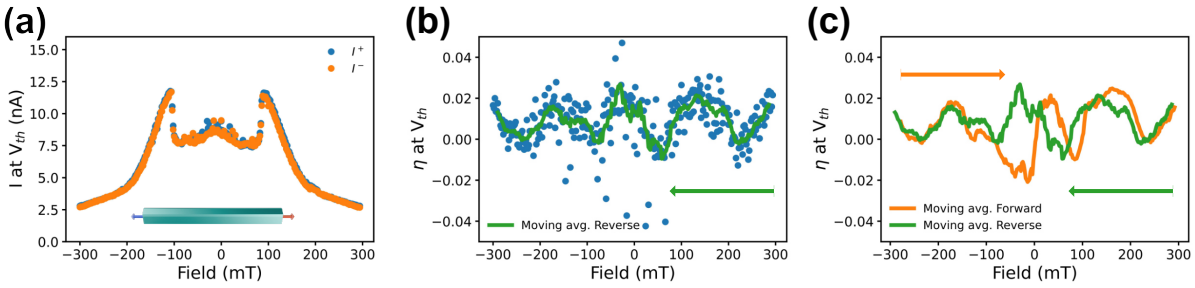

Figure 4.15: Axial field dependence of device B. **a)** Magnetic-field dependence of the positive and negative critical currents, I^+ and I^- at a $V_{th} = 10\mu V$ voltage threshold. The higher V_{th} here is necessary due to thermally rounded IVCs. Insert **a)** Illustration of the nanowire (light blue) and the magnetic-field orientations (red and blue arrows) parallel to the nanowire axis within the substrate plane, used for the transport measurements. The critical current increases around $|B_{ext}| \approx 110$ mT, corresponding to the transition of the thick electrodes to the normal state, resulting in the lowering of the effective temperature in the junction. **b)** Diode efficiency η as a function of B_{ext}. The solid green line denotes a ten-point moving average. B_{ext} was swept from positive to negative values as indicated by the green arrow. An oscillatory behaviour is observed, and the efficiency is asymmetric with respect to zero field, however not at fields $|B_{ext}| > 100$mT. **c)** Moving averages of the diode efficiency for forward (negative ferromagnetic polarisation, orange arrow) and reverse (positive ferromagnetic polarisation, green arrow) B_{ext} sweeps. For fields $|B_{ext}| < 100$mT the two sweep directions produce mirrored $\eta(B_{ext})$ reflective of the influence of the EuS polarisation.

Field Rotation Response The distinction between the devices is further supported by the angular rotations in the substrate plane shown in Fig. 4.16. Devices A and C both exhibit a substantial non-zero baseline contribution to $\eta(\theta)$, characterised by the absence of a clear antisymmetric response under a 180° field rotation. In contrast, Device B shows a more nearly antisymmetric response ($\eta(\theta) \approx -\eta(\theta+180°)$) at 100 mT for certain angular ranges. Within these regions, the diode efficiency changes sign upon a 180° rotation of the field, as indicated by the zero-crossing red arrow in Fig. 4.16(e-f), while the prominent features highlighted by the green arrows explicitly showcase this $\eta(\theta) \approx -\eta(\theta + 180°)$ antisymmetry.

This variation suggests that the balance between intrinsic and externally controlled symmetry-breaking may be sensitive to device-specific morphology. Scanning electron micrographs (Fig. 4.7) reveal that Devices A and C exhibit noticeable bending, whereas Device B is comparatively straight. Mechanical strain associated with this bending could influence both the magnetic configuration of the EuS layer and the electronic structure of the InAs core, potentially modifying the effective exchange field and SOC experienced by the junction. Changes in the SOC could additionally alter the orientation or strength of the effective spin-orbit field and thereby modify its interplay with both the external magnetic field and the EuS-induced exchange field.

Such effects could contribute to the differing balance between baseline and field-dependent diode behaviour observed across the devices. However, establishing a direct connection between morphology, magnetic configuration, and the Josephson diode response would require further systematic investigation.

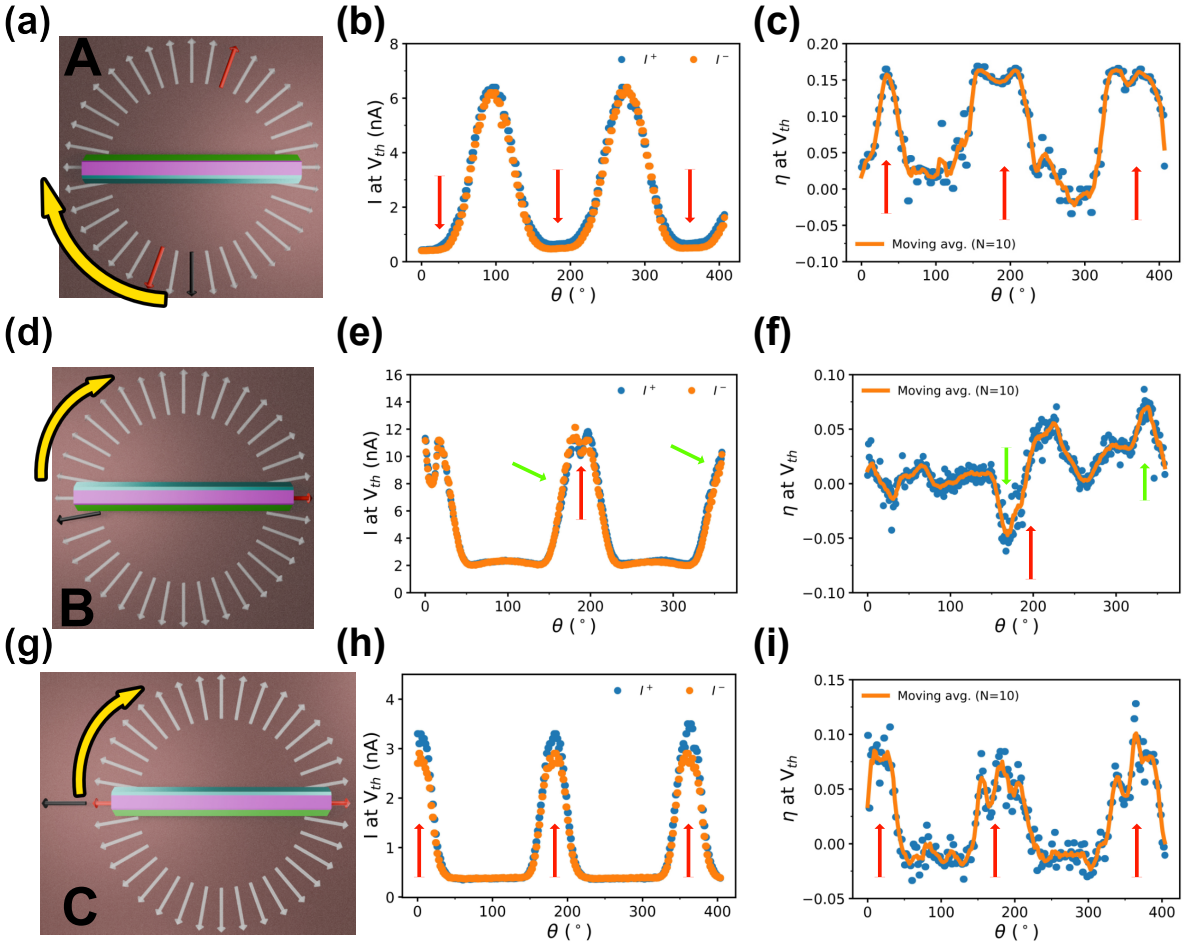

Figure 4.16: Comparative magnetotransport anisotropy and Josephson diode efficiency within the substrate plane across Devices A, B, and C, measured at fixed external magnetic fields of 180 mT (Device A), 100 mT (Device B), and 150 mT (Device C). **(a–c)** Transport signatures for Device A (top row): **(a)** Schematic layout of the rotation configuration, where the straight black arrow indicates the $\theta = 0°$ reference and the yellow arrow marks the direction of the angular sweep. **(b)** Extracted (I^+) and (I^-) critical currents as a function of rotation angle θ, with red arrows identifying the angular domains where the current split is maximised. **(c)** Resulting efficiency $\eta(\theta)$ tracking the baseline-dominated JDE. **(d–f)** Transport signatures for Device B (middle row): **(d)** Rotation geometry schematics. **(e)** Critical currents versus θ, where a red arrow highlights the polarity crossover near $\theta \approx 180°$ where η flips sign, and two green arrows indicate the highly asymmetric regions separated by a 180° interval. **(f)** Corresponding diode efficiency $\eta(\theta)$ displaying a nearly field-dominated antisymmetric inversion. **(g–i)** Transport signatures for Device C (bottom row): **(g)** Rotation geometry schematic. **(h)** Critical currents versus θ, where red arrows identify the regions of maximum current split. **(i)** Resulting efficiency $\eta(\theta)$ mirroring the structural baseline shift seen in Device A.

4.2.7 Discussion and Conclusion

In this work, we systematically investigated the magnetic-field dependence of the JDE in hybrid InAs-EuS-Al nanowire junctions. Magnetotransport measurements reveal clear signatures of a proximity-induced exchange field, including pronounced hysteresis, remanent magnetic behaviour, and finite diode efficiencies that persist even in the absence of an external magnetic field. We further observe that superconductivity remains continuous across the coercive field of the EuS layer, in contrast to several previous studies of related heterostructures [29, 61, 76].

Although all investigated devices exhibit qualitatively similar superconducting and magnetic characteristics, the magnetic evolution of the diode efficiency differs substantially between samples. Device B exhibits a nearly antisymmetric response under magnetic-field inversion ($|B_{ext}| < 100$ mT) and angular rotation, whereas Devices A and C display a pronounced baseline contribution to the diode efficiency that persists over a broad range of field orientations and magnitudes.

These observations suggest that the JDE in the present hybrid nanowires arises from a combination of externally controlled and intrinsic symmetry-breaking mechanisms. The strong angular dependence highlights the interplay between SOC, magnetic proximity, orbital effects, and the applied magnetic field, while the persistent baseline contribution indicates that the non-reciprocal response cannot be explained solely by the external field.

The observed variation between devices further suggests a sensitivity to device-specific properties. In particular, Devices A and C exhibit noticeable nanowire bending, whereas Device B remains comparatively straight. Mechanical strain associated with such morphology could influence both the magnetic configuration of the EuS layer and the electronic structure of the InAs core, thereby modifying the effective exchange field and SOC experienced by the junction, but more importantly possibly modifying the interplay between these effects.

While the microscopic origin of the device-dependent behaviour remains unresolved, the present results demonstrate that non-reciprocal superconducting transport in InAs-EuS-Al hybrid nanowires emerges from a complex interplay of multiple symmetry-breaking mechanisms.

The preceding investigation of InAs-EuS-Al nanowires focused on engineering the symmetry-breaking conditions required for the JDE and topological superconductivity. However, the realisation of robust topological phases depends not only on magnetic proximity and SOC, but also on the coherence and transport properties of the underlying electronic system.

Three-dimensional topological insulators provide an alternative route towards topological superconductivity through their intrinsically spin-momentum-locked surface states. In the following section, we therefore shift focus from magnetic symmetry breaking to the transport properties of Bi_2Se_3 nanoribbons, with the goal of identifying ballistic transport signatures associated with the topological surface states and evaluating their suitability for superconducting hybrid devices.

4.3 Quasi-Ballistic Transport in Bi_2Se_3 Nanoribbon Josephson Junctions

In this section, we investigate quantum transport in Bi_2Se_3 nanoribbons, moving from the spectroscopic characterisation of the electromagnetic environment and symmetry breaking discussed in previous sections to the study of the transport medium itself. The goal is to identify and characterise the Topological Surface States (TSS) and evaluate their potential as a platform for engineered topological superconductivity.

4.3.1 Motivation: Ballistic Surface States and Coherence

As introduced in Section 2.1, the realisation of Majorana bound states (MBS) requires a system with strong spin-orbit coupling and proximity-induced superconductivity [199, 200], as detailed in Section 2.2.1. Bi_2Se_3 is a prototypical three-dimensional topological insulator that fulfills these requirements via its helical surface states. These states are protected by time-reversal symmetry (TRS), which enforces spin-momentum locking and makes backscattering from non-magnetic impurities forbidden [201, 202].

For these materials to serve as a platform for topological superconductivity, it is important to distinguish transport signatures originating from the TSS and the bulk, and to determine over which length scales quasi-ballistic transport in the surface states can be maintained.

In our experiments, we characterise quasi-ballistic signatures using two Bi_2Se_3 nanoribbons, **NR1** and **NR2**, with dimensions summarised in Fig. 4.17. Nanoribbon **NR1** ($W = 430$ nm, $t = 16$ nm), featuring junctions **C1** ($L = 70$ nm) and **C2** ($L = 100$ nm), was primarily utilised for the FP interferometry discussed in Section 4.3.2. Conversely, **NR2** ($W = 205$ nm, $t = 32$ nm) featured a junction-length series with L ranging from 80 nm to 1080 nm (specifically 80, 170, 300, 360, 420, 540, and 1080 nm), as illustrated in Fig. 4.17(b). As shown in the false-colour SEM images and the accompanying table in Fig. 4.17, the lateral dimensions W and t govern the transverse quantisation condition for the momentum q_n around the nanoribbon perimeter $P = 2(W + t)$ (Eq. (2.56)). This confinement leads to the formation of 1D sub-bands [148, 203–205].

4.3.2 Fabry-Pérot Interference as a Coherent Diagnostic

To verify the presence of ballistic transport within the topological surface states, we utilise FP interferometry. In nanoscale devices, ballistic transport manifests as FP resonances in the electronic conductance, where phase-coherent electron waves propagate quasi-ballistically between two semitransparent interfaces without undergoing scattering [206, 207].

As established in the theoretical framework of Section 2.3.2, the nanoribbon weak link acts as an electronic cavity where the Al-TI interfaces provide the necessary reflectivity for interference. The constructive interference of electron waves reflected within this cavity results in resonant transmission whenever the condition $k_F L = \pi n$ is satisfied [206]. In Dirac materials such as Bi_2Se_3, the Klein tunnelling process [150] enables a subset of highly transmissive propagation trajectories to remain observable even in 2D geometries

[204, 205, 208, 209]. These resonances manifest as periodic oscillations in the device conductance $G(\mu)$, as described by the Landauer formula in Eq. (**??**).

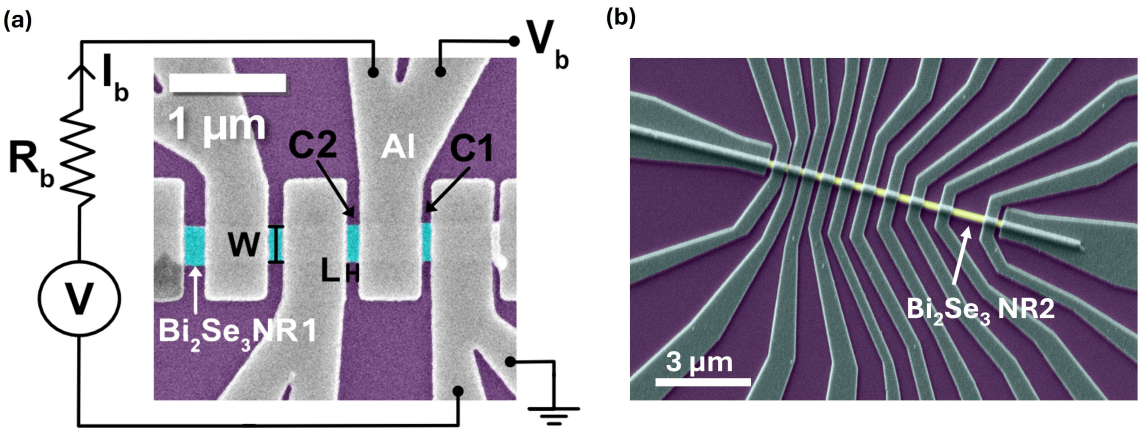

Nanoribbon	Width (nm)	Thickness (nm)	Device / Junction length (nm)
NR1	430	16	C1 (70 nm), C2 (100 nm)
NR2	205	32	C3 (80 nm, 170 nm, 300 nm, 360 nm, 420 nm, 540 nm, 1080 nm)

Figure 4.17: a) False-coloured SEM images of nanoribbon **NR1**, illustrating devices **C1** and **C2** along with the measurement layout. **b)** Junction array on a single Bi_2Se_3 nanoribbon (**NR2**), with lengths L ranging from 80 nm to 1 μm.

The resulting conductance maps for **NR1** are presented in Fig. 4.18, revealing characteristic "FP diamonds." The periodicity of these features in the zero-bias conductance matches the subband spacing expected from the nanoribbon perimeter $P = 2(W + t)$, yielding a spacing $\Delta\mu^W \approx 2.40$ meV.

To probe the normal-state transport, superconductivity in the Al electrodes was suppressed using an out-of-plane magnetic field of 30 mT. The differential conductance $G = dI/dV_b$ was obtained from the measured I-V characteristics, and a smooth background was subtracted to enhance the visibility of the phase-coherent oscillatory features.

The resulting background-corrected maps G_{bgr} are presented in Figs. 4.18(a) and (d). To further resolve the diagonal resonance lines, we computed the derivative dG_{bgr}/dV_g following the approach in Ref. [148], revealing the characteristic "FP diamond" patterns shown in Figs. 4.18(b) and (e). For 2D-FFT Analysis and width quantisation, we utilise a two-dimensional Fast Fourier Transform (2D-FFT) to determine the characteristic periodicities of these oscillations. Finding that for device C1, the 2D-FFT (Fig. 4.18(c)) highlights four distinct peaks at frequencies $f^W_{V_b} \simeq \pm 204\,\mathrm{V}^{-1}$ along the bias direction.

This is in close agreement with the expected value of $208\,\mathrm{V}^{-1}$ associated with 1D sub-band quantisation due to momentum confinement around the nanoribbon perimeter $P = 2(W+t)$. Similarly, device C2 (Fig. 4.18(f)) exhibits peaks at $\simeq \pm 216\,\mathrm{V}^{-1}$.From these measured peak positions, we extract a sub-band energy spacing: $\Delta\mu^W = \frac{e}{2f^W_{V_b}} \approx 2.40\,\mathrm{meV}$.

The reproducibility of these frequencies across different junctions on the same nanoribbon confirms that these oscillations originate from width-dependent quantisation. These results align with previous findings from our group [210], which demonstrated that gate-induced sub-band crossings manifest as pronounced conductance peaks.

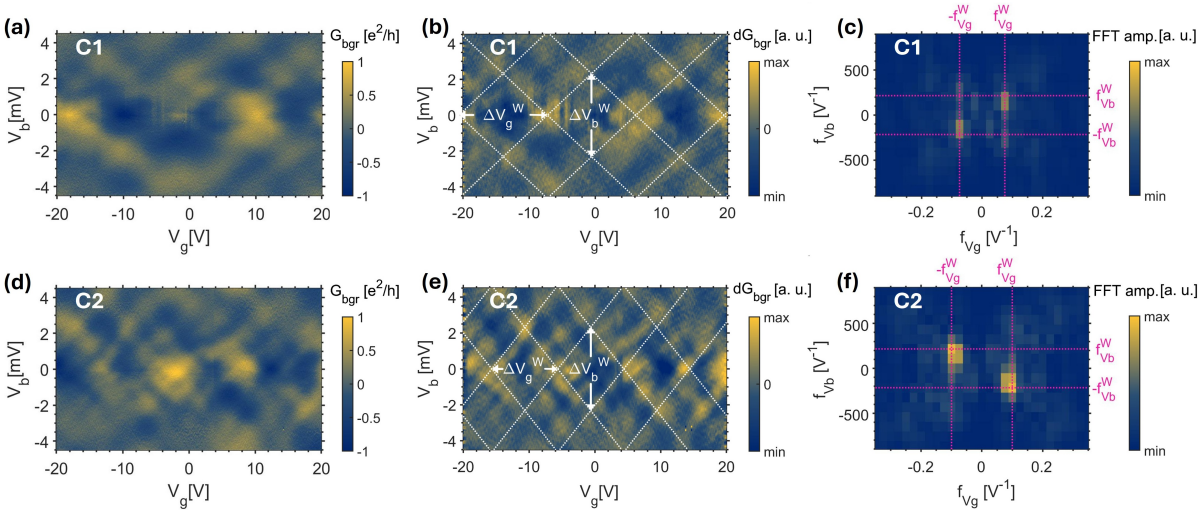

Figure 4.18: a) Background-subtracted differential conductance map of device **C1** (V_b vs V_g), showing FP resonances. **b)** Derivative dG_{bgr}/dV_g highlighting the diamond-shaped interference pattern. White dashed lines indicate expected locations of FP resonances from width quantisation. **c)** 2D-FFT of panel (b), highlighting peaks at $f_{Vb}^{W} \simeq \pm 204\ \mathrm{V}^{-1}$, consistent with transverse quantisation. **d-f)** Similar analysis for device **C2** ($L = 100$ nm), showing peaks at $\simeq \pm 216\ \mathrm{V}^{-1}$.

Note that due to experimental constraints, namely gate leakage at high $|V_g|$ and overheating at high $|V_b|$, the measurement window was insufficient to resolve the energy scale associated with length quantisation ($\Delta\mu^{L} = 14.8\,\mathrm{meV}$).

A central challenge in mesoscopic transport studies of topological insulators is distinguishing FP interference associated with coherent surface-state transport from UCF originating from diffusive modes. To address this, we compare transport measurements in both the normal and superconducting states (Fig. 4.19). Unlike UCF, which produces sample-specific fluctuations without a well-defined geometric scaling, the observed oscillations are directly linked to the cavity dimensions, consistent with quasi-ballistic transport in the helical surface states.

To address this, we compared the dG_{bgr}/dV_g maps in the normal state (30 mT) and the superconducting state (0 mT), as shown in Fig. 4.19. While the superconducting state introduces features related to the gap (Figs. 4.19(b, d)), the underlying oscillation patterns remain largely unchanged.

If the signatures were dominated by UCF, one would expect a substantial randomisation of the pattern when applying a field of 30 mT, which is approximately half the estimated correlation field $B_{cor} \sim h/eLW$. The observed stability of the pattern suggests a ballistic origin rather than a diffusive one, confirming that electron propagation remains ballistic over length scales approaching one micrometer.

While FP interferometry is consistent with coherent transport in width-quantised surface states, it remains primarily a normal-state probe and does not directly address the supercurrent-carrying properties of these channels. Furthermore, in the relatively wide nanoribbons studied here (430 nm), the observed FP features are mainly associated with transverse cavity modes. To further investigate the role of coherent surface transport in

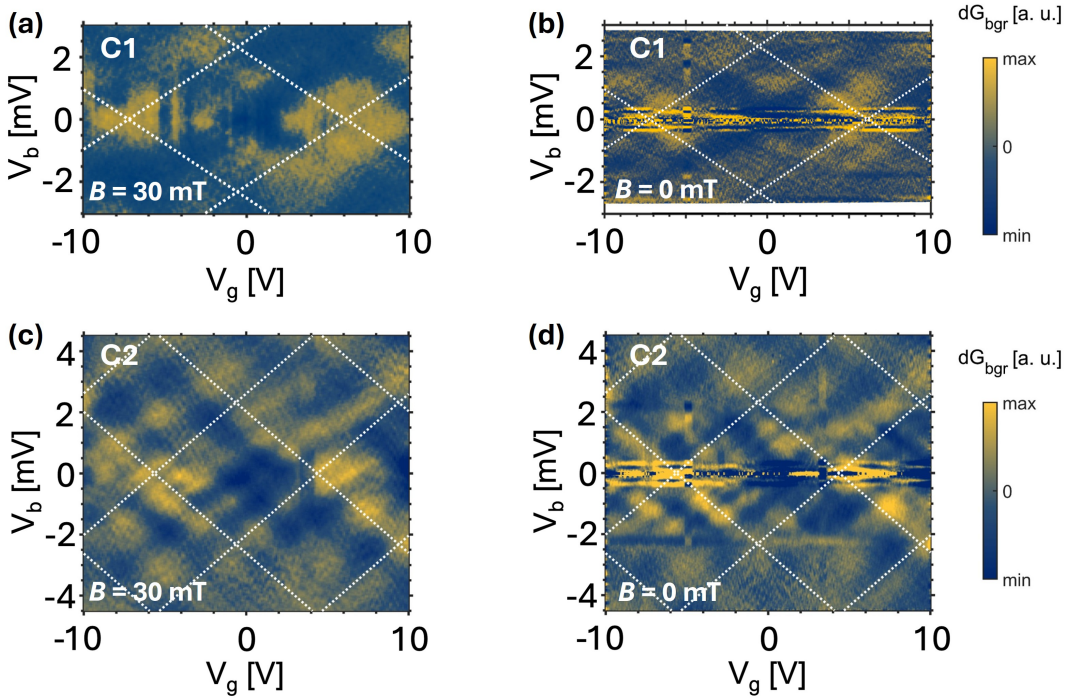

Figure 4.19: Differential conductance derivative dG_{bgr}/dV_g for **C1** in the normal state ($B_{ext} = 30$ mT, **a**) and superconducting state ($B_{ext} = 0$ mT, **b**). Panels **c** and **d** show the same comparison for device **C2**. The stability of the pattern across states suggests a ballistic origin rather than diffusive UCF.

the superconducting regime, we therefore turn to nanoribbon NR2, where a systematic variation of junction length allows the evolution from quasi-ballistic to more diffusive transport behaviour to be examined.

4.3.3 Length-Dependent Josephson Transport: Disentangling Surface and Bulk

Building on the FP evidence for quasi-ballistic transport, we turn to the Josephson effect in nanoribbon **NR2** to probe the transport properties of the surface states. In TI Josephson junctions, separate contributions from diffusive bulk and surface states have previously been identified through temperature-dependent measurements [211]. However, for the longer junctions studied here, the critical currents are relatively small (tens of nA, for most junction sizes), and thermal suppression of the switching current at elevated temperatures complicates a reliable separation of the different transport contributions. We therefore fix the temperature at a base value of 20 mK and instead investigate the transport behaviour through a systematic scaling analysis as a function of junction length L.

Transport characteristics for the **NR2** series are summarised in Fig. 4.20. Using the transport analysis methods introduced in Sec. 2.3, the low-bias measurements shown in Fig. 4.20(a,b) are used to extract the switching currents. By comparing 2- and 4-point

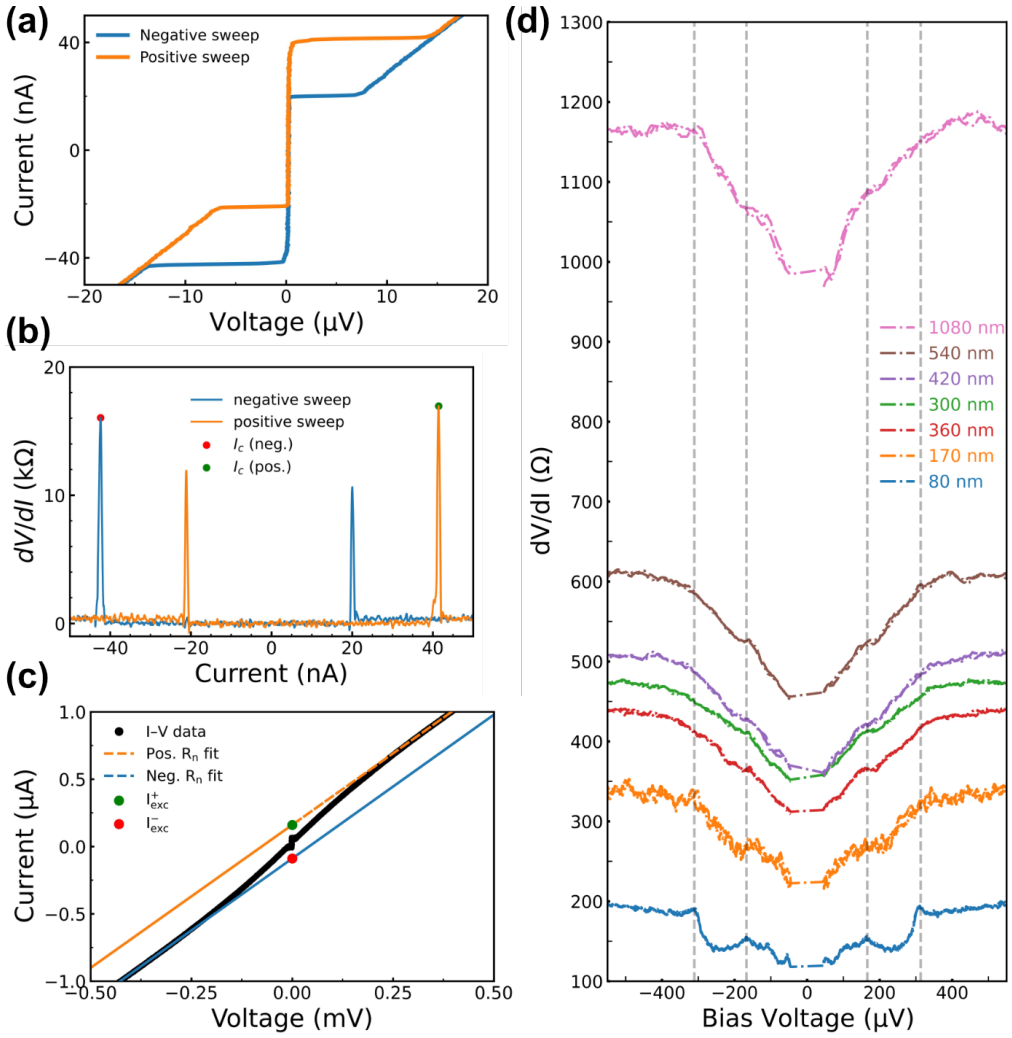

Figure 4.20: Transport characterisation of representative Josephson junctions on nanoribbon **NR2** ($T = 20$ mK). (a) Low-bias current-voltage characteristic (IVC) of a 300 nm junction, showing the switching from the superconducting to the resistive state. (b) Differential resistance dV/dI as a function of bias current, used to extract the critical current I_c. (c) High-bias IVC used to determine the normal-state resistance R_n and excess current I_{exc} via linear fits to the normal branch. (d) Differential resistance vs. bias voltage for junctions of different lengths (**NR2**). Dashed lines mark the positions of the induced gap Δ'/e and $2\Delta'/e$.

configurations, we infer a contact resistance of approximately 1 Ω, which is negligible compared to the total junction resistance. Together with the observation of pronounced MAR subgap features [85], this indicates highly transparent Al-TI interfaces.

Parallel Channel Model and Scaling Crossover

The normal-state resistance R_n is shown as a function of length in Fig. 4.21(a). The non-linear increase is well-described by a parallel combination of a diffusive bulk channel and a surface-state channel that undergoes a ballistic-to-diffusive crossover at $L \approx 500$ nm.

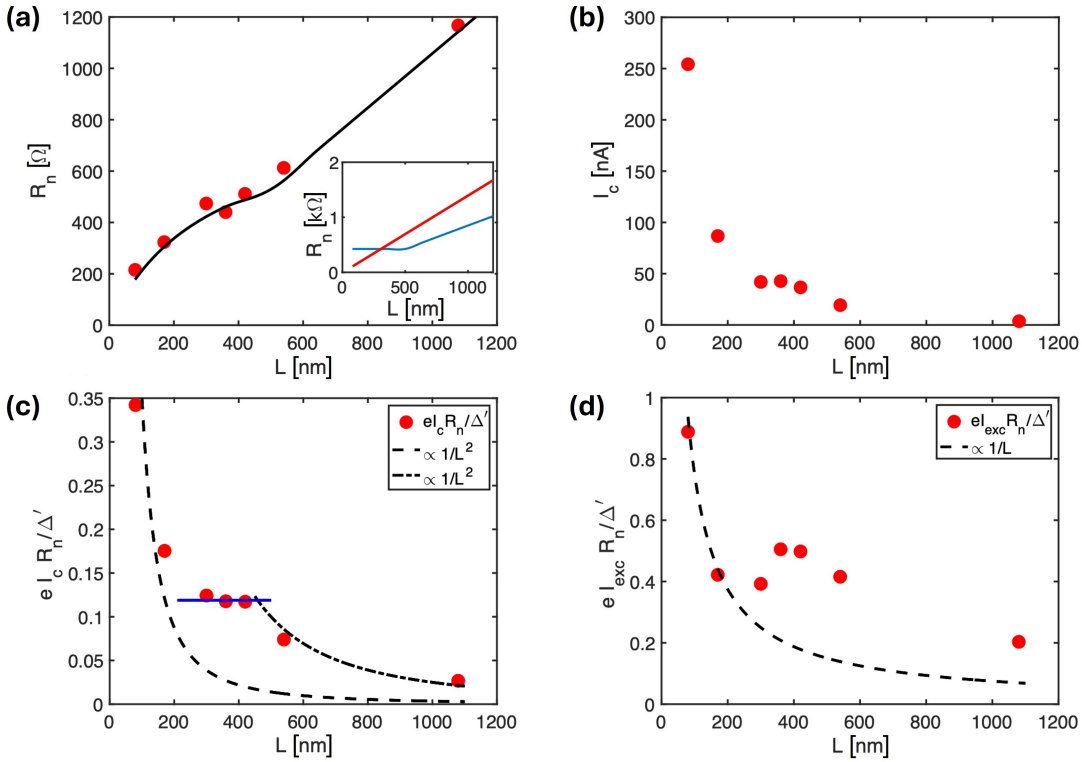

Figure 4.21: Length dependence of transport parameters for **NR2** Bi_2Se_3 nanoribbon Josephson junctions. (a) Normal-state resistance R_n as a function of junction length (red dots). The solid line shows a fit to two parallel transport channels (shown in the inset): a diffusive bulk contribution (red) and surface-state conduction (blue). (b) Critical current I_c vs. junction length. (c) I_cR_n product, normalised to Δ'/e, as a function of junction length L. The dashed and dash-dotted curves illustrate the $1/L^2$ dependence expected for long diffusive junctions. (d) Excess current, normalised to Δ'/R_ne, as a function of junction length. The dashed line illustrates the $1/L$ dependence expected for long diffusive junctions.

The I_cR_n product, normalised to Δ'/e, reveals a distinct crossover in the transport regime (Fig. 4.21(c)). For $L < 200$ nm, the product decays approximately as $1/L^2$, a hallmark of a long diffusive junction ($L > \xi_{\text{diff}}$) where the supercurrent is dominated by bulk states (Table 2.2). However, between 200 nm and 500 nm, a clear plateau emerges. In this regime, the diffusive bulk contribution becomes increasingly suppressed with junction length, while the quasi-ballistic surface states continue to support a comparatively robust supercurrent.

Excess Current and Mean Free Path Comparison

To corroborate this behaviour, we plot the excess current, normalised to Δ'/R_ne, which reflects the overall junction transparency [132]. In contrast to the $1/L$ scaling expected for long diffusive junctions [133], we observe a saturation over length scales of 300-500 nm.

Interestingly, the mean free path extracted from conventional magnetotransport measurements in our nanoribbons is only $\sim$ 150 nm for typical mobility values of $\sim$ 4000 cm^2/Vs

[80, 86]. As magnetotransport yields a value averaged over both ballistic and diffusive modes, these observations suggest that Josephson scaling and Fabry-Pérot interference measurements are considerably more sensitive probes of ballistic transport modes in topological insulators.

4.3.4 Conclusions

Our measurements demonstrate that Bi_2Se_3 nanoribbon Josephson junctions host phase-coherent surface-state transport that gives rise to both transverse Fabry-Pérot resonances and a robust Josephson supercurrent. By systematically varying the junction length, we distinguish the contribution of quasi-ballistic surface transport from the more diffusive bulk background. In particular, the observed scaling behaviour indicates that ballistic transport modes in the topological surface states persist over junction lengths approaching 500 nm. These results provide a framework for identifying coherent transport channels in topological insulator nanostructures and for evaluating their suitability as hybrid superconducting platforms.

4.4 Summary

The experimental results presented across the previous sections provide a comprehensive characterisation of hybrid Josephson junctions from two distinct perspectives. We first demonstrated that ultra-thin Al junctions remain robust in high magnetic fields, serving as sensitive on-chip detectors. We then explored the engineering of non-reciprocity in ferromagnetic hybrid nanowires and the identification of quasi-ballistic surface transport in topological insulator nanoribbons.

Collectively, these magnetotransport measurements offer a macroscopic view of the symmetry landscape and transport coherence in hybrid systems. However, DC transport is inherently limited by thermal smearing, environmental noise, and the integration of multiple conduction channels. To verify the microscopic origin of these effects such as the discrete splitting of Andreev levels or the protection of Majorana parities, one must move beyond DC signatures towards frequency-domain techniques and refined device architectures. The final chapter of this thesis outlines the Outlook, detailing how the integration of microwave spectroscopy and advanced on-chip spectrometers can bridge the gap between macroscopic transport and microscopic quantum states. It also discusses possible future improvements in transport measurements on TI nanoribbons.

5 Outlook

The results presented in this thesis demonstrate that hybrid superconducting devices provide a versatile platform for probing coherent quantum transport, symmetry-breaking mechanisms, and non-reciprocal superconductivity. Building on these findings, several natural directions for future work emerge, aimed at gaining more direct spectroscopic insight and improving control over the underlying physical mechanisms.

5.1 Microwave Spectroscopy of ABS in Hybrid Nanowires

To resolve the energy-phase relation $E(\phi)$ of sub-gap states, we propose two spectroscopic architectures that move beyond DC transport which this thesis focuses on. These methods aim to map transitions between individual Andreev levels, providing a microscopic view of the symmetry-breaking mechanisms discussed earlier chapters.

5.1.1 Resonator Based Dispersive Readout of ABS

The first architecture builds on the experimental platform established in our group [212, 213], utilising high-Q NbTiN resonators for the dispersive readout of ABS transitions.

As shown in Fig. 5.2(a-b), the hybrid nanowire junction is integrated into a NbTiN coplanar stripline (CPS) resonator. This setup involves a coupled system described by the Jaynes-Cummings Hamiltonian [117, 214], where the ABS housing junction is set in a superconducting loop for flux biasing and is galvanically connected to the resonator. A local side gate allows for precise electrostatic control of the junction's chemical potential.

Energy resolution is achieved through two-tone spectroscopy. A fixed readout tone monitors the resonator's frequency, while a secondary drive tone is swept to excite transitions between Andreev levels. The resulting resonance shift δf_r depends on the coupling strength g and the detuning between the ABS transition frequency f_A and the resonator frequency f_r. In recent work on the Al-InAs platform [213], our group demonstrated the ultra-strong coupling regime, enabling the tracking of transitions up to 20 GHz using a resonator with a fundamental frequency of 8 GHz.

This high sensitivity allows us to resolve the multi-band ABS relations connected to Eq. (2.33). As illustrated in Fig. 5.1(c), strong spin-orbit interaction and finite junction length cause the Kramers partners to shift horisontally in opposite directions. These transitions are clearly visible in the experimental data (Fig. 5.1(d)), where distinct conduction channels are resolved and fitted to extract transparency τ and spin-orbit parameters.

Extending this platform to the EuS-Al-InAs system presented in Paper II provides a promising direction for studying non-reciprocal transport [213]. By tracking transition frequencies as a function of phase ϕ, the anomalous phase shift ϕ_0 can be measured

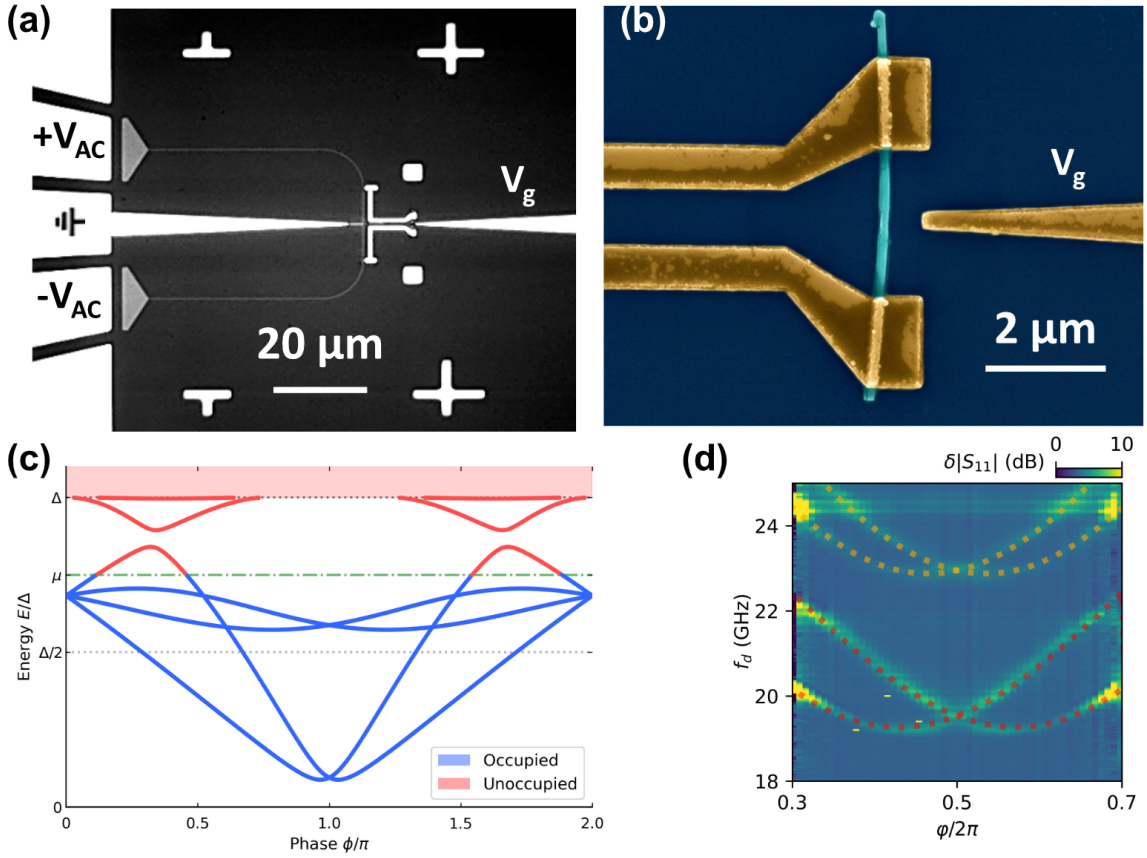

Figure 5.1: Microwave spectroscopy of a hybrid Al-InAs nanowire Josephson junction. **(a)** Optical micrograph of the NbTiN resonator structure used for spectroscopic readout, adapted from [213]. **(b)** False-colour scanning electron micrograph of the hybrid nanowire device [213]. **(c)** Simulated multi-mode Andreev bound state (ABS) spectrum for a system with strong spin-orbit coupling (SOC) and broken inversion symmetry ($\lambda_1 \neq \lambda_2$). In the absence of a magnetic exchange field, time-reversal symmetry is preserved; the broken inversion symmetry lifts the spin degeneracy, causing the Kramers partners to shift horisontally in opposite directions while maintaining global zero-phase symmetry. **(d)** Microwave spectroscopy data of the device tuned via electrostatic gating. The spectrum exhibits resonant transitions corresponding to multiple conduction channels operating in the low-transparency regime. The coloured dotted lines represent theoretical fits to two distinct channels: a slightly higher transmission mode ($\tau = 0.2615$, $\lambda_1 = 2.44$, $\lambda_2 = 3.06$, $x_r = 0.261$) corresponding to the lower frequency transitions, and a lower transmission mode ($\tau = 0.243$, $\lambda_1 = 2.8$, $\lambda_2 = 3.2$, $x_r = -0.0008$) corresponding to the higher frequency transitions. For further details, see [213].

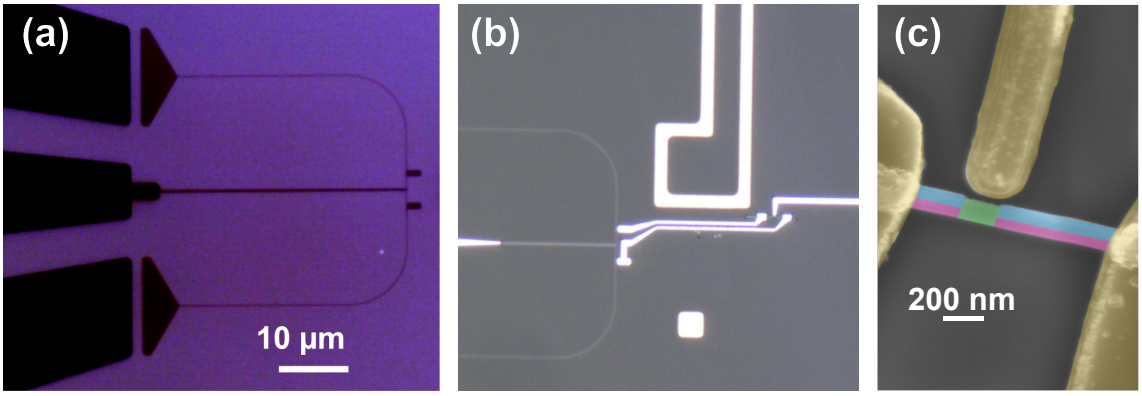

Figure 5.2: **(a)** Optical micrograph of the NbTiN resonator structure, further details can be found in [212, 213]. **(b)** Optical micrograph of the device centre, incorporating the nanowire junction detailed in (c) into the NbTiN coplanar stripline (CPS) resonator geometry. An on-chip flux loop is visible adjacent to the nanowire, enabling local magnetic flux biasing of the junction. The evaporated Ti/Al contacts are galvanically connected to NbTiN patches, which are subsequently wire-bonded to external circuitry. **(c)** False-colour scanning electron micrograph of the hybrid EuS-Al-InAs nanowire device. The Josephson junction is defined by selectively removing a segment of the epitaxial Al shell. A local side gate is positioned adjacent to the junction to provide electrostatic control. False colouring highlights the different material components: evaporated Ti/Al contacts (yellow), epitaxial Al shell (blue), epitaxial EuS layer (pink), and the exposed InAs core (green).

directly through the horisontal displacement of the spectrum. This spectroscopic approach will help clarify whether the observed Josephson diode effect in these nanowires arises from the intrinsic symmetry-breaking of the hybrid states or from extrinsic environmental asymmetries. The integration of this type of nanowire can be seen in Fig. 5.2.

5.1.2 On-Chip DC Spectrometers for Phase-Tunable Detection

A second promising future direction is the development of on-chip spectroscopic probes based on ultra-thin Al-AlO_x-Al Josephson junctions, taking inspiration from Refs. [167, 215, 216]. As demonstrated in Paper I, these junctions remain fully operational at magnetic fields exceeding 1 T and act as highly sensitive detectors of microwave excitations via inelastic Cooper-pair tunnelling allowing for spectroscopy in presence of these external fields.

By integrating our junctions into a DC SQUID geometries, we could enable phase-tunable spectroscopy of hybrid nanowire devices [138]. An implementation of such a spectrometer is shown in Fig. 5.3, with fabrication details provided in Appendix A. In this configuration, the SQUID functions as a controllable, broadband spectrometer, allowing the phase dependent parity conserving ABS transitions to be resolved.

Operating Principle The operating principle of the spectrometer relies on phase-driven microwave emission from a voltage-biased Josephson circuit [216], as illustrated

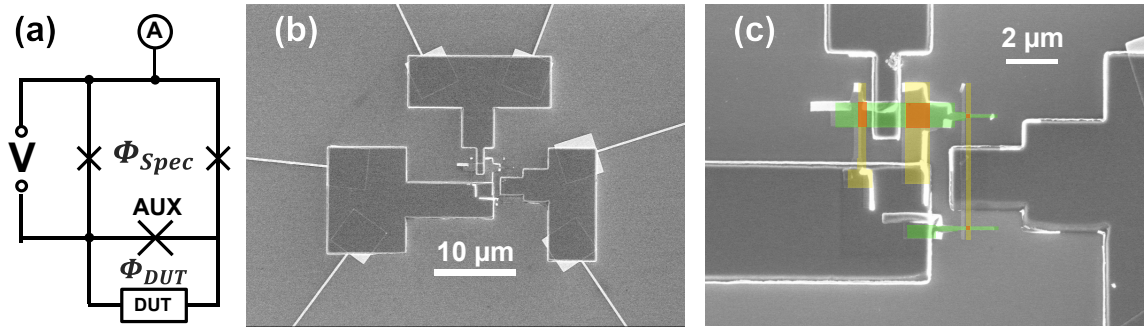

Figure 5.3: a) Schematic of the Josephson junction-based spectrometer. The device consists of two galvanically coupled SQUID loops. The upper, symmetric SQUID is voltage biased and flux biased by Φ_{spec}, enabling phase-driven microwave emission. The lower, asymmetric SQUID contains the device under test (DUT) and an auxiliary junction to allow for flux tuning. This loop is controlled via an independent flux Φ_{DUT}. Transitions in the DUT modify the current response of the coupled circuit. **b)** Scanning electron micrograph of an ultra-thin Al-AlO_x-Al junction-based spectrometer device. The circuit consists of two galvanically coupled SQUID loops. The first SQUID is symmetric and contains small-area junctions with low critical currents, while the second SQUID is highly asymmetric and designed to host a DUT. For concept verification, the DUT is here replaced by an additional Al tunnel junction with comparable critical current. The device includes PVD-deposited Ni/Pt thin-film resistors connected to bond pads, and sputtered NbTiN patches forming the interconnects between the SQUID loops and external circuitry. **c)** Zoom-in of the central region highlighting the Josephson junctions. False colouring distinguishes the two aluminium layers forming the tunnel junctions: first Al layer (green), second Al layer (yellow), and the junction areas (red) located at the overlap regions.

in Fig. 5.3(a). The spectrometer consists of a flux-biased SQUID designed to operate at $\Phi_{\mathrm{spec}} \approx \Phi_0/2$ (see Appendix B) [167, 216]. In this regime, the supercurrents flowing in the two SQUID arms largely cancel in the external circuit, strongly suppressing the net DC Josephson current while preserving circulating AC Josephson dynamics inside the loop. As a consequence, the spectrometer becomes substantially less sensitive to parasitic environmental resonances and current noise originating from the external bias circuitry.

A DC voltage bias applied across the spectrometer generates microwave radiation through the AC Josephson effect. The emitted radiation couples to a second asymmetric SQUID loop containing the DUT, allowing the spectrometer to probe the microwave absorption spectrum of the DUT. In this loop, a large auxiliary junction is placed in parallel with the DUT to form a strongly asymmetric SQUID. This asymmetry localises the superconducting phase drop primarily across the DUT, enabling phase biasing of the DUT through an externally applied magnetic flux while ensuring that the spectrometer itself acts as a weakly perturbing probe. A detailed theoretical description of the coupled SQUID dynamics and the corresponding microwave response can be found in Refs. [167, 216].

The measured DC transport response arises from inelastic Cooper-pair tunnelling processes between the spectrometer and the electromagnetic environment formed by the

DUT. Resonances in the microwave absorption spectrum of the DUT therefore appear directly as features in the spectrometer current, enabling finite-frequency spectroscopy of Andreev bound states and other subgap excitations.

Initial Device Characterisation and Future Improvements

Initial measurements of the fabricated spectrometer prototypes (Fig. 5.3(b)) revealed a magnetic-field periodicity of 135 μT in the SQUID response. This corresponds to an effective loop area of approximately $1.5 \times 10^{-11}\,\mathrm{m}^2$ ($\sim 15\ \mu\mathrm{m}^2$), which is consistent with the lithographic dimensions of the device combined with expected flux focusing effects from the wide superconducting leads.

For future implementations, optimising the geometry to reduce the effective area of both SQUID loops would be highly advantageous. A smaller loop area increases the magnetic-field scale required to inject a single flux quantum, allowing for finer resolution in phase control and improving the device's stability against ambient magnetic-field fluctuations.

5.1.3 Comparison of Techniques

The resonator architecture (Fig. 5.2) and the SQUID-based spectrometer (Fig. 5.3) provide complementary measurement capabilities and operate in distinct frequency regimes. A primary distinction lies in the measurement domain. The high-Q NbTiN resonator ($Q \approx 10^5$) enables time-resolved measurements and coherent manipulation of ABS transitions [217]. Although the sensitivity is concentrated around discrete resonator modes in the few-GHz regime, ultra-strong coupling can extend the accessible transition energies up to approximately 20 GHz [213].

In contrast, the SQUID-based spectrometer operates as a broadband frequency-domain probe with spectral coverage extending from DC to above 100 GHz [216, 218]. The spectrometer functions through inelastic Cooper-pair tunnelling, where the measured current I_{spec} probes the impedance of the external electromagnetic environment $Z_{\mathrm{ext}}(\omega_J)$ according to Eq. (2.48). By operating the spectrometer in the configuration near $\Phi_{\mathrm{spec}} = \Phi_0/2$, parasitic transport currents and environmental resonances are strongly reduced, allowing the response to be dominated by excitations of the device under test over a broad frequency range.

The two approaches are therefore highly complementary. Resonator-based techniques are well suited for coherent control, time-domain measurements, and precise extraction of microscopic parameters such as spin-orbit coupling strengths. The SQUID-based spectrometer, on the other hand, provides direct broadband access to the full energy-phase structure of the device.

Signatures of Topological Transitions and Majorana Physics The ultimate objective of this microwave-coupled architecture is to resolve the evolution of the sub-gap spectrum as the system approaches the topological regime. A hallmark of the topological phase transition (Sec. 2.2.2) is the closing and reopening of the superconducting gap, accompanied by the emergence of Majorana bound states (MBS) [27, 28, 60].

Because microwave spectroscopy probes transitions between quantum states rather than the states themselves, the measured response is governed by the selection rules and

occupation dynamics of the Andreev spectrum, which are highly sensitive to the fermion parity structure of the device under test [219, 220]. In the topological phase, a protected zero-energy crossing appears at $\phi = \pi$, where the two crossing branches possess opposite fermion parity. Direct microwave-induced transitions across this crossing are therefore forbidden by fermion parity conservation [20, 221].

Consequently, the spectroscopic signature of the topological phase is not simply a transition frequency that collapses to zero at the crossing, but rather the suppression of microwave absorption near $\phi = \pi$, reflecting the protected 4π-periodic energy-phase relation of the underlying Majorana spectrum [123, 124].

Despite these expected signatures, several experimental mechanisms can mimic aspects of topological superconductivity. In highly transparent but topologically trivial junctions, the Andreev spectrum may contain a small avoided crossing near $\phi = \pi$. When the Josephson radiation frequency,

$$\omega_J = \frac{2eV}{\hbar}, \tag{5.1}$$

becomes comparable to the avoided-crossing energy, photon-assisted Landau-Zener-type transitions can occur [222]. These processes can generate spectral responses resembling those expected from a protected Majorana crossing [223].

The interpretation is further complicated by environmental parity-breaking processes such as quasiparticle poisoning, local Joule heating, or the breaking of Cooper pairs by high-energy photons [47, 224, 225]. Such processes generate nonequilibrium quasiparticles that can randomise fermion parity on experimentally relevant timescales, partially lifting the parity protection and thereby reintroducing otherwise forbidden transitions.

As a result, while on-chip microwave spectroscopy provides a powerful probe of phase-dependent Andreev spectra, the transition to a topological Majorana spectrum may become difficult to access unambiguously in steady-state measurements. Resolving the underlying parity structure will likely require more advanced architectures capable of controlled parity manipulation or interferometric detection, enabling the distinction between genuine topological signatures and non-equilibrium parity-breaking processes. Strategies such as controlled parity switching or interferometric detection will be essential to unequivocally confirm the topological nature of the observed spectra and distinguish them from non-equilibrium parity-breaking processes [127, 130].

5.2 Advanced Control of Topological Insulator Nanoribbons

Finally, further investigation of topological insulator nanoribbon devices could focus on enhancing control over the carrier density and the coherence of transport pathways. In particular, the implementation of local electrostatic gating utilising high-κ dielectrics and refined gate architectures would allow for the precise tuning of the relative contributions of bulk and surface transport, enabling controlled access to regimes where phase-coherent ballistic transport dominates [210].

While reaching the true single-channel limit in Bi_2Se_3 remains challenging due to the high intrinsic carrier densities ($\sim 10^{13}$ cm^{-2}) and limitations imposed by dielectric breakdown, improved gating strategies could nevertheless reduce bulk contributions and en-

hance the relative contribution of coherent surface transport. Simulations further indicate that increasing the junction width W could improve the visibility of longitudinal Fabry-Pérot oscillations over a broader chemical-potential range. As the transverse confinement energy scale decreases with increasing width, the transverse mode spectrum becomes progressively denser, allowing the longitudinal interference pattern governed by

$$\Delta\mu^L \approx \frac{hv_F}{2L} \tag{5.2}$$

to remain observable at higher chemical potentials.

Achieving this level of control would likely require local interface gating through the implementation of split-gates at the S-N interfaces in order to sharpen the electrostatic potential step. Such an approach could create more specular electronic mirrors, thereby reducing the frequency "jitter" associated with imperfect reflections and enhancing the visibility of longitudinal resonances.

In this context, systematic measurements over a wider range of energies and across multiple devices would be essential to establish robust Fabry-Pérot interference. By accessing larger gate and bias windows, higher modes of the interference pattern could be resolved, providing a more stringent confirmation of its origin and allowing a quantitative comparison with theoretical models of quantisation.

Beyond electrostatic control, a primary challenge for future iterations of these hybrid junctions is the mitigation of **electronic self-heating**. The hysteresis observed in the current-biased I-V characteristics (Sec. 2.3) and the smearing of fine conductance features are characteristic of a regime where quasiparticles in the normal region cannot thermalise effectively. Future experimental designs could address these limitations through the following refinements:

Substrate and Dielectric Engineering The current devices utilise a global backgate consisting of a 285 nm SiO_2 layer on a Silicon substrate. While robust, the relatively low thermal conductivity of SiO_2 ($\sim$ 1.4 W/m·K) limits the dissipation of heat from the nanoribbon to the cryostat mixing chamber. Moving toward substrates with higher thermal conductivity, such as Aluminum Nitride or Sapphire, could significantly improve thermal coupling and enhance cooling of the hybrid interface. In addition, replacing the global backgate with local top-gates utilising high-κ dielectrics such as HfO_2 would reduce the required gate voltages and minimise heating associated with leakage currents and gate-induced electric-field stress.

Thermalisation and Quasiparticle Trapping The use of Aluminium leads is necessary to establish the S-TI-S Josephson structure. However, the superconducting gap of Al also acts as a barrier for quasiparticles, thereby trapping excess heat within the nanoribbon weak link. One possible strategy for improving thermalisation would be the incorporation of normal-metal cooling fins, such as Au or Cu, placed in direct contact with the superconducting leads. Positioned sufficiently far from the junction to avoid suppressing the proximity effect, but close enough to efficiently absorb escaping quasiparticles, such structures could provide an effective thermal sink and reduce the electronic temperature within the device.

Taken together, these directions highlight the potential of hybrid superconducting platforms for combining spectroscopy, phase control, and engineered symmetry breaking. Continued development along these lines will be important for advancing both the fundamental understanding of quantum transport in low-dimensional systems and the realisation of more complex superconducting quantum devices.